Higher Order QCD Corrections in Small x Physics

Dissertation
zur Erlangung des Doktorgrades
des Fachbereichs Physik
der Universität Hamburg

vorgelegt von
Grigorios Chachamis
aus Nafplio

Hamburg
2006

Gutachter der Dissertation:	Prof. Dr. Jochen Bartels Prof. Dr. Bernd Kniehl
Gutachter der Disputation:	Prof. Dr. Jochen Bartels Prof. Dr. Jan Louis
Datum der Disputation:	22 August 2006
Vorsitzender des Prüfungsausschusses:	Dr. Hans Dierk Rüter
Vorsitzender des Promotionsausschusses:	Prof. Dr. Günter Huber
MIN-Dekan:	Prof. Dr. Arno Frühwald

Abstract

We study higher order QCD corrections in small x Physics. The numerical implementation of the full NLO photon impact factor is the remaining necessary piece for the testing of the NLO BFKL resummation against data from physical processes, such as $\gamma^*\gamma^*$ collisions. We perform the numerical integration over phase space for the virtual corrections to the NLO photon impact factor. This, along with the previously calculated real corrections, makes feasible in the near future first estimates for the $\gamma^*\gamma^*$ total cross section, since the convolution of the full impact factor with the NLO BFKL gluon Green's function is now straightforward. The NLO corrections for the photon impact factor are sizeable and negative. In the second part of this thesis, we estimate higher order correction to the BK equation. We are mainly interested in whether partonic saturation delays or not in rapidity when going beyond the leading order. In our investigation, we use the so called 'rapidity veto' which forbids two emissions to be very close in rapidity, to "switch on" higher order corrections to the BK equation. From analytic and numerical analysis, we conclude that indeed saturation does delay in rapidity when higher order corrections are taken into account. In the last part, we investigate higher order QCD corrections as additional corrections to the Electroweak (EW) sector. The question of whether BFKL corrections are of any importance in the Regge limit for the EW sector seems natural; although they arise in higher loop level, the accumulation of logarithms in energy s at high energies, cannot be dismissed without an investigation. We focus on the process $\gamma\gamma \to Z\,Z$. We calculate the pQCD corrections in the forward region at leading logarithmic (LL) BFKL accuracy, which are of the order of few percent at the TeV energy scale.

Zusammenfassung

Wir untersuchen QCD-Korrekturen höherer Ordnung für kleine Werte der Bjorken-x-Skala. Die numerische Implementierung des vollen NLO Photon Impact Faktors stellt den nötigen, noch fehlenden Teil dar, um die NLO BFKL Resummation mit Daten aus physikalischen Prozessen, wie $\gamma^*\gamma^*$-Kollisionen, testen zu können. Wir führen die numerische Integration über den Phasenraum für die virtuellen Korrekturen zum NLO Photon Impact Faktor durch. Diese macht es zusammen mit den vor Kurzem berechneten reellen Korrekturen möglich, in näherer Zukunft erste Abschätzungen für den totalen $\gamma^*\gamma^*$-Wirkungsquerschnitt zu erhalten, da nun die Faltung des vollen Photon Impact Faktors mit der NLO BFKL Greens-Funktion direkt berechenbar ist.Die NLO Korrekturen für den Photon Impact Faktor sind betragsmäßig groß und negativ. Im zweiten Teil dieser Arbeit schätzen wir Korrekturen höherer Ordnung zur BK Gleichung ab. Unser Interesse richtet sich dabei vor Allem auf die Frage, ob die partonische Sättigung beim Übergang zu höheren Ordnungen zu größeren Rapiditäten verschoben wird oder nicht. In unserer Untersuchung benutzen wir zur Berücksichtigung von Korrekturen höherer Ordnung in der BK Gleichung das sog. 'Rapiditäts-Veto', das verbietet, dass zwei Emissionen annähernd gleiche Rapidität besitzen. Aus analytischen und numerischen Analysen schliessen wir, dass die Sättigung tatsächlich zu größeren Rapiditäten verschoben wird, sobald höhere Ordnungen berücksichtigt werden. Im letzten Teil der Arbeit untersuchen wir QCD-Korrekturen höherer Ordnung als zusätzliche Korrekturen zum elektroschwachen (EW) Sektor. Natürlich stellt sich die Frage, ob BFKL-Korrekturen im Regge-Limit für den elektroschwachen Sektor überhaupt wichtig sind. Obwohl sie erst auf einem höheren Schleifen-Niveau auftauchen, tragen sie für hohe Energien mit Logarithmen in der Energie s bei und können deshalb ohne eine genauere Untersuchung nicht ausser Acht gelassen werden. Wir konzentrieren uns hierbei auf den Prozess $\gamma\gamma \to Z\,Z$. Wir berechnen die pQCD-Korrekturen in der Vorwärtsrichtung mit einer Genauigkeit des BFKL LO-Niveaus, die einer Größenordnung von einigen Prozent bei Energien auf der TeV-Skala entspricht.

Contents

Chapter 1

Introduction

Quantum Chromodynamics (QCD) is the well established theory for the description of the hadronic interactions. If we were able to solve QCD exactly, we would then be in position to make theoretical predictions for any regime of the strong interactions. Unfortunately, in reality this is not the case. Thus, at the weak coupling limit ($\alpha_s \ll 1$), we rely on perturbation theory (pQCD) to calculate physical observables, whereas the only way so far we have to investigate the strong coupling limit ($\alpha_s \gg 1$) is on the *lattice* (lattice QCD). High energy scattering, or else the so-called *small x* limit of hadronic interactions: $\binom{s\to\infty}{x\to 0}$, can be described in terms of pQCD, given that a hard scale Q^2 is present in the process. Asymptotic freedom implies the vanishing of the strong coupling constant, α_s, in asymptotically high energies. After renormalisation, α_s is a function of that typical scale, Q^2, of the scattering. The validity of the perturbative expansion is ensured, exactly when the typical scale, Q^2, is large enough to keep α_s small, in other words when Q^2 is a *hard* scale. At the end, any computed observable is a convolution between a *hard* perturbative piece and a *soft* piece of non-perturbative origin that is determined by experimental measurements. Typically, at small scattering angles, the longitudinal components of the momenta are huge and the scale that ensures the smallness of the coupling lies in the transverse momentum space. However, in the *small x* limit of the strong interactions one cannot expect such a clean factorisation scheme between hard and soft Physics, as outlined above, since more complicated patterns appear, e.g. diffusion from hard transverse scales down to scales in the non-perturbative region. In this thesis, we will be concerned about higher order (HO) terms of the perturbative expansion.

A major step for the description of high energy scattering within perturbative QCD was the development of the Balitskii-Fadin-Kuraev-Lipatov (BFKL) equation [1]. The largest contribution to amplitudes comes from leading logarithms in s. By solving the BFKL equation, one can resum

terms

$$\alpha_s \ll 1, \quad (\alpha_s \ \ln s)^n \tag{1.1}$$

up to arbitrary powers of n, obtaining the so called 4-point gluon Green's function f_ω[1] in leading logarithmic approximation (LLA). The diagrams that contribute have a ladder-like structure with two reggeized gluons exchanged in the t-channel, whereas the rungs of the ladder depict real gluon emissions. This ladder exchange, projected in the colour singlet channel is, in perturbative QCD, the first approximation for the *Pomeron*, also called hard or BFKL Pomeron. In the old Regge theory, the Pomeron (soft Pomeron) is the leading reggeon with quantum numbers of the vacuum and of a non-perturbative nature. It has an intercept $\alpha_{I\!P}(0)$ close to unity, describing thus a weak power-like rise of the total cross sections:

$$\sigma_{tot} \propto s^{\alpha_{I\!P}(0)-1} \quad , \qquad \alpha_{I\!P}(0) = 1.08\,. \tag{1.2}$$

The BFKL Pomeron in LLA has a much larger intercept $(1+\omega_{\rm BFKL})$ suggesting a much steeper dependency of the total cross sections on the c.m. energy:

$$\sigma_{tot} \propto s^{\omega_{\rm BFKL}} \ , \omega_{\rm BFKL} = (4N_c \ln 2)/\pi)\alpha_s \ \approx 0.5, \ (\alpha_s \sim 0.2)\,. \tag{1.3}$$

The applicability of BFKL dynamics though is restricted by several factors. Thus, one could not possibly attempt to compare perturbative BFKL predictions with hadronic total cross sections that carry an important 'soft input' due to the size of the hadrons. In order to experimentally test the validity of the BFKL framework, one needs to consider scattering processes between two projectiles that have a sizeable transverse momentum of several GeV. Various observables and processes have been suggested, namely HERA forward jet production at HERA [2, 3], cross sections for Mueller-Navalet jets at LHC [4] and most importantly virtual photon scattering at an $e^\pm\ e^-$ collider (e.g. ILC) [5, 6].

$\gamma^*\gamma^*$ collisions are an excellent probe of BFKL dynamics because they do not involve any non-perturbative target. The off-shell photons fluctuate into colour dipoles that can further interact strongly. If the transverse size of the dipoles is small (high virtuality), then any soft effects are suppressed. One can tune at will the virtualities of the projectiles, Q_1^2 and Q_2^2, such that perturbation theory will be applicable. One could even try to lower the virtualities to smaller values, switching on in that way soft effects, to study the transition (or the interplay) between perturbative and non-perturbative regimes. Data from LEP [7] for virtual photon photon total cross section suggest indeed a steep rise with the scattering energy but not as steep as it is suggested in (1.3). Actually, the data are more in favour of a rise with

[1] Also notated as $\mathcal{G}$, which will be our preferred notation in Chapter 6.

a power of ~ 0.3 comparing to the $\omega_{\rm BFKL} \approx 0.5$. One is bound to wonder what the corrections beyond the LLA are, and whether they alone could lower the intercept close to the experimental value.

High energy or Regge factorisation implies that the total cross section will be a convolution between a process dependent part and a process independent part accounting for any energy dependence. The latter is the BFKL Green's function f_ω , namely the amplitude for the interaction between the two reggeized gluons exchanged in the t-channel, whereas the former consists of the so called *impact factors*: the coupling of the Green's function to the external projectiles. In our case of $\gamma^*\gamma^* \to hadrons$ scattering, we deal with the virtual photon impact factors. Higher order corrections in the process under consideration can enter in two ways, either through the impact factors or through the Green's function.

Calculating next to leading logarithmic corrections to the BFKL kernel was indeed a formidable project [8, 9]. The corrections proved to be very large and negative, lowering the BFKL Pomeron intercept even to negative values. Various studies [10] have shown that it is needed to take into account renormalisation group constraints and collinear contributions to the BFKL kernel have to be resumed consistently. In such a unified picture the behaviour of the intercept is tamed and its value is about 0.3, compatible with the data.

However, as already mentioned, these are only one part of the corrections to the $\sigma_{tot}^{\gamma^*\gamma^*}$. The NLO corrections to the Born impact factor have to be computed as well for a complete analysis if one wants really to test the NLO BFKL Pomeron against experimental data. The gluon Green's function carries a dependence on an arbitrary energy scale s_0. We can understand this as the energy that scales s in the arguments of the logarithms in order they be dimensionless. In the next Chapter we will devote some effort to sketch the derivation of the BFKL equation in order to show how this scale s_0 makes its entry. However, the total cross section should be s_0 independent, which in turn implies that there must be an s_0-dependence in the NLO impact factor such that cancels the one entering from the BFKL kernel. This indeed is the case.

Nonetheless, apart from that main motivation of testing the NLO BFKL, the project of calculating the NLO impact factor is also very important in other aspects. The cross section at the limit $Q_1^2 \ll Q_2^2$ is known from the Dokshitzer-Gribov-Lipatov-Altarelli-Parisi (DGLAP) equations [11] that resum collinear logarithms. Knowing the collinear structure of the NLO impact factor then opens a window for comparison between the collinear and the $k_\perp$-factorisation scheme. On the other hand, the NLO γ^* impact factor is important within the colour dipole picture. The colour dipole picture and the notion of the photon wave function, provide an intuitive approach to DIS-like processes. The photon wave function accounts for the proba-

bility of the splitting of the virtual photon into a quark-antiquark pair, a coloured dipole, which in turn interacts strongly with the hadron. The cross section factorises in this case into short-time effects (strong interaction between dipole-hadron) and long-time effects (lifetime of the dipole). One is justified to ask whether the dipole picture holds in higher orders, namely whether we are able to expand the virtual photon in terms of higher Fock components, like $q\bar{q}g$, $q\bar{q}gg$ etc. The colour dipole approach was very useful for the analysis of a series of HERA data in the small x region [12] and it is the favourite framework for discussing non-linear evolution equations and *parton saturation* which will concern us in the second half of this thesis.

The computation and analysis of the NLO corrections to the γ^* impact factor is also a demanding task that spans the last six years. The computation itself was divided into several steps. The calculation of the real and virtual corrections [13, 14] was carried out first. In particular, the calculation of the virtual corrections has been done in such a way, that provides us with the amplitude for γ^* g^* amplitude. Next step was the demonstration of the cancellation of the ultraviolet and infrared divergencies to ensure the finiteness of the result [14, 15]. The integration over phase space, for the case of real corrections, has been done analytically in Ref. [15, 16], and also a first numerical study of the behaviour of the real corrections was presented in Ref. [16]. To calculate photonic total cross sections, a last ingredient which is needed is the integration over phase space for the virtual corrections. In the first half of the thesis, we will present the results for exactly this integration, done numerically in this case, which along with the previously completed phase space integration for the real corrections, sets a full numerical implementation of the NLO γ^* impact factor. The numerical implementation, no matter how important it is for testing the BFKL Pomeron is not the end of the story for the photon impact factor. There are still open questions that have to do with the collinear structure of the impact factor and higher order Fock components of the photon wave function which, however, require an analytic handling of the virtual corrections. Although these will not be of concern in this thesis, they will have to be addressed in the near future.

To perform the phase space integration we need to convolute the amplitude from the one loop virtual corrections to the $\gamma^* g \to q\bar{q}$ vertex with the Born one, sum over helicities and colour indices and finally integrate over the loop momentum. For that purpose we have written a MATHEMATICA program that generates the code that serves as the integrand for the loop momentum integration. The expressions were very lengthy and some symbolic manipulation had to be done in FORTRAN environment. The numerical integration was performed using the Monte Carlo routine VEGAS. We have successfully gone through extended tests to ensure the correctness of the calculation. Some of these tests required a specific 'interplay' between

real and virtual contributions which adds to our confidence of having finally numerically implemented the full NLO γ^* impact factor for longitudinal polarised photons correctly.

Going back now, to hadronic scattering, as it was previously stressed, the applicability of BFKL dynamics is restricted. The reason is the presence of a soft scale, the size of the hadrons. The scattering energies have to be high but not very high. In asymptotia, BFKL predictions come in contradiction with s-channel unitarity. A crucial step for the unitarization of the BFKL Pomeron is considered to be the introduction of the afore-mentioned parton saturation [17].

The total cross sections cannot rise forever and ever with increasing s since the colliding hadrons have limited size. After a certain point, gluon recombination effects are to be taken into account. In other words, multi-parton contributions to the scattering from within the same hadron are becoming relevant. They draw the gluon density lower to limited values. This is the key idea behind *parton saturation*. BFKL of course still remains valid for a large window of values of c.m. energies. It is at very low x that we expect to observe saturation. Parton Saturation is described by evolution equations that are not linear any more and thus quite complicated. At LLA and in the large N_c limit, the best tool we have in terms of simplicity and calculational functionality to study 'saturated' systems is the Balitskii-Kovchegov (BK) equation [18, 19]. It is based upon the BFKL "kernel". It contains, nevertheless, a non linear term, that accounts for the gluon fusion.

So far, there is not a definite experimental verification of saturation. There are hints at HERA but not a definite answer. Data fits exist, that describe the HERA data with and without the use of saturation equally well. Needless to say, that apart from the question of the phenomenological relevance or not of saturation physics for near-future accessible rapidities, it is also very important to understand its theoretical fundamental significance in high energy scattering, since saturation is 'touching' non-perturbative effects but from 'above', that is from really high energies.

An important quantity in parton saturation physics is the *saturation scale*, $Q_s(Y)$, a momentum scale as a function of the rapidity (energy). It signifies at which scale non-linear effects (saturation effects) become important. Its functional form is derived from the BK equation. It is not only from a phenomenological point of view, but also from a more general theoretical interest, that we want to check what is the impact of higher order corrections to the saturation scale. Namely, whether they delay or bring forth in rapidity the onset of saturation. Phenomenologically it would suggest the 'correct' region of rapidities to look for saturation. On the other hand, if the significance of the HO corrections is very large, one is tempted to investigate whether an approach of taking into account increasingly higher order terms of the perturbative expansion can be an alternative to the notion of satu-

ration. This last seems not to be very likely [20]. Nevertheless, as we have mentioned already, BK and BFKL share the same kernel and since the NLO corrections to the BFKL equation are large we have to ask ourselves what is the impact of NLO corrections for the BK equation and in turn for the saturation scale. Corrections to the BK equation can also come by relaxing the assumption of large N_c-limit but these will not concern us in this thesis.

The phenomenological method we used to estimate higher order effects to the BK equation was by introducing a *rapidity veto* [21] which forbids subsequent emissions to be very close in rapidity and is known to mimic higher order corrections to the linear BFKL equation [22, 23]. Firstly, we introduce the veto constraint using analytical arguments and we estimate the functional dependence of the saturation scale Q_s on rapidity Y. Finally, we perform a full numerical analysis by solving the BK equation in FORTRAN for different values of veto and we estimate again the functional relation between Q_s and Y. The numerical and analytical approaches to the impact of HO corrections to the BK equation are consistent.

In the last part of the thesis, we deal with higher order QCD corrections seen from a completely different perspective. We are concerned with their impact as additional corrections to the Electroweak (EW) sector of the Standard Model. Accuracies of the EW experimental data are so high in many cases, that in order to compare with theoretical predictions one has to take into account next-to-next-to-leading order EW corrections. It seems natural then the question whether pQCD corrections in the small x limit, or equivalently BFKL corrections in the Regge limit are of any importance for the EW sector. Naively, one would argue that they are not since they arise at higher loop level. But in the kinematical limit that we are interested, we know that gluon emissions can generate large logarithms in energy so the answer is not straightforward. We investigate this question by considering photon photon scattering in the vector boson production channel again and in particular the process $\gamma\gamma \to ZZ$. We compute the one loop EW amplitude and the LLA BFKL corrections to it for different helicity channels. The pQCD approach is based once again upon Regge factorisation but in this case the process dependent part is the $\gamma \to Z$ impact factors also in LLA.

The outline of this thesis is as follows: We are concerned with effects in the small x kinematical region that come from higher order corrections to linear and non-linear QCD evolution equations. The magnitude of these effects is important for theoretical and phenomenological reasons. In Chapter 2 we summarise the linear evolution equations in QCD. We sketch the derivation of BFKL equation which will prove useful in the discussion of s_0 dependence. We give an account of NLO BFKL and we introduce the method of the rapidity veto constraint. In Chapter 3 we present our results for the phase space integration of the virtual corrections and consequently

the numerical result for the full NLO impact factor. We also discuss the computation of the $\sigma_{tot}^{\gamma^*\gamma^*}$. In the next Chapter we argue on parton saturation and we describe the BK equation. It is in Chapter 5 that we estimate the importance of HO corrections in the saturation regime. In Chapter 6 we present our results for the process $\gamma^*\gamma^* \to ZZ$. Finally, we will give a brief summary and an outlook for future work.

Chapter 2

Linear Evolution in QCD

In this Chapter we will discuss linear evolution equations in QCD, DGLAP and BFKL. Apart from needing both to cover most of the domain of pQCD, with DGLAP leading the evolution in $\ln Q^2$ and BFKL in $\ln(1/x)$, this introductory Chapter will serve multiple purposes. It starts with an introduction to the parton model, discussed within Deep Inelastic Scattering (DIS)-like processes. This will be helpful as a basic background concept, in which collinear and small x logarithms emerge in an clear way and secondly, it is needed in the discussion of the colour dipole picture in Chapter 5. It is also the most natural way to initiate a discussion on parton densities and in particular gluon densities. The discussion on DGLAP remains as brief as possible and it is included not only for having a more complete view on linear evolution schemes in comparison to non-linear evolution, which we will discuss later, but also because it is relevant to the collinear resummation approach of the next to leading logarithmic corrections for the BFKL equation. We extend the analysis on BFKL more as we want to point out key notions that appear later on in the NLO computation of the impact factor.

2.1 DIS kinematics and the naive Parton model

Deep inelastic scattering (DIS) is the scattering of a lepton off a hadron (typically a proton[1]):

$$L(l) + P(p) \to L'(l') + X(p_x)\,. \tag{2.1}$$

We will assume that DIS is dominated by one photon exchange (neutral current channel) $\gamma^\star(q)$, Fig. 2.1. The total cross section for virtual photoabsortion is proportional to the quantity F_2 which will be in the centre of

[1]Later on in this thesis we will even consider scattering off a nucleus

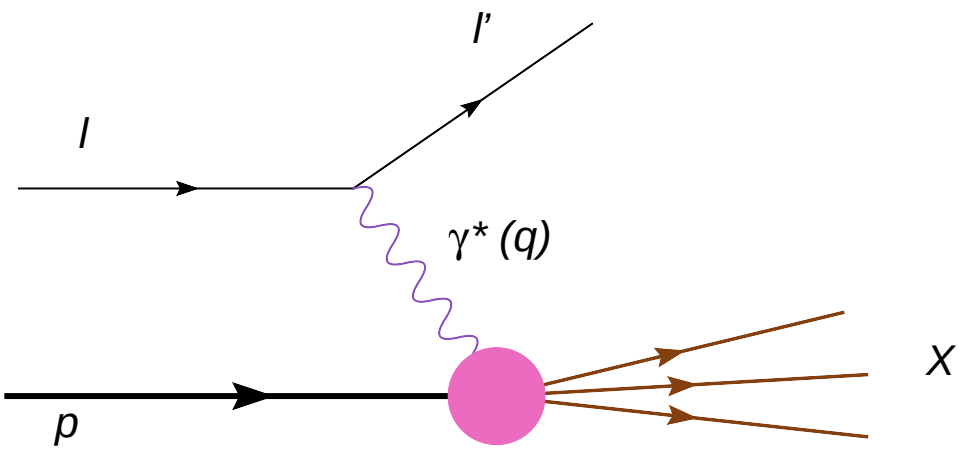

Figure 2.1: Deep inelastic scattering

our attention in the remaining of this Section:

$$\sigma^{\gamma^* N}(x,\, Q^2) \;=\; \frac{4\pi^2 \alpha_{em}}{Q^2}\, F_2(x\, Q^2)\,. \tag{2.2}$$

Let us first introduce the kinematical variables that are involved in the inclusive reaction Eq. 2.1 (it can be described by three kinematic variables). The c.m. energy squared is

$$s = (l+p)^2\,, \tag{2.3}$$

whereas the photon virtuality is (negative)

$$q^2 = -Q^2 = (l-l')^2\,. \tag{2.4}$$

The c.m. energy for the photon-nucleon system is

$$W^2 = (p+q)^2\,, \tag{2.5}$$

and the Bjorken scaling variable x is

$$x = \frac{Q^2}{2p\cdot q} = \frac{Q^2}{Q^2 + W^2 - M_p^2}\,. \tag{2.6}$$

Let us also define

$$y = \frac{p\cdot q}{p\cdot l} = \frac{W^2 + Q^2 - M_p^2}{s - M_p^2}\,. \tag{2.7}$$

If the transferred energy (difference between final E' and initial E lepton energies) is denoted by ν, in the proton rest frame, then it is $y = \nu/E$. For

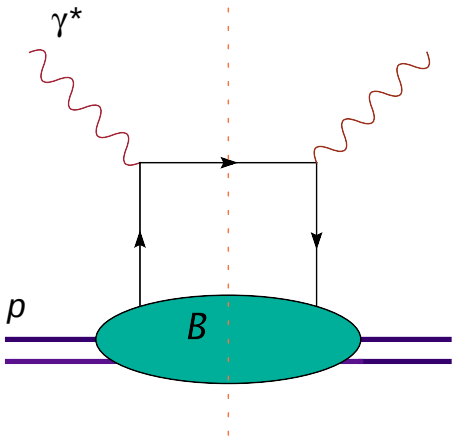

Figure 2.2: Handbag diagram.

both x and y (also called "inelasticity") it is $0 < (x, y) < 1$ and they are related by:

$$xy = \frac{Q^2}{s - M_p^2} \simeq \frac{Q^2}{s} \,. \tag{2.8}$$

We call *deep inelastic* the kinematical region where we can neglect the mass of the proton M_p with respect to the hard scales involved. Another quantity that we need to define and which will prove of great use in the second half of this thesis is the *rapidity* Y of a particle.

$$\mathrm{Y} = \frac{1}{2} \ln \frac{E + p_z}{E - p_z} \,, \tag{2.9}$$

where E is the energy of the particle and p_z is the momentum component along the z-axis. Rapidity transforms additively under Lorentz boosts along the z direction. For very fast particles one can assume that

$$\mathrm{Y} \simeq \ln \frac{2p_z}{m} \,, \tag{2.10}$$

where m is the mass of the particle. To complete the introduction of our notation conventions, let us define the "hat"$\hat{}$convention which will refer to partonic quantities e.g. $\hat{s}$ will be the c.m. energy squared for the process γq where q denotes a parton quark.

In the naive parton model, one assumes that the virtual photon scatters off an internal constituent of the proton incoherently. These constituents are treated as "free" particles. The total cross section for lepton-proton scattering can be written as a contraction of a lepton tensor and a hadronic tensor, and in terms of diagrammatic language the scattering is depicted by

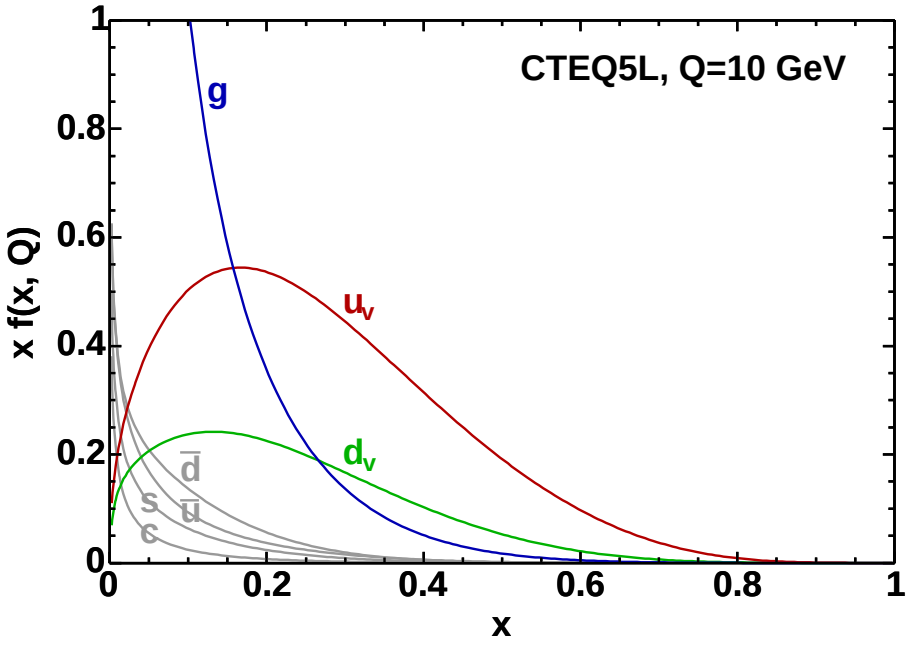

Figure 2.3: Proton's parton distribution functions.

the "handbag" diagram as in Fig. 2.2. The latter is the relevant QCD dependent object that we are interested in. It can be parametrised in terms of two dimensionless *structure functions* $F_1(x, Q^2)$ and $F_2(x, Q^2)$. Soft physics input enters into F_1, F_2 through the parton distribution functions (*pdf*'s) $f_i(x)$, with i standing for quarks anti-quarks or gluons. The distribution functions give the profile of the probability to find a parton in the proton with a fraction of momentum x, as in Fig. 2.3. In the so called Bjorken limit ($\nu, Q^2 \to \infty$), x fixed, the structure functions scale and they become functions of x only, as one can observe at Fig 2.4. They are proportional to each other and their exact relation is given by the Callan-Gross formula: $F_2 = 2xF_1$, whereas the relation between them[2] and the pdf's ($f_q(x)$, $f_{\bar{q}}(x)$) is given by:

$$F_2(x) = \sum_q e_q^2 x(f_q(x) + f_{\bar{q}}(x)) \,, \tag{2.11}$$

where the sum implies summation over flavours of quarks and anti-quarks.

2.2 DGLAP evolution equations

The naive parton model serves well for a very first description of reality but if one has a closer look things are more complicated. Starting from Fig. 2.4

[2]From now on, we will concentrate on $F_2(x)$.

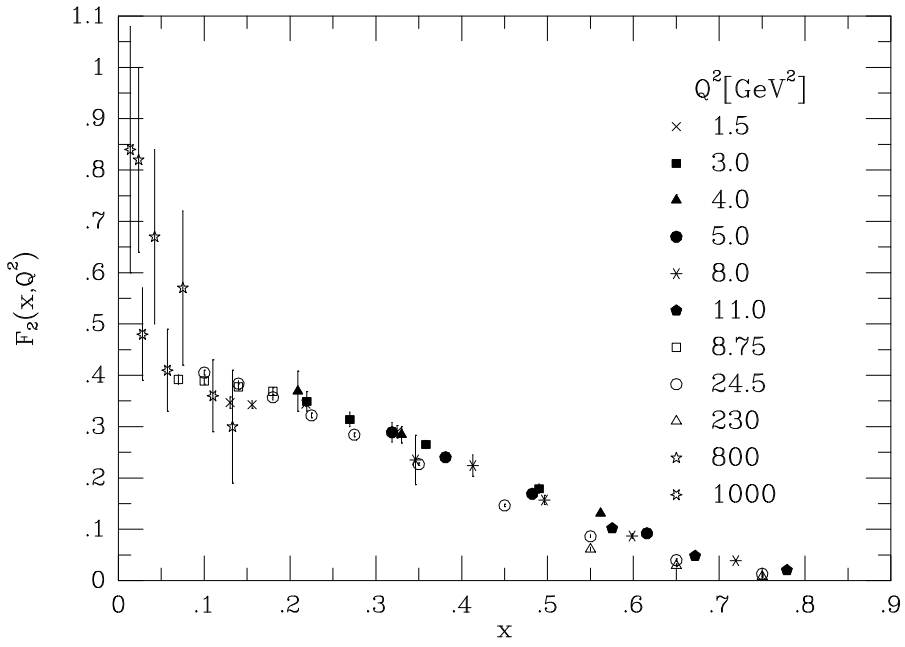

Figure 2.4: Bjorken Scaling

one can see that the scaling is not perfect for small x values and what is just an indication there, becomes an overwhelming experimental reality in Fig. 2.5. F_2 is Q^2-dependent and higher order QCD corrections are the cause. Let us consider the partonic process $\gamma^* q$ in Fig. 2.6, where a quark q is stricken by the photon. If we suppose that the probability for the quark to carry momentum fraction between ξ and $\xi + d\xi$ with $0 < \xi < 1$, is $q(\xi)d\xi$ then the cross section for the above process is

$$\hat{F_2^q}(\frac{x}{\xi}) = e_q^2 \delta(\frac{x}{\xi} - 1)\,. \tag{2.12}$$

One can go from the partonic level to the hadronic one, by 'loading' all the soft physics dependence on the pdf's and contracting them to the calculable $\hat{F_2^q}(\frac{x}{\xi})$:

$$F_2(x) = \sum_{q,\bar{q}} \int_x^1 d\xi f_q(\xi) \hat{F_2^q}(\frac{x}{\xi})\,. \tag{2.13}$$

What we see in Fig. 2.6 is the first order diagram in perturbative expansion. One must take diagrams of corrections into account as in Fig. 2.7 or alternatively in the "handbag" diagram setup as in Fig. 2.8. In order $\mathcal{O}(\alpha_s)$

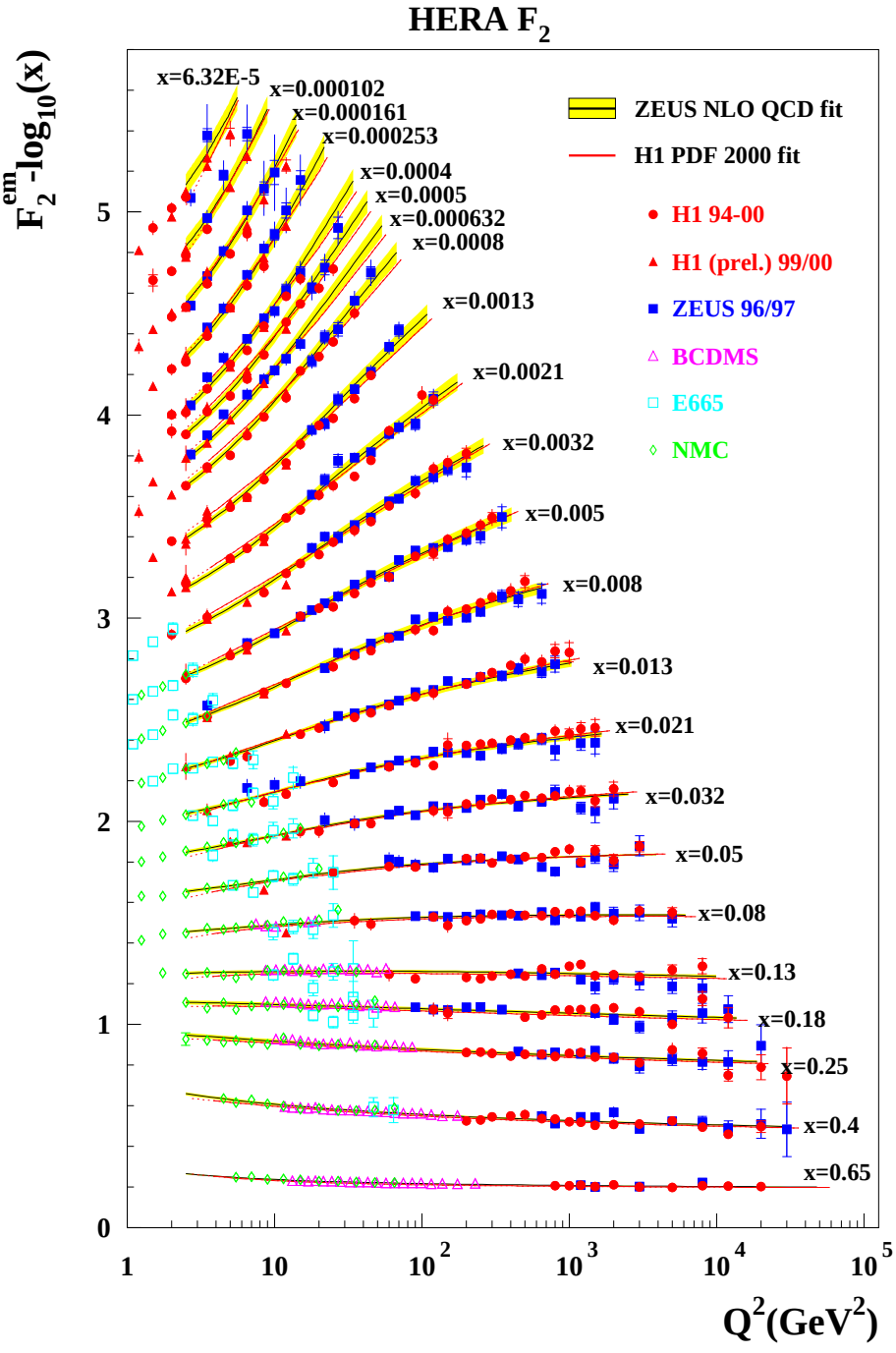

Figure 2.5: Scaling Violation.

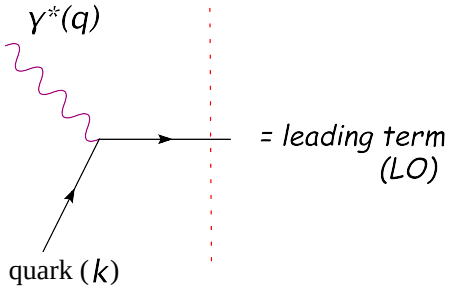

Figure 2.6: $\gamma^* q$ scattering.

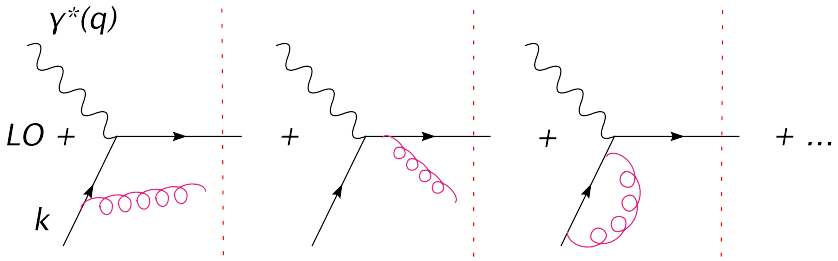

Figure 2.7: HO corrections to the upper left part of the handbag diagram.

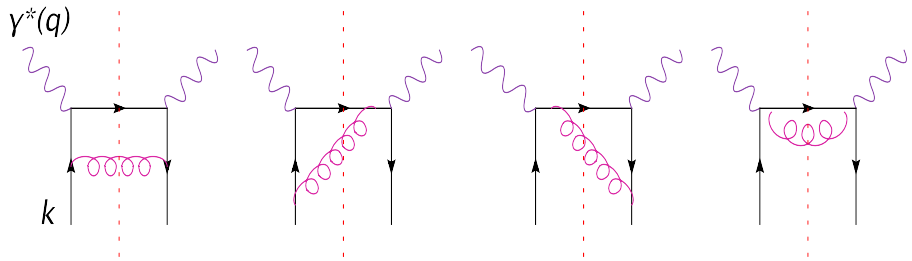

Figure 2.8: Real gluon emission diagrams bringing in logarithmic in Q^2 dependence.

the corrections modify Eq. 2.12 by a term

$$\hat{F_2^q}(\frac{x}{\xi},Q^2) = \frac{\alpha_s}{2\pi}e_q^2(\frac{x}{\xi})\left(P(\frac{x}{\xi})\ln\frac{Q^2}{Q_0^2} + C(\frac{x}{\xi})\right), \tag{2.14}$$

where Q_0^2 is a lower momentum cutoff and $C(\frac{x}{\xi})$ a calculable function. Some remarks are in order. Firstly, the $\hat{F_2^q}(\frac{x}{\xi})$ and through it F_2 acquires a Q^2 logarithmic dependence. Secondly, the divergent logarithm $\ln\frac{Q^2}{Q_0^2}$ when $Q_0^2 \to 0$ is the result of the collinear singularity that arises when the gluon is emitted parallely to the quark. We have chosen here to regularise the divergency with the use of a cutoff but a more elegant way is through dimensional regularisation. On a descriptive level, we can say that the idea is to introduce bare pdf's in which we absorb the singularities (pretty much as with the coupling constant) paying the price of introducing a renormalisation scale μ dependence. Since F_2 is a physical observable, it cannot be dependent on μ. The renormalisation group equation then demands for the quark distributions:

$$\frac{\partial q(x,\mu^2)}{\partial\ln\mu^2} = \frac{\alpha_s(\mu^2)}{2\pi}\int_x^1\frac{d\xi}{\xi}P(\frac{x}{\xi})q(\xi,\mu^2)\,. \tag{2.15}$$

This is the DGLAP equation, an evolution equation in scale. $P(\frac{x}{\xi})$ is the so called splitting function, the evolution kernel for Eq. 2.15, and it can be expanded as a power series in α_s:

$$P(\frac{x}{\xi},\alpha_s) = P^{(0)}(\frac{x}{\xi}) + \frac{\alpha_s}{2\pi}P^{(1)}(\frac{x}{\xi}) + \cdots\,. \tag{2.16}$$

At leading order, DGLAP evolution equation resums contributions of the type $(\alpha_s\ln Q^2)^n)$. The physical interpretation of the splitting function at leading order, $P_{ab}^{(0)}(\frac{x}{\xi})$, is that it gives the probability of finding a parton a with longitudinal momentum fraction x inside a parton b with momentum fraction ξ. We can have four splitting functions depending on a and b as we can see in Fig. 2.9. For the complete DGLAP equations, apart from the quark density $q(x,\mu^2)$, one has to include the coupled gluon density $g(x,\mu^2)$. After setting $t = \ln\frac{Q^2}{\mu^2}$ for convenience, we define the non-singlet distribution (q_{NS})

$$q_{NS} = q(x,t) - \bar{q}(x,t)\,, \tag{2.17}$$

for which DGLAP equation takes the form:

$$\frac{\partial q_{NS}(x,t)}{\partial t} = \frac{\alpha_s(t)}{2\pi}\int_x^1\frac{d\xi}{\xi}P_{qq}(\frac{x}{\xi})q(\xi,t)\,, \tag{2.18}$$

and the singlet one

$$\Sigma(x,t) = \sum_{flavors}\left[q(x,t) - \bar{q}(x,t)\right]. \tag{2.19}$$

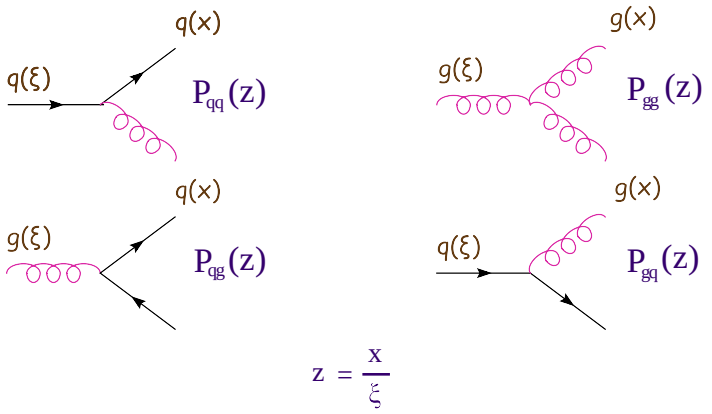

Figure 2.9: leading order splitting functions.

which evolves as:

$$\frac{\partial}{\partial t}\begin{pmatrix}\Sigma(x,t)\\ g(x,t)\end{pmatrix} = \frac{\alpha_s(t)}{2\pi}\int_x^1 \frac{d\xi}{\xi}\begin{pmatrix}P_{qq}(\frac{x}{\xi}) & 2N_f P_{qg}(\frac{x}{\xi})\\ P_{gq}(\frac{x}{\xi}) & P_{gg}(\frac{x}{\xi})\end{pmatrix}\begin{pmatrix}\Sigma(x,t)\\ g(x,t)\end{pmatrix}. \tag{2.20}$$

To conclude with this Section, in the collinear scheme, one starts from an initial transverse hard scale Q^2 and eventually, due to the emission of gluons evolves down to very small momenta. DGLAP therefore, as already pointed out is an evolution equation in scale (actually a 'revolution' since we evolve from large to small scales). As far as it concerns the parton densities, by using DGLAP one can eventually have the *pdf*'s for any virtuality of the photon Q^2, assuming of course available an initial condition for the *pdf*'s at a given initial scale Q^2_{init}, from which on the evolution will start. The way to get the initial condition at an initial scale, Q^2_{init}, is by modelling the distributions at that scale, since one cannot use pQCD to compute them. Then by evolving them to different virtualities, the crucial test for whether they are succeful or not, is how good a fit they give to the experimental data. Since the form of the parton distributions in the initial scale can only be guessed, modelled, or be obtained from experimental data, in other words, it does not enter through a perturbative calculation, what we can test indeed is the evolution of the Q^2-dependence, which in turn of course is a test for the pQCD evolutions equations. Going back to Fig. 2.5, one can see that the fit to the data is almost perfect by using NLO DGLAP evolution.

Being able to produce *pdf*'s as accurately as possible which fit the existing data and will fit data that will be obtained in the future is the main purpose of what we call global analyses of DIS and related data. There are quite a few parameterisations for the proton structure, e.g. MRST, CTEQ, GRV, that differ in the parametrisation of the initial input to the evolution, the selection

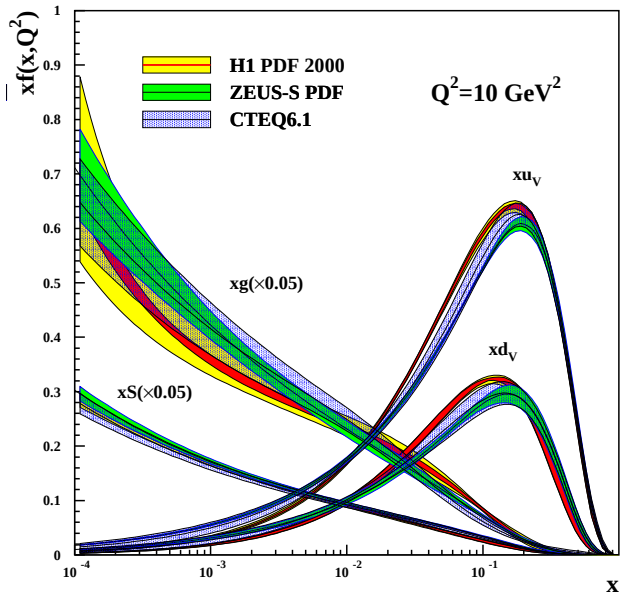

Figure 2.10: pdf's from H1, ZEUS and CTEQ parametrisation.

of the data analysed, the treatment of the experimental errors, the way of treating the value of α_s etc. In Fig. 2.10 we see the parton distribution functions from HERA along with curves from CTEQ parametrisation.

2.3 BFKL dynamics

We saw in the previous Section that by using the DGLAP evolution equation one resums logarithms of the type $(\alpha_s \ln Q^2)^n$ (collinear resummation). In this Section we will discuss the other very important evolution equation in pQCD, namely the BFKL equation, which resums logarithms of energy, that is terms like $(\alpha_s \ln s)^n$. The applicability of BFKL is guaranteed by the presence of two sizable hard scales, one at the upper and one at the lower part of the gluonic ladder, which are of the same order. That is the reason why we will base our analysis on the derivation of BFKL equation considering quark-quark scattering. Let us now proceed by demonstrating the derivation of the BFKL equation in leading logarithmic approximation (LLA) in a very simplified way [24, 25]. We will focus on the emerging of terms $\ln(\frac{s}{t})$ in the colour octet channel and of terms like $\ln(\frac{s}{s_0})$ when considering real gluon emissions. This will make more transparent later the study of real and virtual corrections of the NLO photon impact factor.

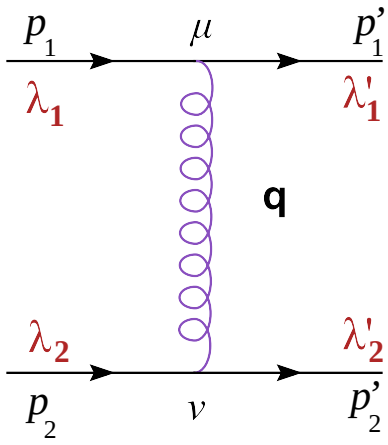

Figure 2.11: qq scattering

BFKL equation

We shall start by considering $q\,q$ scattering, whereas the physical content that the equation acquires when seen in different physical processes will be discussed later. Therefore, we will reserve our interest for the time being, on how the famous logarithms in s make their appearance, seeing it from an intuitive point of view. Throughout this Section (and actually the next Chapter) we will use the Feynman gauge. Hereafter, we will omit the "hat" notation, as it will be clear that we discuss issues on the partonic level and the extra notation would merely be an unnecessary complication. Our main three aims will be:

- Demonstrating the reggeization of the gluon.
- Defining the real emission BFKL kernel.
- Presenting the perturbative Pomeron and BFKL equation.

Some remarks are in order. The Pomeron, as we will see, can be attributed to a gluonic ladder exchanged between the two quarks in the colour singlet channel. The ladder consists of two reggeized gluons exchanged in the t channel which interact with each other through real gluon emissions. Let us consider the process in Fig. 2.11. We can write the momentum of the gluon in Sudakov parametrisation:

$$q = \alpha\, p_1 + \beta\, p_2 + q_\perp\,, \tag{2.21}$$

where $q_\perp$ denotes the transverse components of the gluon momentum. Then for our kinematics, we define $s = 2p_1p_2$ and $t = q^2 = \alpha\beta s - \mathbf{q}^2$. From now on, we will denote the transverse two-dimensional vectors by boldface

characters. A reggeized gluon has a modified propagator by a factor $s^{\epsilon(q^2)}$, namely:

$$D_{\mu\nu}(s,q^2) = -i\frac{g_{\mu\nu}}{q^2}\left(\frac{s}{\mathbf{k}^2}\right)^{\epsilon(q^2)}\,, \tag{2.22}$$

with $\mathbf{k^2} \ll s$ a typical momentum scale and $1+\epsilon(q^2)$ the gluon trajectory. The form of $\epsilon(q^2)$ is defined later in Eq. 2.38. For the t-channel gluons we decompose the metric tensor into:

$$g_{\mu\nu} \;=\; \frac{2}{s}(p_{1\mu}p_{2\nu} + p_{1\nu}p_{2\mu}) + g_{\mu\nu\,\perp}\,. \tag{2.23}$$

In our calculation here and in the next Chapter, we retain only the first term. The rungs of the ladder are compromising non-local triple gluon vertices, the so-called Lipatov effective vertices and are associated with the real emission BFKL kernel. We remind at this point that we are in the kinematical region:

$$s \gg |t|,\; u \simeq -s\,. \tag{2.24}$$

Our aim in the formulae to follow is to show how the important phenomenon of the reggeization emerges and how one can obtain the tree level amplitude for the $q\,q \;\to q\,q\,+(ng)$ process by iterating an essential "building block", namely the BFKL real Kernel. Important elements for this demonstration are the optical theorem and the use of *eikonal vertices*. Let us focus on the process in Fig. 2.11 Then for the upper vertex we have:

$$-ig_s\bar{u}(p_1+q)\gamma_\mu u(p_1)\,. \tag{2.25}$$

Because of Eq. 2.24, $q \ll p_1$ and the above formula can be approximated as

$$-ig_s\bar{u}(p_1)\gamma_\mu u(p_1) = -2ig_s p_1^\mu\,. \tag{2.26}$$

Following the same reasoning for the lower vertex, the amplitude for the process at hand will be

$$A^{(0)}(s,t) = 8\pi a_s t^\alpha_{ij} t^\alpha_{kl}\frac{s}{q^2} = 8\pi a_s t^\alpha_{ij} t^\alpha_{kl}\frac{s}{t}\,. \tag{2.27}$$

Suppose now that we are interested in the second order in perturbation theory for the qq scattering. As we want to retain only leading in s logarithms, diagrams with self-energy and vertex corrections will be neglected since they are sub-leading in $\ln s$. The diagrams that give the relevant term are shown in Fig. 2.12. Let us focus on the Fig. 2.12(a) diagram. We can calculate the imaginary part of it by means of the so called *Cutkosky rules* and then obtain the full amplitude by dispersion relations. Denoting the amplitude by $A^{(1)}(s,t)$ we will have:

$$ImA^{(1)}(s,t) = \frac{1}{2}\int d\Pi_2 A^{(0)}(s,k^2)A^{(0)\dagger}(s,(k-q)^2)\,, \tag{2.28}$$

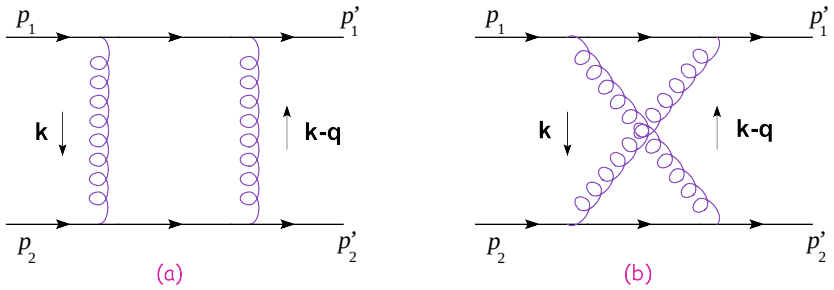

Figure 2.12: qq scattering, one loop corrections.

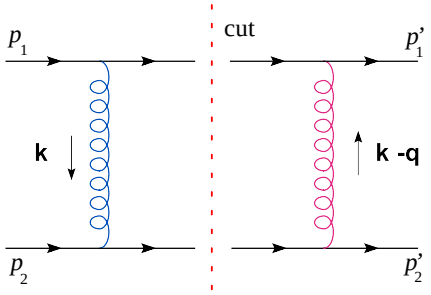

Figure 2.13: qq scattering, one loop cut amplitude.

where $A^{(0)}(s,k^2)$ and $A^{(0)\dagger}(s,(k-q)^2)$ are the tree amplitudes in Fig. 2.13 with the quark lines to be on shell at the cut points and $A^{(0)\dagger}$ denoting the hermitian conjugate of $A^{(0)}$. The two-body phase space $\int d\Pi$ is

$$\int d\Pi = \int \frac{d^4k}{(2\pi)^2}\delta((p_1-k)^2)\delta((p_2+k)^2)\,. \tag{2.29}$$

By introducing again Sudakov variables α,β and using bold face characters for transverse two-dimensional vector components, we can write for k

$$k = \alpha\, p_1 + \beta\, p_2 + k_\perp \tag{2.30}$$

and then

$$d^4k = \frac{s}{2} d\alpha d\beta d^2\mathbf{k}\,. \tag{2.31}$$

After a little algebra, finally one obtains for the phase space:

$$\int d\Pi = \frac{1}{8\pi^2 s}\int d^2\mathbf{k}\,. \tag{2.32}$$

The two tree level amplitudes in Eq. 2.28 are:

$$A^{(0)}(s,k^2) \;=\; -8\pi a_s (t^\alpha_{mj} t^\alpha_{nl})\frac{s}{\mathbf{k}^2} \tag{2.33}$$

and

$$A^{(0)\dagger}(s,(k-q)^2) \;=\; -8\pi a_s (t^\beta_{mi} t^\beta_{nk})^* \frac{s}{(\mathbf{k}-\mathbf{q})^2} \tag{2.34}$$

and thus the imaginary part of $A^{(0)}(s,t)$, with the help of Eq. 2.32, becomes:

$$Im A^{(1)}(s,t) \;=\; 4\alpha_s^2 \,(t^\alpha t^\beta)_{ij}\,(t^\alpha t^\beta)_{kl} s \int \frac{d^2\mathbf{k}}{\mathbf{k}^2(\mathbf{k}-\mathbf{q})^2}\,. \tag{2.35}$$

By dispersion relations we can reconstruct the full amplitude which is:

$$A^{(1)}(s,t) \;=\; -4\frac{\alpha_s^2}{\pi}\,(t^\alpha t^\beta)_{ij}\,(t^\alpha t^\beta)_{kl} \ln(\frac{s}{t}) s \int \frac{d^2\mathbf{k}}{\mathbf{k}^2(\mathbf{k}-\mathbf{q})^2}\,. \tag{2.36}$$

We remind that we are tracing leading logarithms in s, and since $\frac{s}{t} < 0$ we can write for a generic amplitude $\mathcal{A}$:

$$\mathcal{A} = Re\mathcal{A} + iIm\mathcal{A} \sim \mathcal{B}\ln\frac{s}{t} = \mathcal{B}\ln\frac{s}{|t|} - i\pi\mathcal{B} \tag{2.37}$$

which finally means $Re\mathcal{A} \;=\; -\frac{1}{\pi}\, Im\mathcal{A}\, \ln\frac{s}{|t|}$. Thus, after defining

$$\epsilon(t) = \frac{N_c\alpha_s}{4\pi^2} \int -\mathbf{q}^2 \frac{d^2\mathbf{k}}{\mathbf{k}^2(\mathbf{k}-\mathbf{q})^2}\,, \tag{2.38}$$

we can rewrite Eq. 2.36 as

$$A^{(1)}(s,t) \;=\; -\frac{16\pi\alpha_s}{N_c}\,(t^\alpha t^\beta)_{ij}\,(t^\alpha t^\beta)_{kl}\frac{s}{t}\,\ln(\frac{s}{t})\,\epsilon(t)\,, \tag{2.39}$$

whereas for the Fig. 2.12(b) diagram in the crossed channel it will be:

$$A^{(1)}_{cross}(s,t) \;=\; -\frac{16\pi\alpha_s}{N_c}\,(t^\alpha t^\beta)_{ij}\,(t^\alpha t^\beta)_{kl}\frac{u}{t}\,\ln(\frac{u}{t})\,\epsilon(t)\,. \tag{2.40}$$

By adding the last two relations and keeping in mind that $u \simeq -s$ we obtain the full one loop amplitude. Considering colour octet exchange, we can have the one loop amplitude in terms of the tree level one as

$$A^{(1)}_8(s,t) = 8\pi a_s t^\alpha_{ij} t^\alpha_{kl}\frac{s}{t}\,\ln(\frac{s}{|t|})\,\epsilon(t) \;=\; A^{(0)}\,\ln(\frac{s}{|t|})\,\epsilon(t)\,. \tag{2.41}$$

By going one level higher in corrections, in $\mathcal{O}(\alpha_s^3)$, we have to consider many Feynman diagrams like the ones in Fig. 2.14 but fortunately not all of them are accompanied by leading logarithms. Restricting ourselves at this point to only the virtual-gluon contributions, we must compute the diagrams in Fig. 2.15. Using Cutkosky rules again, we have at our disposal all the necessary elements to calculate the virtual corrections, namely contributions from graphs with qq as intermediate states, in terms of the Born

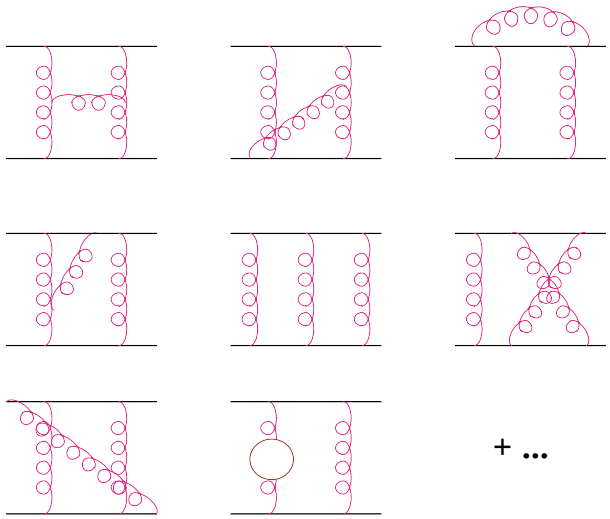

Figure 2.14: qq scattering, two loop diagrams.

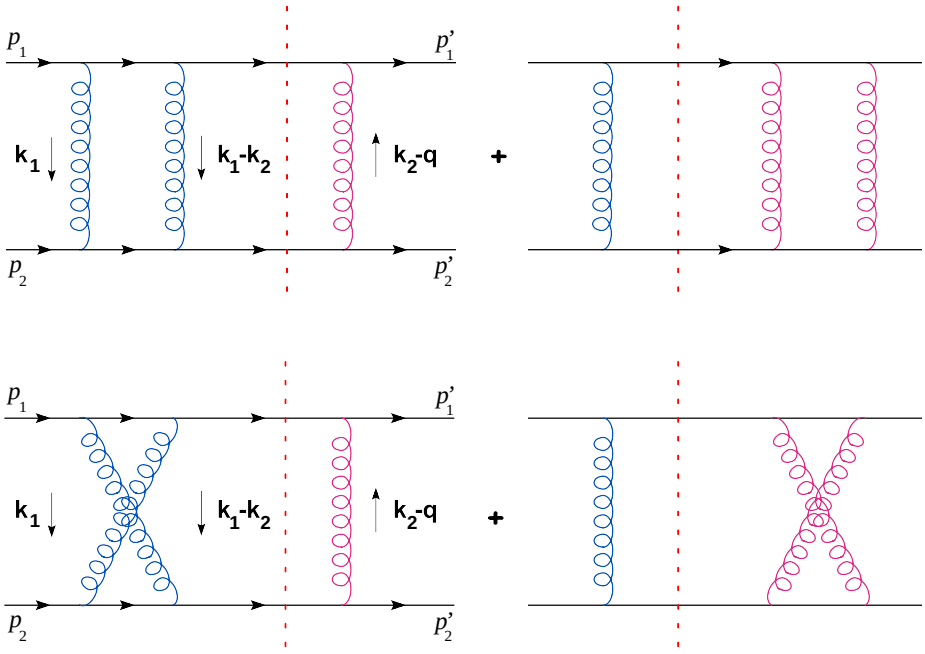

Figure 2.15: qq scattering, one loop virtual corrections.

one. After multiplying the amplitudes in the left hand side of the cut line with the hermitian conjugates of the ones in the right hand side, summing over helicities and integrating over the phase space without forgetting the on-shell conditions at the cut lines, we reach the result

$$A_8^{(2)}(s,t) = A^{(0)}(s,t)\,\frac{1}{2}\ln^2(\frac{s}{|t|})\,\epsilon^2(t)\,. \tag{2.42}$$

The form of $A_8^{(2)}(s,t)$ and $A_8^{(1)}(s,t)$ suggests that we can write the amplitude as an expansion:

$$A_8(s,t) = A^{(0)}(s,t)\,\left(1+\ln(\frac{s}{|t|})\,\epsilon(t)+\frac{1}{2}\ln^2(\frac{s}{|t|})\,\epsilon^2(t)+...\right)\,. \tag{2.43}$$

We make the ansatz that the above generalises to:

$$A_8(s,t) = A^{(0)}(s,t)\,\left(\frac{s}{|t|}\right)^{\epsilon(t)} \tag{2.44}$$

which is precisely the reggeization of the gluon. To see that, if we go back and calculate the tree amplitude for one gluon exchange using as a gluon propagator instead of the normal one the one from Eq. 2.22, taking also into account Eq. 2.26, we will then obtain exactly Eq. 2.44. To conclude with, our ansatz that considering the virtual gluon corrections leads to a modification of the gluon propagator (reggeization), which was based on the form of the first three orders of the expansion, is proven to be true to all orders by the so called *bootstrap* equation.

Let us now proceed to considering the contributions from the real gluon emission diagrams in Fig. 2.16. As we pointed out before, these are diagrams with qqg intermediate states, that carry $\ln s$ terms and the ones that we have to compute in LLA at $\mathcal{O}(\alpha_s^3)$. It turns out that instead of computing the amplitudes of all these diagrams it suffices to substitute their contribution by the diagram in Fig. 2.17 where the blob stands for the *Lipatov effective vertex* which is gauge invariant and has a tensor structure. The Lipatov effective vertex is an elegant way to sum over the contributions from the graphs in Fig. 2.16. Using once more Sudakov decomposition, the momenta of the two t-channel gluons are

$$\begin{aligned} k_1 &= \alpha_1 p_1 + \beta_1 p_2 + k_{1\perp} \\ k_2 &= \alpha_2 p_1 + \beta_2 p_2 + k_{2\perp}\,. \end{aligned} \tag{2.45}$$

The kinematical region of importance for our study (i.e. tracing the leading logarithms) is

$$\begin{aligned} 1 >> \alpha_1 >> \alpha_2 \\ 1 >> |\beta_2| >> |\beta_1| \end{aligned} \tag{2.46}$$

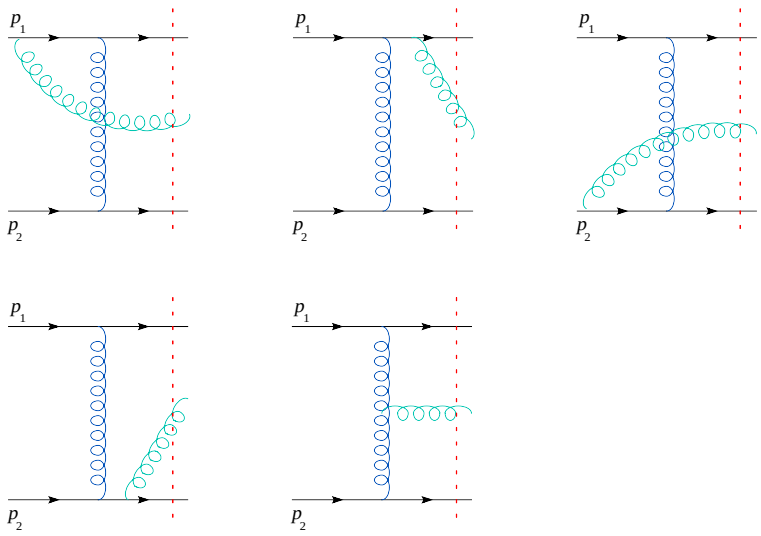

Figure 2.16: qq scattering with real gluon emission.

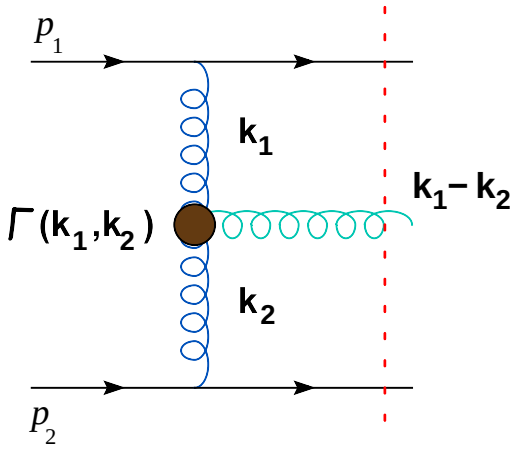

Figure 2.17: Lipatov effective vertex.

and again by using Cutkosky rules we contract the tree level amplitude from the diagram in Fig. 2.17 with its hermitian complex conjugate and we integrate over the three-body phase space. Now the three-body phase space after using Eq. 2.45 is

$$\int d\Pi_3 = \frac{s^2}{4(2\pi)^5} \int d\alpha_1 d\alpha_2 d\beta_1 d\beta_2 d^2\mathbf{k}_1 d^2\mathbf{k}_2 \\ \delta(-\beta_1(1-\alpha_1)s - \mathbf{k}_1^2)\ \delta(\alpha_2(1+\beta_2)s - \mathbf{k}_2^2) \\ \delta((\alpha_1-\alpha_2)(\beta_1-\beta_2)s - (\mathbf{k}_1-\mathbf{k}_2)^2)\,. \tag{2.47}$$

Because of Eq. 2.46 we can approximate

$$1-\alpha_1 \simeq 1, \\ 1+\beta_2 \simeq 1 \\ \alpha_1-\alpha_2 \simeq \alpha_1,\ \ \beta_1-\beta_2 \simeq -\beta_2\,. \tag{2.48}$$

Then Eq. 2.47 becomes

$$\int d\Pi_3 = \frac{s^2}{4(2\pi)^5} \int d\alpha_1 d\alpha_2 d\beta_1 d\beta_2 d^2\mathbf{k}_1 d^2\mathbf{k}_2 \\ \delta(-\beta_1 s - \mathbf{k}_1^2)\ \delta(\alpha_2 s - \mathbf{k}_2^2)\ \delta(-\alpha_1\beta_2 s - (\mathbf{k}_1-\mathbf{k}_2)^2)\,. \tag{2.49}$$

It is from the rightmost delta function in (Eq. 2.49) that the $\ln s$ behaviour of the real corrections arises. Indeed, after carrying out the integration over β_2, an $(1/\alpha_1)$ factor will be generated in the integrand:

$$\int d\Pi_3 = \frac{1}{4(2\pi)^5 s} \int_{\mathbf{k}_2^2/s}^1 \frac{d\alpha_1}{\alpha_1} \int d^2\mathbf{k}_1 d^2\mathbf{k}_2 \tag{2.50}$$

and finally performing the α_1 integration yields a factor

$$\ln\left(\frac{s}{\mathbf{k}_2^2}\right) = \ln\left(\frac{s}{s_0}\right), \tag{2.51}$$

where again s_0 is a typical momentum, a typical normalisation scale for the BFKL equation.

The previous discussion introduced us to the notion of reggeization and the logarithmic behaviour of the gluons that carry the interactions between the two reggeized gluons in the t-channel. It is now time to show how this knowledge can be incorporated in the general picture of a BFKL ladder in the colour singlet exchange, how by iterating the amplitude of a real gluon emission and using reggeized gluon propagators in the t-channel we construct the perturbative Pomeron. Let us consider the diagram in Fig 2.18. It consists of n rungs (real emitted gluons) connected to the t-channel

gluons via Lipatov effective vertices. The vertical gluons are subdivided into $n+1$ reggeized propagators. The imaginary part of the amplitude, $Im\mathcal{A}(s,t)$ for such a process will be given by contracting the two tree level amplitudes to the left and right hand side of the cut and after integrating over the $n+2$-body phase space. Again tracking leading logarithms only suggests a restriction of the kinematical configuration to the so-called *multi-Regge kinematics* (MRK):

$$\begin{aligned}
\mathbf{k}_1^2 \simeq \mathbf{k}_2^2 \simeq ... \mathbf{k}_i^2 \simeq \mathbf{k}_{i+1}^2 ... \simeq \mathbf{k}_n^2 \simeq \mathbf{k}_{n+1}^2 \gg \mathbf{q}^2 \simeq s_0, \\
1 \gg \alpha_1 \gg \alpha_2 \gg ... \alpha_i \gg \alpha_{i+1} \gg \alpha_{n+1} \gg \frac{s_0}{s}, \\
1 \gg |\beta_{n+1}| \gg |\beta_n| \gg ... \gg |\beta_2| \gg |\beta_1| \gg \frac{s_0}{s}\,. \qquad (2.52)
\end{aligned}$$

The integration over the phase space is nested and the way to turn the multi-nested integral into a product of integrals is by working in the complex angular momentum space ω by taking the Mellin transform of $Im\mathcal{A}(s,t)$

$$f(\omega,t) \,=\, \int_1^\infty d\left(\frac{s}{s_0}\right)\left(\frac{s}{s_0}\right)^{-\omega-1}\frac{Im\mathcal{A}(s,t)}{s}\,. \qquad (2.53)$$

Starting from $f(\omega,t)$, we can further define a function $f_\omega(\mathbf{k}_1,\mathbf{k}_2,t)$ which as its arguments indicate, is the Mellin transform of the amplitude with the integrations over the transverse momenta $\mathbf{k}_1$ and $\mathbf{k}_2$ still to be performed. This is called BFKL Green's function. Since $t \simeq -\mathbf{q}^2$, we will prefer in the following the notation $f_\omega(\mathbf{k}_1,\mathbf{k}_2,\mathbf{q}^2)$ in which we contain the propagators ${\mathbf{k_1}}^2$ and $(q-\mathbf{k_2})^2$ and $\mathbf{q}^2$ stands for the momentum transfer. By taking $n=1$ in the ladder diagram in Fig. 2.18 and calculating the corresponding $f_\omega^{(1)}(\mathbf{k}_1,\mathbf{k}_2,\mathbf{q}^2)$ function and then setting $n=2$ and calculating the $f_\omega^{(2)}(\mathbf{k}_1,\mathbf{k}_2,\mathbf{q})$ and generally iterating this procedure one realizes that there exists an integral equation which governs the behaviour of f_ω:

$$\begin{aligned}
\omega f_\omega(\mathbf{k}_1,\mathbf{k}_2,\mathbf{q}) = \delta^2(\mathbf{k}_1-\mathbf{k}_2) \\
+\frac{\bar{\alpha_s}}{2\pi}\int d^2\mathbf{l}\Bigg\{\frac{-\mathbf{q}^2}{(\mathbf{l}-\mathbf{q})^2\mathbf{k}_1^2}f_\omega(\mathbf{l},\mathbf{k}_2,\mathbf{q}) \\
+\frac{1}{(\mathbf{l}-\mathbf{k}_1)^2}\left(f_\omega(\mathbf{l},\mathbf{k}_2,\mathbf{q}^2)-\frac{\mathbf{k}_1^2 f_\omega(\mathbf{k}_1,\mathbf{k}_2,\mathbf{q})}{\mathbf{l}^2+(\mathbf{k}_1-\mathbf{l})^2}\right) \\
+\frac{1}{(\mathbf{l}-\mathbf{k}_1)^2}\Bigg(\frac{(\mathbf{k}_1-\mathbf{q})^2\mathbf{l}^2 f_\omega(\mathbf{l},\mathbf{k}_2,\mathbf{q}^2)}{(\mathbf{l}-\mathbf{q})^2\mathbf{k}_1^2} \\
-\frac{(\mathbf{k}_1-\mathbf{q})^2 f_\omega(\mathbf{k}_1,\mathbf{k}_2,\mathbf{q}^2)}{(\mathbf{l}-\mathbf{q})^2(\mathbf{k}_1-\mathbf{l})^2}\Bigg)\Bigg\}\,, \qquad (2.54)
\end{aligned}$$

with $\bar{\alpha_s} = N_c\alpha_s/\pi$. In the case of zero momentum transfer, $\mathbf{q^2}=0$, Eq.

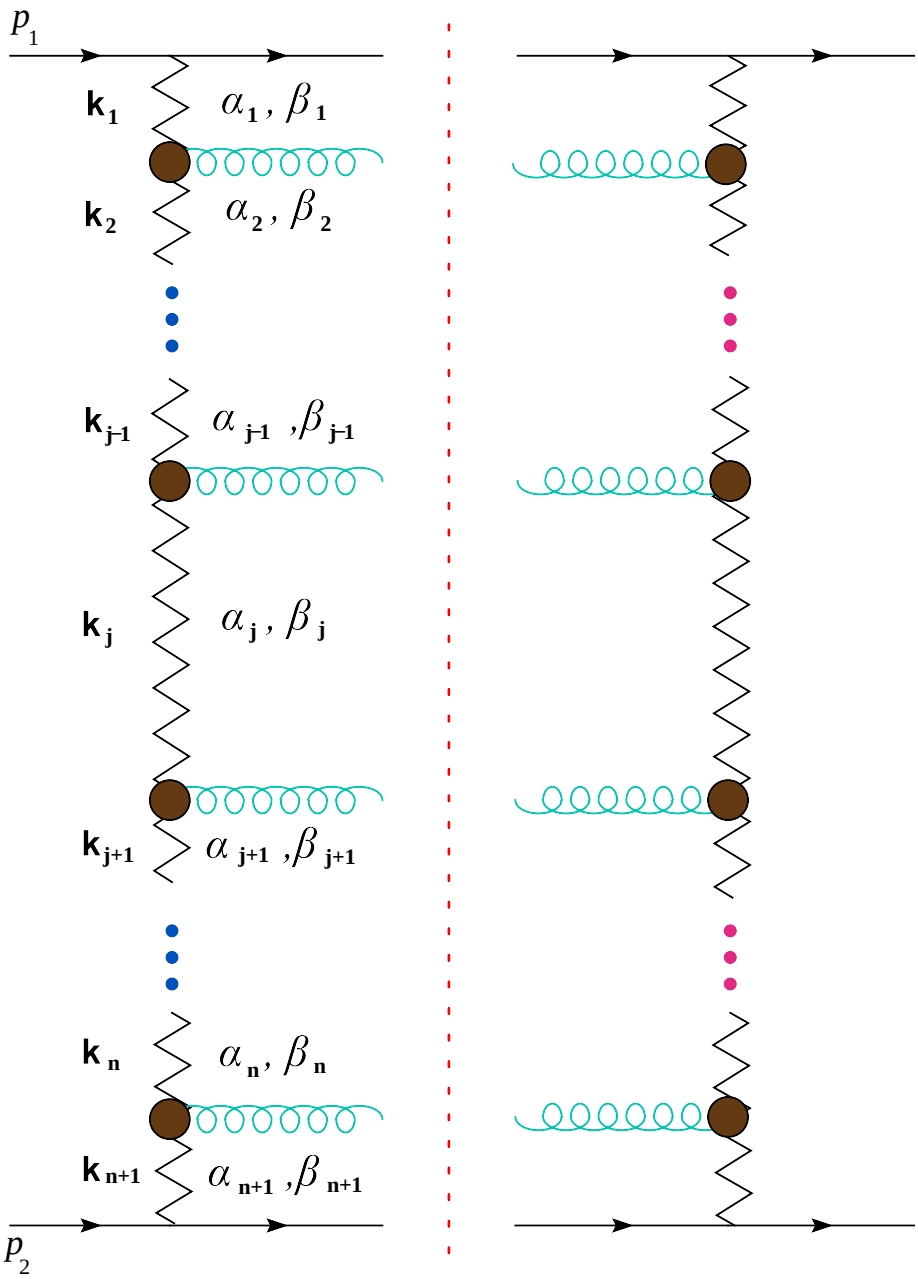

Figure 2.18: Gluonic ladder diagram.

2.54 becomes:

$$\omega f_\omega(\mathbf{k}_1,\mathbf{k}_2) = \delta^2(\mathbf{k}_1-\mathbf{k}_2) + \frac{\bar{\alpha_s}}{2\pi}\int \frac{d^2\mathbf{l}}{(\mathbf{l}-\mathbf{k}_1)^2}\left(f_\omega(\mathbf{l},\mathbf{k}_2) - \frac{\mathbf{k}_1^2 f_\omega(\mathbf{k}_1,\mathbf{k}_2)}{\mathbf{l}^2+(\mathbf{k}_1-\mathbf{l})^2}\right),. \tag{2.55}$$

We can rewrite the equation above very nicely as

$$\omega f_\omega(\mathbf{k}_1,\mathbf{k}_2) = \delta^2(\mathbf{k}_1-\mathbf{k}_2) + \int d^2\mathbf{l}\,\mathcal{K}(\mathbf{k}_1,\mathbf{l})\,f_\omega(\mathbf{l},\mathbf{k}_2)\,, \tag{2.56}$$

where $\mathcal{K}(\mathbf{k}_1,\mathbf{l})$ is the BFKL kernel:

$$\mathcal{K}(\mathbf{k}_1,\mathbf{l}) \;=\; \underbrace{2\epsilon(-\mathbf{k}_1^2)\,\delta^2(\mathbf{k}_1-\mathbf{l})}_{\mathcal{K}_{virt}} + \underbrace{\frac{N_c\alpha_s}{2\pi^2}\,\frac{1}{(\mathbf{k}_1-\mathbf{l})^2}}_{\mathcal{K}_{real}}\,. \tag{2.57}$$

$\mathcal{K}_{virt}$ and $\mathcal{K}_{real}$ are the parts of the kernel that correspond to the virtual and real corrections respectively.

Solving BFKL equation will provide us with the BFKL Green's function from which we can reconstruct the imaginary part of the amplitude for $q\,q$ scattering in two steps. Firstly, we will need to take the inverse Mellin transform and go back to s space:

$$f(s,\mathbf{k}_1,\mathbf{k}_2,\mathbf{q}) \;=\; \frac{1}{2\pi i}\int_{c-i\infty}^{c+i\infty} d\omega\,\left(\frac{s}{s_0}\right)^\omega\, f_\omega(\mathbf{k}_1,\mathbf{k}_2,\mathbf{q}) \tag{2.58}$$

and subsequently to perform the integrations over the $\mathbf{k}_1$ and $\mathbf{k}_2$ momenta of the reggeized gluons:

$$\mathcal{A}_{singlet}(s,t) = i(8\pi\alpha_s)^2\,s\,\frac{N_c^2-1}{4N_c^2}\int\frac{d^2\mathbf{k}_1}{(2\pi)^2}\,\frac{d^2\mathbf{k}_2}{(2\pi)^2}\,\frac{f(s,\mathbf{k}_1,\mathbf{k}_2,\mathbf{q})}{\mathbf{k}_2^2(\mathbf{k}_1-\mathbf{q})^2}\,. \tag{2.59}$$

The left hand side of Eq. 2.59 is not $Im\mathcal{A}(s,t)$ as one would expect, because the amplitude is purely imaginary for colour singlet exchange and thus $\mathcal{A}(s,t) \;=\; i\,Im\mathcal{A}(s,t)$.

Let us consider once more Eq. 2.59. The BFKL kernel Eq. 2.57 is infrared finite, the $\mathcal{K}_{real}$ and $\mathcal{K}_{virt}$ are singular but their divergencies cancel one against the other. The amplitude though is still infrared divergent due to the gluon propagators $\frac{1}{\mathbf{k}_2^2}$ and $\frac{1}{(\mathbf{k}_1-\mathbf{q})^2}$. In practice, the quarks (or scattering gluons) are not on mass-shell as we assumed here in sketching the derivation of BFKL equation. In physical processes, as for example hadron hadron collisions, the Pomeron couples to partons inside a hadron which are off shell. To take into account the structure of the hadrons we need the introduction of a quantity Φ which serves as the coupling of the Pomeron

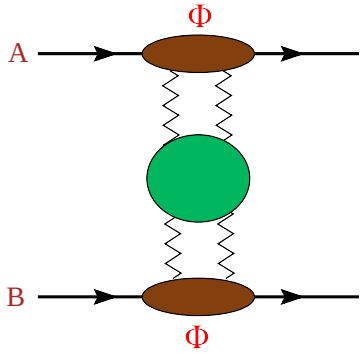

Figure 2.19: Regge factorisation for a generic hadronic process.

to the hadron and which is called *impact factor*. Then a hadronic elastic amplitude between hadrons A and B (Fig. 2.19) will be written as

$$\mathcal{A}(s,t) \;=\; i\,s\,\mathcal{C}\int \frac{d^2\mathbf{k}_1}{(2\pi)^2}\,\frac{d^2\mathbf{k}_2}{(2\pi)^2}\,\Phi_A(\mathbf{k}_1,\mathbf{q})\,\frac{f(s,\mathbf{k}_1,\mathbf{k}_2,\mathbf{q})}{\mathbf{k}_2^2(\mathbf{k}_1-\mathbf{q})^2}\Phi_B(\mathbf{k}_2,\mathbf{q})\,, \quad (2.60)$$

where $\mathcal{C}$ accounts for the colour factor[3] of the process and the quantities Φ_A and Φ_B are the hadron impact factors for the the hadrons A and B. Whenever we have scattering of particles with Pomeron exchange, we also have to consider impact factors for each of these particles. In general, impact factors are non perturbative objects, non-calculable and thus subjects to modelling. Nevertheless, all impact factors have to share a very important universal behaviour, i.e. they regulate the infrared divergencies:

$$\Phi(\mathbf{k},\mathbf{q})\Big|_{\mathbf{k}\to 0}^{\mathbf{k}-\mathbf{q}\to 0} \to 0\,. \quad (2.61)$$

In this way, they cancel the singular behaviour of Eq. 2.60 which exactly appears at these limits. Although the impact factors are non perturbative objects, there is at least a particle for which the impact factor falls into the realm of pQCD, namely the case of the virtual photon. The perturbative calculation of the photon impact factor will be the subject of the next Chapter. In the case of virtual photon scattering, the Eq. 2.60 which exhibits the Regge factorisation, becomes:

$$\begin{aligned}\sigma^{tot}_{\gamma^*\gamma^*} =& \frac{1}{(2\pi)^2}\int\frac{d^2\mathbf{r}}{\mathbf{r}^2}\int\frac{d^2\mathbf{r}'}{\mathbf{r}'^2}\\ &\times\Phi_A(\mathbf{r},s_0)\left[\int_{\delta-i\infty}^{\delta+i\infty}\frac{d\omega}{2\pi i}\left(\frac{s}{s_0}\right)^{\omega} f_\omega(\mathbf{r},\mathbf{r}',s_0)\right]\Phi_B(\mathbf{r}',s_0)\,, \quad (2.62)\end{aligned}$$

[3]For example, $\mathcal{C}=(N_c^2-1)/4N_c^2$ for $q\,q$ scattering

where we changed notation from **k** to **r** for the reggeized gluon momenta. To get the solution to (2.56), we could rewrite it in a symbolic form as

$$\omega F \;=\; \mathbb{1} + \mathcal{K} \;\otimes\; F\,, \tag{2.63}$$

with $\mathcal{K}$ being the BFKL kernel from Eq. 2.57, and try to attempt to diagonalise the BFKL equation by finding the eigenfunctions ϕ_a of the kernel $\mathcal{K}$:

$$\mathcal{K} \otimes \phi_a \;=\; \omega_a \phi_a\,. \tag{2.64}$$

If θ is the azimuthal polar coordinate of the momenta, then the eigenfunctions can be expressed as:

$$\phi_{n\nu}(|\boldsymbol{k}|,\theta) \;=\; \frac{1}{\pi\sqrt{2}}(\boldsymbol{k}^2)^{-\frac{1}{2}+i\nu}\, e^{in\theta}\,. \tag{2.65}$$

The high energy behaviour of the total cross section is determined when we consider the angular averaged kernel (averaged over the azimuthal angle between $\boldsymbol{k}_1$ and $\boldsymbol{k}_2$) and then $(\boldsymbol{k}_2^2)^{\gamma-1}$ can be used as eigenfunctions such that:

$$\int d^2k\, \mathcal{K}(\boldsymbol{k}_1,\boldsymbol{k})(\boldsymbol{k}^2)^{\gamma-1} = \frac{N_c\alpha_s}{\pi}\,\chi_0(\gamma)(\boldsymbol{k}_1^2)^{\gamma-1} \tag{2.66}$$

with the eigenvalues

$$\chi_0(\gamma) = 2\psi(1) - \psi(\gamma) - \psi(1-\gamma), \qquad \psi(\gamma) = \Gamma'(\gamma)/\Gamma(\gamma)$$

and $\gamma = 1/2 + i\nu$. The set of eigenfunctions, where the real ν ranges between $-\infty$ and ∞ is complete. The power rise of the total cross section then is given by the eigenvalue $\chi(\gamma = 1/2) = 4\ln 2$. Finally, one obtains the result that we have already mentioned in the introduction:

$$\omega_{BFKL} = \frac{4N_c \ln 2}{\pi}\,.$$

One is bound to think whether taking higher order corrections, that is beyond LLA, can change this value drastically.

2.4 BFKL at NLLA

At next-to-leading logarithmic approximation (NLLA) the new terms that have to be resumed in addition are terms like $\alpha_s(\alpha_s \ln s)^n$. As in LLA, the reggeization of the gluon also holds in NLLA. This is a key point in the analysis, due to which one can use the same formula for the NLO BFKL equation as for the leading order one, with different kernels and eigenvalues

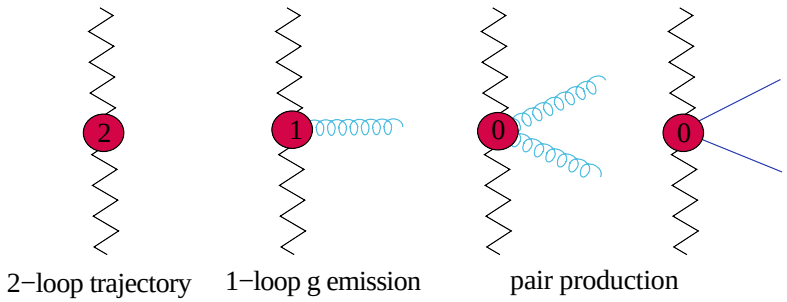

Figure 2.20: Contributions to the NLL approximation.

of course [8]. From now on, when the approximation is at NLLA level, we will prefer the term NLO BFKL equation, instead of NLLA.

There are two sources of contributions to the NLO corrections: from MRK and from another kinematical configuration that we call *Quasi-Multi-Regge-Kinematics* (QMRK). In MRK, the next-to-leading order corrections for the gluon trajectory and the RRG vertex have to be included. So, the reggeized gluon trajectory has to be calculated in two loop approximation, $\epsilon^{(2)}$ [26], whereas, the real part of the kernel, $\mathcal{K}_{real}$ gets contributions from one-loop level gluon production [27].

A different way to obtain a term of the type $\alpha_s(\alpha_s \ln s)^n$ is to lose a logarithm of s starting from an amplitude at LLA. As we saw in the previous Section, the key feature that generates these logarithmic terms is the strong ordering in rapidity. Thus, if we allow for a state where two of the emitted particles are close to each other, we are in the Quasi-Multi-Regge-kinematics (QMRK): Eq. 2.52 still holds with the exception of a pair of particles. The pair can be a pair of gluons but now we can aslo have a $q\bar{q}$ pair so the vertices ($reggeon\, reggeon\, g\, g$) [28] and ($reggeon\, reggeon\, q\, q$) [29] were computed. A pictorial demonstration of the corrections at NLLA are shown in Fig. 2.20

The project of computing the next-to-leading corrections was an impressive feat that took almost ten years to finish [8, 9]. When it was completed, in the late nineties, it came as a surprise that the corrections compared to LLA were very large with the discouraging feature that they even led to a negative intercept for moderate α_s. Various studies [10] had shown that the reason for such a behaviour had its origin in the two particle production in QMRK.

Since we impose no restrictions on the values of the transverse momenta for the emissions, there can be final configurations possible where the transverse momenta of the pair of particles are strongly ordered. This leads to large logarithms of transverse momenta (collinear logarithms) that make the expansion in $\alpha_s \ln s$ unstable. To eliminate these unphysical logarithms one can perform a complete DGLAP resummation of these large logarithms

which stabilizes the convergence of the expansion [30]. In that way, we are led to an effective change in the dependence of $\omega_{\rm BFKL}$ on α_s. For a typical value $\alpha_s = 0.2$, the intercept turns out to vary between 0.3 and 0.4, which is a promising result for applying NLO BFKL to phenomenology.

Apart from the renormalisation group improved kernel, another solution to the problem, and the one which we will discuss in more detail here as we will later use it in the second half of this thesis, originates from L. Lipatov [21]. The idea is to impose a a restriction in the rapidity separation of the produced particles, the so called *rapidity veto effect* [21, 22, 23]. Application of the rapidity veto leads to the same results comparing with the ones obtained from the collinear ressumed kernel.

The technical idea behind the rapidity veto is based on the artificial suppression of the emission of gluons which are close in rapidity along the BFKL ladder (Fig. 2.21). As we have seen, the logarithms in s arise from the integration over the rapidities of the real and virtual gluons. At LL accuracy, the limits of these rapidity integrations (arising from the integration over phase space, as for example in Eq. 2.47) cannot be precisely defined. In other words, we are allowed to shift the limits of integration by a small parameter and still be within the validity of the LL approximation. If the shift parameter, let us name it η, is much smaller compared to the whole rapidity interval, $\eta \ll s$ then any modification that can possibly enter our result after the integration over rapidities, will have to be beyond LL accuracy. In physical terms, this parameter can only be realized as a separation in rapidity space between two subsequent gluon emissions (with rapidities Y_i and Y_{i+1}) along the gluonic ladder, as in Fig 2.21, namely on top of all the other requirements for the BFKL resummation, an additional constraint must be taken into account: $\mathrm{Y}_{i+1} - \mathrm{Y}_i > \eta$, where η is the so called *veto parameter*. Another way to look upon the whole procedure is to think that we are allowed to redefine the energy that scales s in the logarithms, as long as we keep that scale much smaller than s. Studies ([22, 23]) have shown that a veto η with a value around 2 units of rapidity lowers the intercept from 0.5 down to 0.3 in consistency with the results from the collinearly ressumed kernel. Actually, if we keep in mind that most of the problematic behaviour of the NLO kernel originates at QMRK, when unphysical collinear logarithms appear and have to be eliminated, the 'regularizing' role of the veto should not come as a surprise. The standard BFKL equation is certainly obtained at the limit $\eta = 0$.

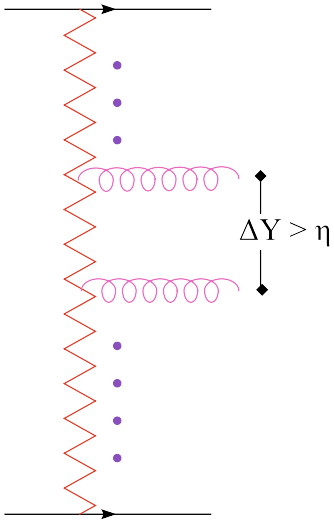

Figure 2.21: Imposing a rapidity veto for subsequent emissions.

Chapter 3

The NLO Photon Impact Factor

In this Chapter we will firstly introduce the LO impact factor in order to define our notation and to gain an intuitive idea of what the γ^* impact factor at NLO will be. We will discuss in brief the previously achieved results of the NLO computation. We will finally present the newly obtained results for the virtual contributions, namely, the numerical integration over phase space. It has to be stressed that in this thesis, we deal with the numerical implementation for the case only of longitudinally polarized photons.

We are primarily interested in $\gamma^*\gamma^*$ scattering. The building block we need in order to calculate the first approximation of $\sigma^{total}_{\gamma^*\gamma^*}$ at fixed order, is the $\gamma^* g$ vertex at LO, see Fig 3.1. Then, using the optical theorem (s-channel discontinuity) and projecting in the colour singlet, we need simply to calculate the imaginary part of the diagram in Fig. 3.2 since for the general scattering between A and B particles it is

$$\sigma^{(0)}_{AB} = \frac{1}{s} Im T^{(0)}_{AB}(s, t = 0)\,. \tag{3.1}$$

The blobs at the points where the photons split into a $q\bar{q}$ pair are merely

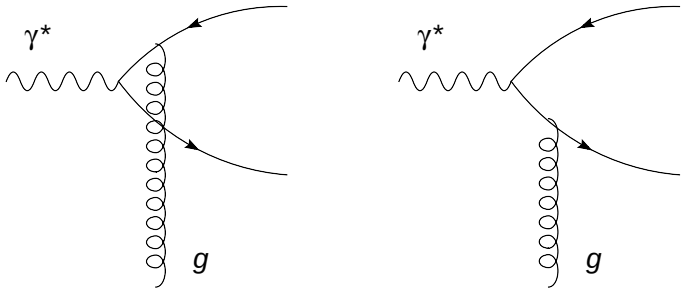

Figure 3.1: $\gamma^* g$ vertex at LO

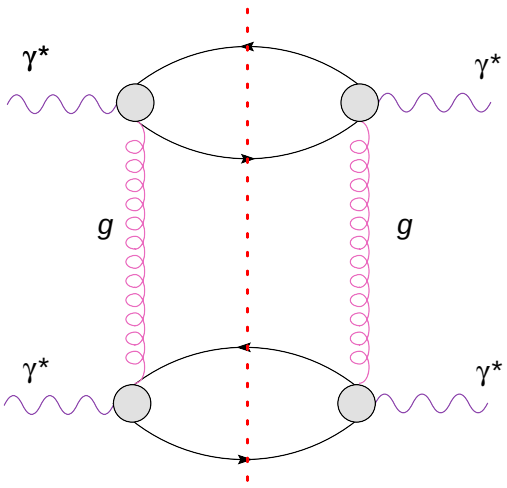

Figure 3.2: $\gamma^*\gamma^*$ at LO, fixed order

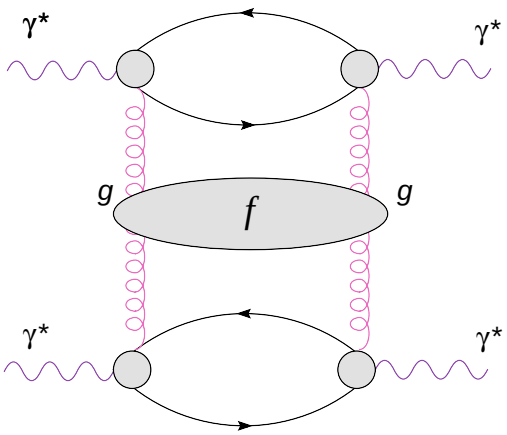

Figure 3.3: $\gamma^*\gamma^*$ at LO BFKL

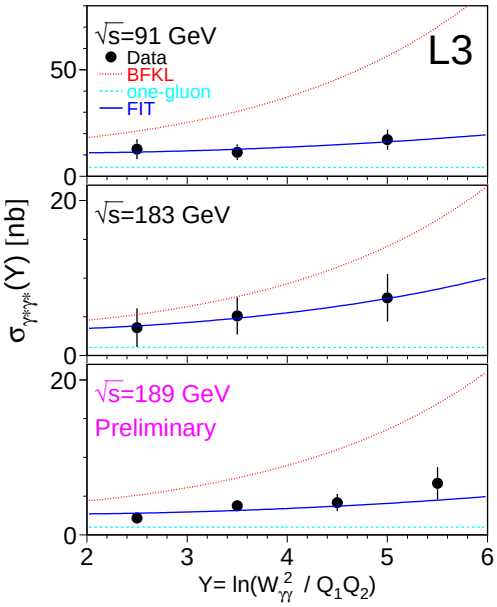

Figure 3.4: $\gamma^*\gamma^*$ total cross section from LEP [7].

denoting that the gluon can be coupled to the quark or the antiquark line. Unfortunately, such an attempt does not give a good description of the data behaviour. Data from LEP [7], shown in Fig. 3.4, indicate a rise with energy and more precisely they favour a rise like $W^{0.3}_{\gamma^*\gamma^*}$. The fixed order calculation sketched above predicts a flat behaviour in energy as it can be seen in the same figure, whereas a LO BFKL calculation (Fig. 3.3) clearly overshoots the data.

Nevertheless, Fig. 3.1 will provide us with the basic notions in order to introduce the LO and NLO impact factor for the virtual photon, since the diagrams in that figure are the pictorial contributions of what we call photon wave function interacting with a gluon. They give the probability for the photon to split into a $q\bar{q}$ pair and further on, to interact strongly with the exchange of a gluon. The photon impact factor at LO will be (again by using the optical theorem) that probability squared, projected in the colour singlet and integrated over phase space. We usually denote the photon impact factor by $\Phi(Q^2, \boldsymbol{r}^2)$, where Q^2 is the virtuality of the photon and $\boldsymbol{r}^2$ the transverse momentum squared of the exchanged gluon. An additional superscript will denote the order in α_s, namely $\Phi^{(0)}(Q^2, \boldsymbol{r}^2)$ for LO and $\Phi^{(1)}(Q^2, \boldsymbol{r}^2)$ for NLO.

Summarising, the photon impact factor is a quantity that enters processes which invoke virtual photon scattering. It depends on the exchanged gluon momentum and the virtuality of the photon but not on s and should

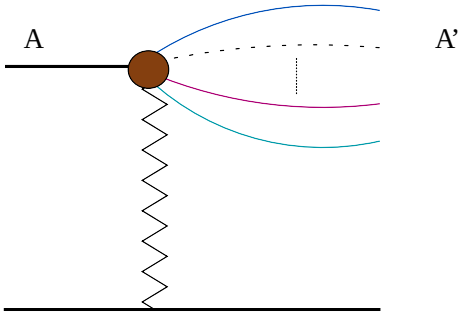

Figure 3.5: An auxiliary process that can be used to calculate the impact factor for A.

be considered as a 'partial cross section'. High energy factorisation implies that the total cross section will be a convolution (generally integration over the gluon momentum or momenta in the non-forward case) between the impact factors and a process independent part that carries all the energy dependence. In Fig. 3.3, the total cross section is a convolution between the gluon Green's function f and the upper and lower photon impact factors.

3.1 The LO impact factor

As we previously mentioned, the photon impact factor is obtained from the energy discontinuity of the amplitude $\gamma^* + reggeon \to \gamma^* + reggeon$. For the Born level ($\mathcal{O}(\alpha_s)$), this discontinuity is simply the square of the sum of the amplitudes from the Fig. 3.1, where the reggeon now is simply the t-channel gluon. For a general definition of the impact factor of a particle A, see Fig 3.5, we can state [15]:

$$\Phi_A = \frac{\delta^{ab}}{\sqrt{N_c^2-1}} \sum_{A'} \int \left\langle \Gamma^a_{A\to A'} \Gamma^{b\,*}_{A\to A'} \right\rangle d\phi_{A'} \frac{s d\beta_r}{2\pi}\,, \tag{3.2}$$

where summing over colour and helicity in the intermediate state A' is to be understood by the use of the $\langle\rangle$ notation whereas the factor $\frac{\delta^{ab}}{\sqrt{N_c^2-1}}$ is the colour projector. $d\phi_{A'}\frac{s d\beta_r}{2\pi}$ is the phase space measure for the A' intermediate state. Equivalently, in a short hand notation we could write

$$\Phi_A = \sum_{A'} \int |\Gamma_{A\to A'}|^2 d\phi_{A'} \frac{s d\beta_r}{2\pi} \tag{3.3}$$

including the colour projection in the square of the matrix elements. To calculate the LO photon impact factor and most importantly the NLO corrections, we will use an auxiliary process, namely $\gamma^* q$ scattering. This is

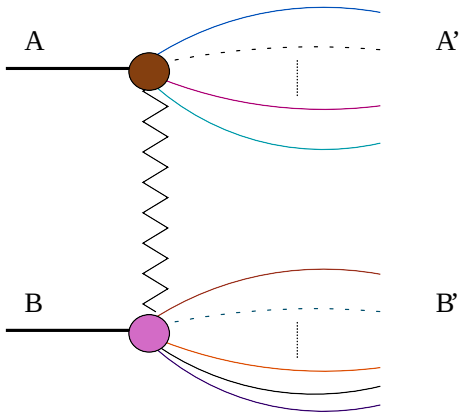

Figure 3.6: Generic $A + B \to A' + B'$ scattering

because, although we can represent the matrix elements for the Born piece of the impact factors in terms of Feynman diagrams (Fig. 3.1), there is not such a simple diagrammatic definition (in terms of Feynman diagrams) for the virtual photon at NLO as we will see later. One then needs to calculate the amplitude at NLO for $\gamma^* q$ and after 'stripping' all the irrelevant pieces of the calculated amplitude, one obtains the piece that will give the NLO corrections after the integration over phase space. Therefore, let us start by considering the scattering $\gamma^* + q' \to q\bar{q} + q'$ (Fig. 3.7)

The amplitude for this process, as an expansion in the strong coupling g, is

$$T_{\gamma^* q} = g^2 T^{(0)}_{\gamma^* q} + g^4 T^{(1)}_{\gamma^* q} \,. \tag{3.4}$$

This comes naturally after using the Regge ansatz. That is, in the high energy limit the amplitude for the scattering process $A + B \to A' + B'$ (Fig. 3.6) is described by the exchange of a reggeized gluon. It can then be cast into the following form:

$$\mathcal{M}_{AB} = \frac{s}{t}\, \Gamma^{\alpha}_{A\to A'} \left[\left(\frac{s}{-t} \right)^{\omega(t)} + \left(\frac{-s}{-t} \right)^{\omega(t)} \right] \Gamma^{\alpha}_{B\to B'} \,. \tag{3.5}$$

$\Gamma^{\alpha}_{A\to A'}$ and $\Gamma^{\alpha}_{B\to B'}$ are the particle-particle-reggeon vertices, $1 + \omega(t)$ is the Regge trajectory of the gluon[1] and the index α stands for the colour of the reggeized gluon. For the process at hand in Fig. 3.7, Eq. 3.5 becomes:

$$T_{\gamma^* q \to q\, q\bar{q}} = \frac{s}{t}\, \Gamma^{\alpha}_{\gamma^* \to q\bar{q}} \left[\left(\frac{s}{-t} \right)^{\omega(t)} + \left(\frac{-s}{-t} \right)^{\omega(t)} \right] \Gamma^{\alpha}_{qq} \,. \tag{3.6}$$

[1]The change of notation from $\epsilon(t)$ to $\omega(t)$ here is necessary to be in accordance with the series of papers of the previous steps of the NLO photon impact factor computation

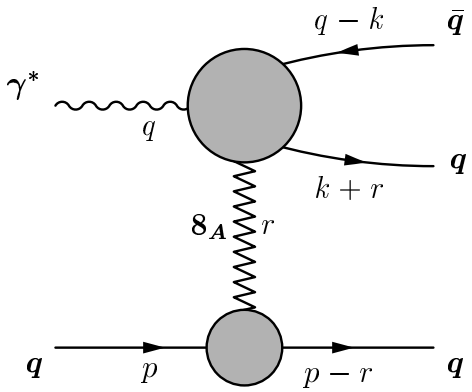

Figure 3.7: Kinematic variables for the process $\gamma^* + q' \to q\bar{q} + q'$.

Expanding in g, we will have:

$$\omega = g^2\omega^{(1)} + g^4\,\omega^{(2)}\,, \tag{3.7}$$

$$\Gamma^{\alpha}_{\gamma^*\to q\bar{q}} = g\,\Gamma^{(0),\alpha}_{\gamma^*\to q\bar{q}} + g^3\,\Gamma^{(1),\alpha}_{\gamma^*\to q\bar{q}}\,, \tag{3.8}$$

$$\Gamma^{\alpha}_{qq} = g\,\Gamma^{(0),\alpha}_{qq} + g^3\,\Gamma^{(1),\alpha}_{qq}\,. \tag{3.9}$$

Because of the last four equations, we can identify in Eq. 3.4:

$$T^{(0)}_{\gamma^* q} = \Gamma^{(0),\alpha}_{\gamma^*\to q\bar{q}}\,\frac{2s}{t}\,\Gamma^{(0),\alpha}_{qq}\,, \tag{3.10}$$

and

$$T^{(1)}_{\gamma^* q} = \Gamma^{(1),\alpha}_{\gamma^*\to q\bar{q}}\,\frac{2s}{t}\,\Gamma^{(0),\alpha}_{qq} + \Gamma^{(0),\alpha}_{\gamma^*\to q\bar{q}}\,\frac{2s}{t}\,\Gamma^{(1),\alpha}_{qq} + \Gamma^{(0),\alpha}_{\gamma^*\to q\bar{q}}\,\frac{s}{t}\omega^{(1)}\left[\ln\frac{s}{-t} + \ln\frac{-s}{-t}\right]\,\Gamma^{(0),\alpha}_{qq}\,. \tag{3.11}$$

At Born approximation, we just keep the first term of the right hand side of Eq. 3.4. The kinematical variables we will use in our calculation, are as usual, q and p for the four momenta of the photon and the incoming quark, the centre-of-mass energy s of the $\gamma^* q$ scattering process, the photon virtuality $Q^2 = -q^2$ and the Bjorken scaling variable $x = Q^2/2p\cdot q$. It will serve us well in the future, when discussing the NLO virtual corrections, to introduce some notation for the invariants of the process at a general level, so we will denote the momentum transfers, as depicted in Fig. 3.8, by $t = r^2$, $t_a = k^2$ and $t_b = (q-k-r)^2$, whereas M^2 is the invariant mass of the outgoing $q\bar{q}$-system. The momenta k and r can be written in a Sudakov decomposition form with respect to the light cone momenta $q' = q - xp$ and p with $2p\cdot q' = s$:

$$k = \alpha q' + \beta p + k_\perp,\;\; r = \frac{t}{s}q' - \frac{t_a + t_b}{s}p + r_\perp\,. \tag{3.12}$$

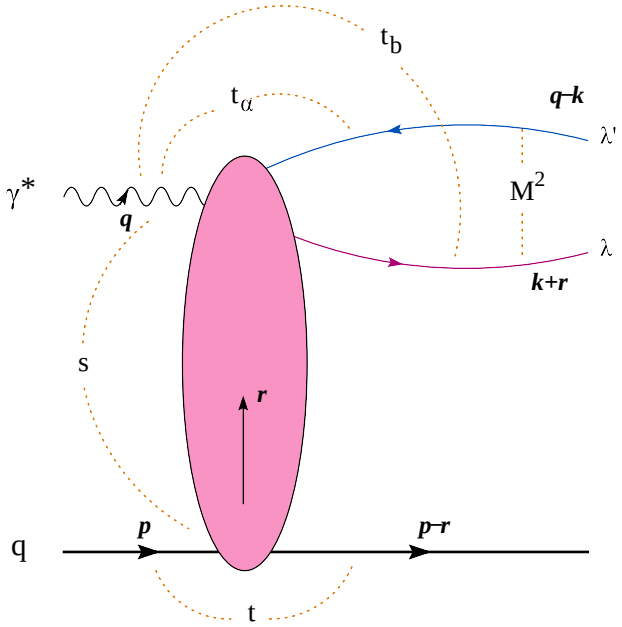

Figure 3.8: Invariants for the process $\gamma^* + q \to q\bar{q} + q$.

Two dimensional transverse momenta are denoted as $\boldsymbol{k}^2 = -k_\perp^2$ and $\boldsymbol{r}^2 = -r_\perp^2$. We stress once more that we are working in the high energy limit (Regge limit):

$$t,\, Q^2,\, t_a,\, t_b,\, M^2 \ll s\,. \tag{3.13}$$

Let us see how the Born impact factor can be obtained from $T^{(0)}_{\gamma^* q}$. At leading order we may write, due to the reggeization of the t-channel gluon,

$$T^{(0)}_{\gamma^* q} = \Gamma^{(0),a}_{\gamma^* \to q\bar{q}}\, \frac{2s}{t}\, \Gamma^{(0),a}_{qq}\,, \tag{3.14}$$

with the Born level vertices being

$$\Gamma^{(0),a}_{qq} = \frac{1}{s}\bar{u}(p-r,\,\lambda_{q'})\;\not{q}'\lambda^a u(p,\,\lambda_q)\,, \tag{3.15}$$

$$\Gamma^{(0),a}_{\gamma^* \to q\bar{q}} = -iee_f\left(\frac{H^a_T}{st_a} - \frac{\bar{H}^a_T}{st_b}\right). \tag{3.16}$$

The helicity formalism is used and the matrix elements H^a_T and $\bar{H}^a_T$ are defined as:

$$H^a_T = \bar{u}(k+r,\lambda)\;\not{p}\,\not{k}\,\not{\varepsilon}\,\lambda^a v(q-k,\lambda')\,, \tag{3.17}$$

$$\bar{H}^a_T = \bar{u}(k+r,\lambda)\;\not{\varepsilon}\,(\not{q} - \not{k} - \not{r})\;\not{p}\,\lambda^a v(q-k,\lambda')\,, \tag{3.18}$$

with the λ^a being the generators of the colour group $SU(N_c)$ and the e_f the electric charge of the lower quark.

After squaring the Born level vertex (Eq. 3.16) and averaging (summing) over incoming (outgoing) colours and helicities we finally obtain:

$$|\Gamma^{(0)}_{\gamma^*\to q\bar{q}}|^2_L = 4\sqrt{N_c^2-1}e^2e_f^2\alpha^3(1-\alpha)^3Q^2\left(\frac{1}{D(\boldsymbol{k})}-\frac{1}{D(\boldsymbol{k}+\boldsymbol{r})}\right)^2, \quad (3.19)$$

for a longitudinally polarised photon, where $D(\boldsymbol{k}) = \boldsymbol{k}^2 + \alpha(1-\alpha)Q^2$. Respectively, the sum over the two transverse photon polarisations is given by

$$|\Gamma^{(0)}_{\gamma^*\to q\bar{q}}|^2_T = 2\sqrt{N_c^2-1}e^2e_f^2\alpha(1-\alpha)\left[\alpha^2+(1-\alpha)^2\right]\left(\frac{\boldsymbol{k}}{D(\boldsymbol{k})}-\frac{\boldsymbol{k}+\boldsymbol{r}}{D(\boldsymbol{k}+\boldsymbol{r})}\right)^2. \quad (3.20)$$

The LO impact factor then, using Eq. 3.3, and the fact that the two-particle phase space measure is

$$d\phi_{q\bar{q}}\frac{sd\beta_r}{2\pi} = \frac{d\alpha}{2\alpha(1-\alpha)}\frac{d^{D-2}\boldsymbol{k}}{(2\pi)^{D-1}} \quad (3.21)$$

will be (we keep the spacetime dimensions D for later consistency):

$$\Phi^{(0)}_{\gamma^*;T,L} = \int\frac{d^{D-2}\boldsymbol{k}}{(2\pi)^{D-1}}\frac{d\alpha}{2\alpha(1-\alpha)}|\Gamma^{(0)}_{\gamma^*\to q\bar{q}}|^2_{T,L} \quad (3.22)$$

or equivalently

$$\Phi^{(0)}_{\gamma^*;T,L} = \int d^{D-2}\boldsymbol{k}\, d\alpha\, \mathcal{I}_{2;T,L}(\alpha,\boldsymbol{k};\boldsymbol{r},Q)\,. \quad (3.23)$$

where it is

$$\mathcal{I}_{2;L}(\alpha,\boldsymbol{k};\boldsymbol{r},Q) = \frac{2e^2e_f^2\sqrt{N_c^2-1}}{(2\pi)^{D-1}}\alpha^2(1-\alpha)^2Q^2\left(\frac{1}{D(\boldsymbol{k})}-\frac{1}{D(\boldsymbol{k}+\boldsymbol{r})}\right)^2 \quad (3.24)$$

and

$$\mathcal{I}_{2;T}(\alpha,\boldsymbol{k};\boldsymbol{r},Q) = \frac{e^2e_f^2\sqrt{N_c^2-1}}{(2\pi)^{D-1}}\left[\alpha^2+(1-\alpha)^2\right]\left(\frac{\boldsymbol{k}}{D(\boldsymbol{k})}-\frac{\boldsymbol{k}+\boldsymbol{r}}{D(\boldsymbol{k}+\boldsymbol{r})}\right)^2. \quad (3.25)$$

As we previously mentioned , it is only for the case of longitudinally polarised photons that we will present numerical results in this thesis, so in our analysis from now on, we will concentrate on that polarisation configuration.

One very important feature of $\Phi^{(0)}_{\gamma^*;L}(Q^2,\boldsymbol{r}^2)$ is that it is dimensionless. This comes formally from the fact that it presents a scaling property, namely

it is not a function of Q^2 and $\boldsymbol{r}^2$ seen independently, but a function of their ratio:

$$\Phi^{(0)}_{\gamma^*;L}(Q^2, \boldsymbol{r}^2) \equiv \Phi^{(0)}_{\gamma^*;L}(\frac{\boldsymbol{r}^2}{Q^2}) \,. \tag{3.26}$$

This fact and the symmetry of the squared matrix elements under the exchange $q \leftrightarrow \bar{q}$, namely $\alpha \leftrightarrow 1-\alpha$, $\boldsymbol{k} \leftrightarrow -\boldsymbol{r}-\boldsymbol{k}$, which translates into

$$\mathcal{I}_2(\alpha, \boldsymbol{k}; \boldsymbol{r}, Q) = \mathcal{I}_2(1-\alpha, -\boldsymbol{r}-\boldsymbol{k}; \boldsymbol{r}, Q) \,, \tag{3.27}$$

are very important to keep in mind in the following, when we will discuss numerical checks of the integration over phase space for the virtual corrections. After integrating Eq. 3.27 over $\boldsymbol{k}$, we get a relation with a $\alpha \leftrightarrow 1-\alpha$ symmetry:

$$\phi(\alpha, \boldsymbol{r}, Q) = \phi(1-\alpha, \boldsymbol{r}, Q) \,, \tag{3.28}$$

where now ϕ is a function with still the α integration to be done.

Fig. 3.9 shows a plot of the Born photon impact factor as a function of $\boldsymbol{r}^2/Q^2$. In this plot, we used $Q^2 = 15$ GeV^2 for the photon virtuality which will give a typical value of the strong coupling $\alpha_s \approx 0.18$ and we varied $\mathbf{r}^2$. In the limit $\boldsymbol{r} \to 0$, Q^2 fixed, the Born impact factor dies off like $\Phi^{(0)} \sim \boldsymbol{r}^2$, so the impact factor regulates the total cross section in the infrared limit as we saw in the Chapter 2. We get the same limit when we assume $Q^2 \to \infty$, $\boldsymbol{r}^2$ fixed. The large virtuality of the photon translates into a very small transverse size of the dipole $q\bar{q}$, so small that the dipole looks needlelike and the interaction cross section vanishes. If we imagine that the dipole interacts with a proton (DIS), the strength of the dipole-proton interaction is proportional to the dipole size. With a very small dipole, the proton will not be able to 'notice' it's colour charges. This is known as *colour transparency*.

3.2 NLO corrections

The NLO corrections to the photon impact factor can be represented in a pictorial way as in Fig. 3.10. The project of calculating them was divided into steps. Firstly, analytic results were obtained for the one loop corrections to the coupling of the reggeized gluon to the $\gamma^* \to q\bar{q}$ vertex. The process used for that purpose was $\gamma^* + q \to q\bar{q} + q$ [13]. The next step was the calculation of the cross section of the process $\gamma^* + q \to q\bar{q}g + q$ with a large rapidity gap between the fragmentation system $q\bar{q}g$ and the other quark. From this calculation, the real corrections of the virtual photon impact factor in the next-to leading order were obtained [14, 15]. The cancellation of infrared divergencies when combining the real and virtual parts was demonstrated in Ref. [15], while the renormalisation of the ultraviolet divergencies

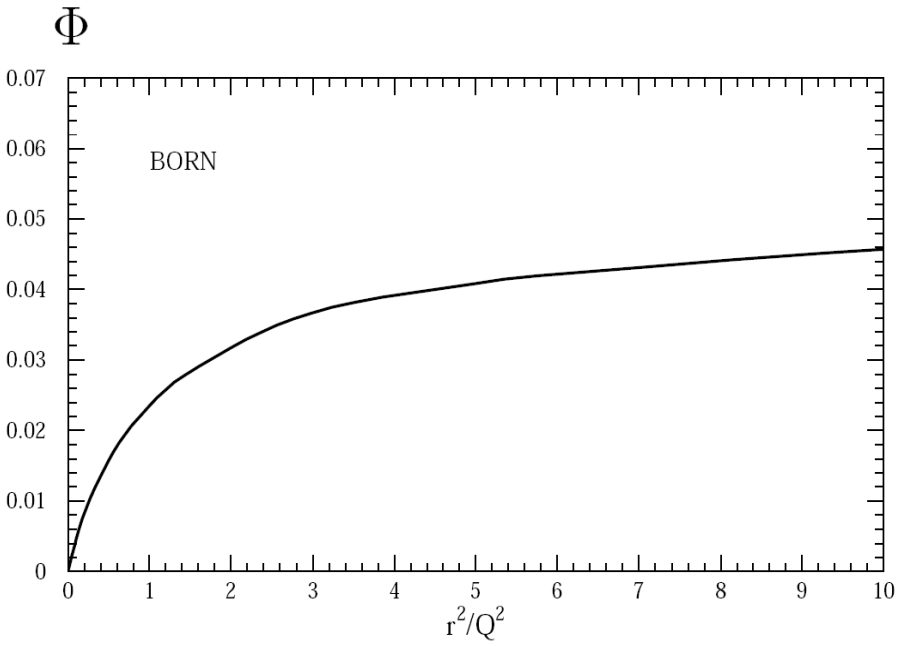

Figure 3.9: Born impact factor. $\alpha_s \approx 0.18$

.

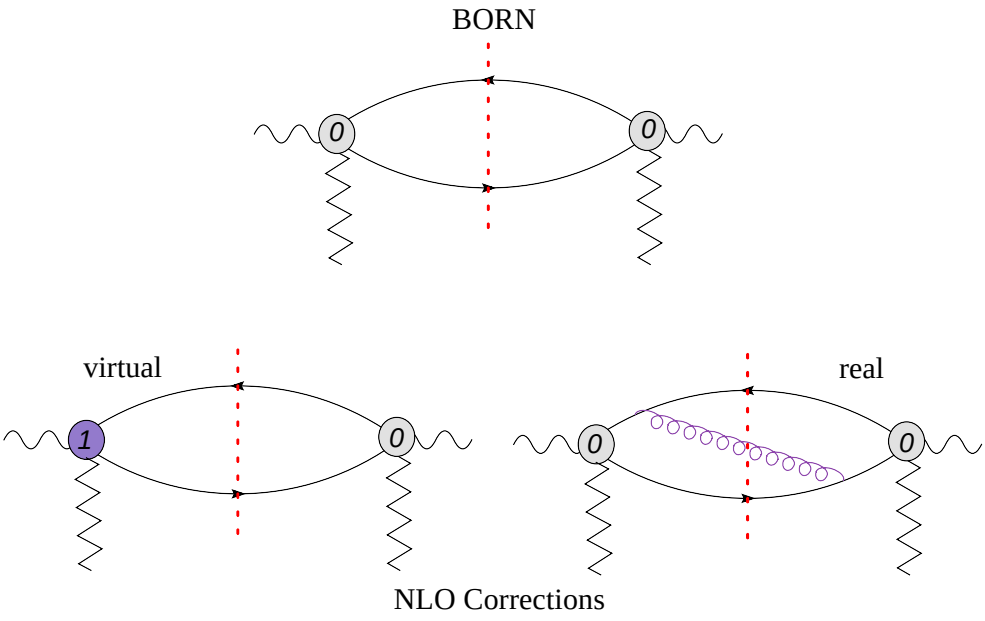

Figure 3.10: Corrections to the impact factor at NLO

.

took place in Ref. [13]. The last step so far, involved analytic manipulation and numerical integration over phase space for the real corrections [16]. The final step, and the one which will be presented in this thesis is the numerical integration over phase space for the virtual corrections which will leave us with a full NLO numerical implementation of the impact factor. We will firstly discuss in brief the known results.

As we previously stated, to 'extract' the corrections one needs to use the processes $\gamma^* q' \to q\bar{q}\, q'$ for the virtual corrections and $\gamma^* q' \to q\bar{q}g\, q'$ for the real ones. The relevant Feynman diagrams for the virtual corrections are shown in Fig. 3.11 and for the real ones in Fig. 3.12. It is evident, that for many of them, we can see similarities with the ones we used in Section 2.3, with a certain additional complication, namely the upper 'part' is not a quark line but a vertex between a photon and a $q\bar{q}$ pair.

The NLO corrections to the virtual photon impact factor have three 'sources'. Two contributions will come from the process with the same intermediate state as in the Born case, $\gamma^* q \to q\bar{q}\, q'$. From Eq. 3.11, we see that corrections can enter in this case either through the vertex $\Gamma^{\alpha}_{\gamma^* \to q\bar{q}}$ ($\Gamma^{(1),\alpha}_{\gamma^* \to q\bar{q}}$), or because of the first term of the expansion of the gluon trajectory, $\omega^{(1)}$ (third term of Eq. 3.11). To these we will refer to as the 'virtual' part of the NLO corrections. The third contribution is extracted from the process which involves the production of a gluon in the intermediate state, namely

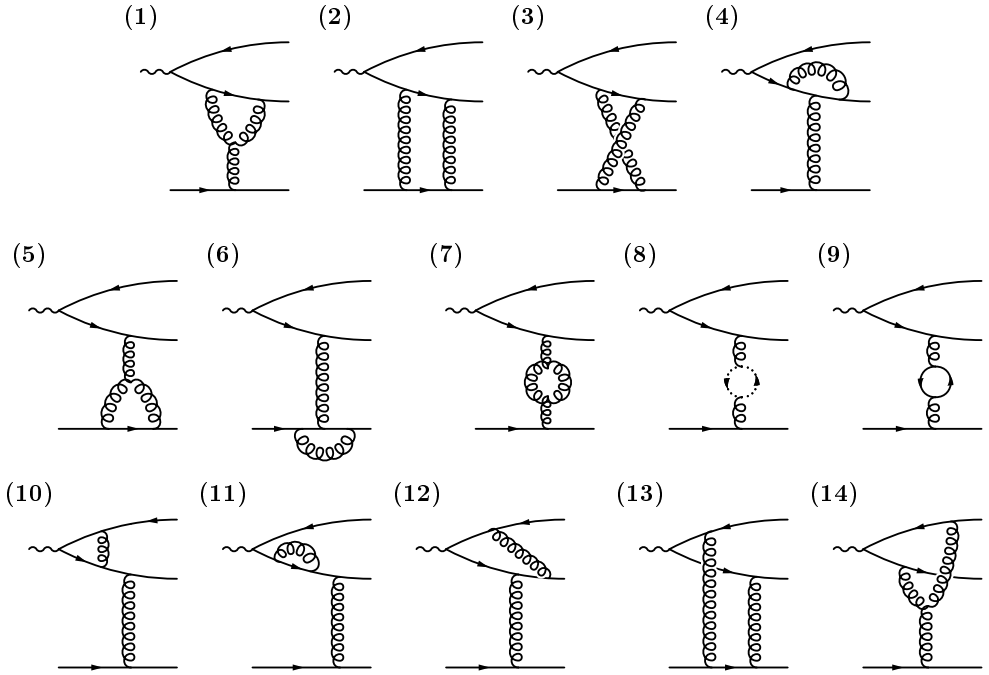

Figure 3.11: Virtual Corrections. One should also include the ones with the quark- antiquark lines interchanged.

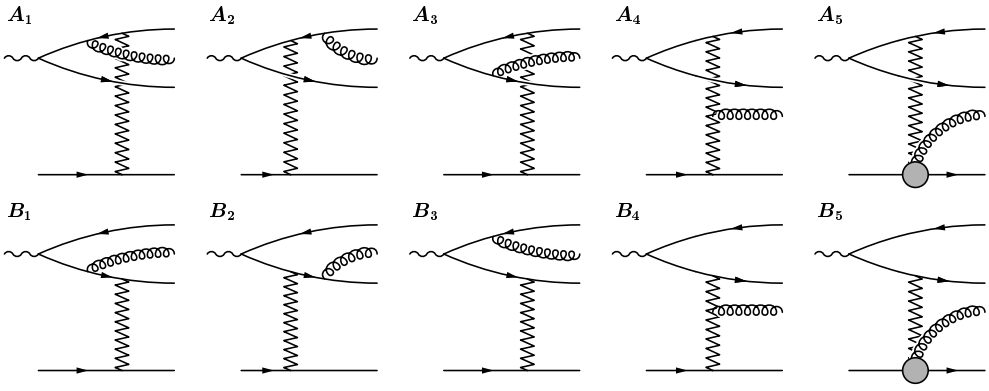

Figure 3.12: Real Corrections.

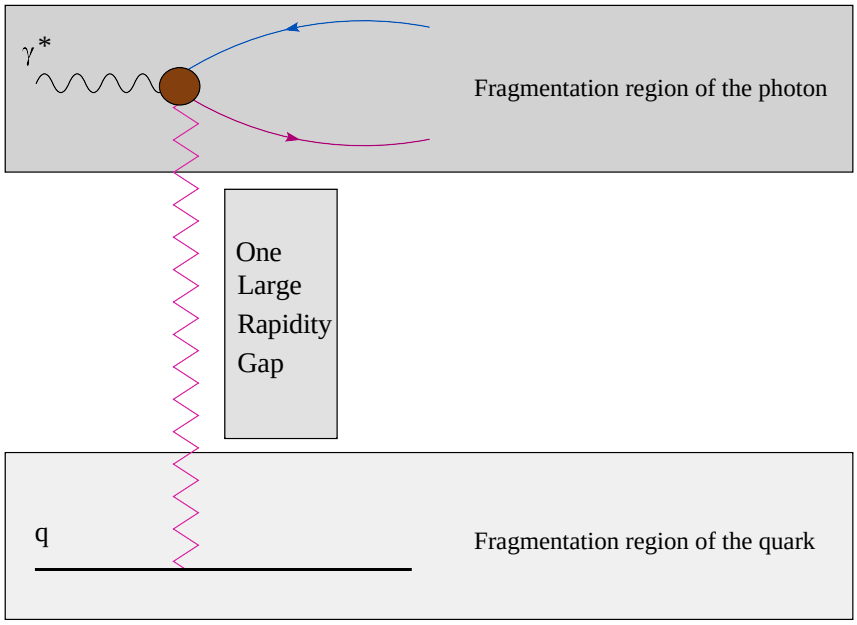

Figure 3.13: Configuration with one large rapidity gap.

$\gamma^* q \to q\bar{q}g\,q'$. These we will call 'real' part. The gluon, depending on its rapidity, can divide the phase space into a configuration with one large rapidity gap, as for example in Fig. 3.13 when it is emitted either in the photon or in the quark fragmentation region, or with two large rapidity gaps when emitted in the central region, as in Fig. 3.14. The only allowed part of the phase space for the real part is the one with one large rapidity gap and the gluon emission taking place within the fragmentation region of the photon. To divide the phase space such that only the relevant 'upper' part will be considered, the introduction of an energy scale s_0 was necessary [14, 15].

This energy scale, s_0, as we will see in the following Sections, is the same as the one used in the BFKL equation, in Chapter 2. It serves as an energy cutoff: gluons with rapidities above s_0 belong in the fragmentation region of the photon, see Fig. 3.15, and thus will be accounted for in the real part of the NLO corrections. On the other hand, in Ref. [15], it was shown that the very same s_0 is the scale that regulates the logarithm in s that accompanies the real emission BFKL kernel. Thus, in the NLO fixed order calculation of the $\gamma^*\gamma^*$ total cross section, s_0 enters through both the impact factor and the LO BFKL kernel. However, at the end, the total cross section, at fixed order, is independent of it. We will see that this fact provides us with candidate test for checking the correctness of the final result for the NLO impact factor.

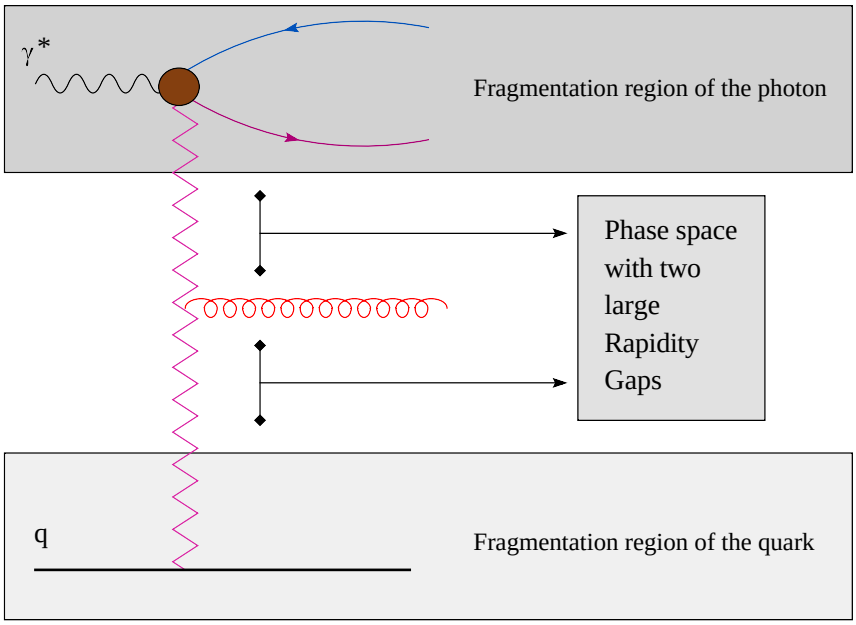

Figure 3.14: Configuration with two large rapidity gaps.

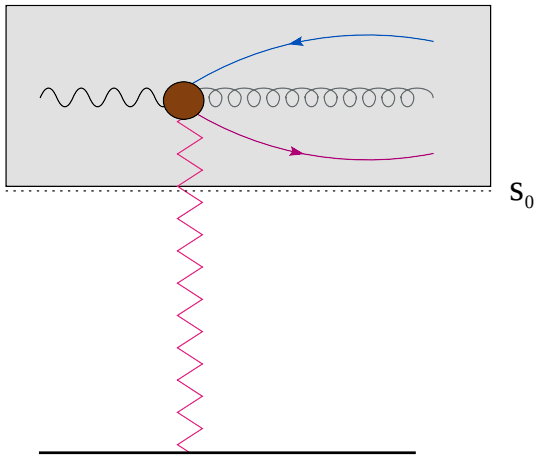

Figure 3.15: The energy scale s_0 sets the lower bound of the photon fragmentation region.

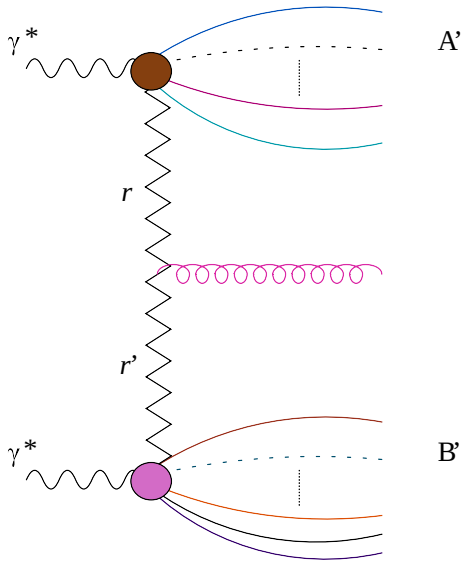

Figure 3.16: $\gamma^*\gamma^*$ scattering. In principal, there may be many more emitted gluons but here we depict only one as this is relevant at NLO order and also to illustrate the notation $\boldsymbol{r}$ and $\boldsymbol{r}'$ of the momenta of the reggeized propagators.

The total cross section for $\gamma^*\gamma^*$ scattering is given by:

$$\begin{aligned}\sigma_{\gamma^*\gamma^*} &= \frac{1}{s}\mathrm{Im}\, T_{\gamma^*\gamma^*}(s, t=0) \\ &= \int \frac{d^{D-2}\mathbf{r}}{(2\pi)^{D-2}} \int \frac{d^{D-2}\mathbf{r}'}{(2\pi)^{D-2}}\, \Phi_A(\mathbf{r}, s_0)\Phi_B(\mathbf{r}', s_0)\frac{f(s, \mathbf{r}, \mathbf{r}', s_0)}{\mathbf{r}^2\mathbf{r}'^2}\,, \end{aligned} \tag{3.29}$$

where $f(s, \mathbf{r}, \mathbf{r}', s_0)$ is the gluon Green's function:

$$f(s, \mathbf{r}, \mathbf{r}', s_0) \;=\; \int \frac{d\omega}{2\pi i}\left(\frac{s}{s_0}\right)^{\omega} f_\omega(\mathbf{r}, \mathbf{r}')\,. \tag{3.30}$$

If we expand $f(s, \mathbf{r}, \mathbf{r}', s_0)$ in $\bar{\alpha}_s = \alpha_s N_c/\pi^2$, we get:

$$f(s, \mathbf{r}, \mathbf{r}', s_0) \;=\; \delta^{(2)}(\mathbf{r} - \mathbf{r}') \;+\; \frac{\bar{\alpha}_s}{2\pi}\,\mathcal{K}_{real}(\mathbf{r}, \mathbf{r}')\,\ln\frac{s}{s_0}\,. \tag{3.31}$$

Recalling that by expanding the photon impact factor in the strong coupling gives

$$\Phi_{\gamma^*} \;=\; g^2\Phi^{(0)}_{\gamma^*} \;+\; g^4\Phi^{(1)}_{\gamma^*}\,, \tag{3.32}$$

we can express the total NLO corrections ($\mathcal{O}(\alpha_s^3)$) to the photonic cross

section as:

$$\begin{aligned}\sigma^{(1)}_{\gamma^*\gamma^*} &= \frac{1}{s}\mathrm{Im}\, T^{(1)}_{\gamma^*\gamma^*}(s,t=0)\\ &= \int \frac{d^{D-2}\boldsymbol{r}}{(2\pi)^{D-2}}\Phi^{(1)}_A(\boldsymbol{r},s_0)\frac{1}{\boldsymbol{r}^4}\Phi^{(0)}_B(\boldsymbol{r}) + \int \frac{d^{D-2}\boldsymbol{r}}{(2\pi)^{D-2}}\Phi^{(0)}_A(\boldsymbol{r})\frac{1}{\boldsymbol{r}^4}\Phi^{(1)}_B(\boldsymbol{r},s_0)\\ &\quad + \int \frac{d^{D-2}\boldsymbol{r}}{(2\pi)^{D-2}}\Phi^{(0)}_A(\boldsymbol{r})\ln(\frac{s}{s_0})2\omega^{(1)}(\boldsymbol{r}^2)\frac{1}{\boldsymbol{r}^4}\Phi^{(0)}_B(\boldsymbol{r})\\ &\quad + \int \frac{d^{D-2}\boldsymbol{r}}{(2\pi)^{D-2}}\frac{d^{D-2}\boldsymbol{r}'}{(2\pi)^{D-2}}\Phi^{(0)}_A(\boldsymbol{r})\frac{1}{\boldsymbol{r}^4}\mathcal{K}_{real}(\boldsymbol{r},\boldsymbol{r}')\frac{1}{\boldsymbol{r}'^4}\Phi^{(0)}_B(\boldsymbol{r}')\ln(\frac{s}{s_0})\,.\end{aligned} \tag{3.33}$$

One would naively expect the logarithm in the third line of Eq. 3.33, to be $\ln(s/\boldsymbol{r}^2)$, in accordance with the Regge ansatz and Eq. 3.11. Nevertheless, this is not the case as in Eq. 3.33 there are contributions from two processes, namely from $\gamma^*q \to q\bar{q}\,q$ and $\gamma^*q \to q\bar{q}g\,q$ scattering, whereas Eq. 3.11 refers only to the former. In other words, in the equation above, we do have a real gluon emission which brings corrections to the total cross section and needs to be taken into account.

The final expression of the impact factor at NLO is the assembly of all the finite pieces. After renormalisation, the ultraviolet divergencies which actually come only from the virtual part, are cancelled. The infrared divergencies of the virtual part cancel against the ones from the real contributions. To isolate the soft and collinear divergencies of the latter, one needs to introduce a scale Λ, which will finally drop out in the final result, but is apparent in the intermediate stages [15]. Thus, the expression for the full NLO corrections will involve, apart from $t = -\boldsymbol{r}^2$, t_α, t_b, M^2, also s_0, Λ, Q^2 and s. Especially for s, it appears explicitely in the finite expressions, before phase space integration, but evidently any dependence on it finally cancels out.

The s_0-dependence of the NLO impact factor as we saw, has it's origin at the calculation of the real corrections. One expects, therefore, to have a clear separation, i.e. the real part carries the s_0 dependence while the virtual part is s_0-independent. However, it is necessary in order to serve an important calculational purpose, to reshuffle the contributing to the corrections terms, such that at the end we will have two pieces, both of which will exhibit the scaling property. Both pieces must be a function of ratios of scales as in the the LO impact factor case. This is very important because it makes possible various checks of the correctness of the phase space integration. By doing so though, we pay the price of distributing the s_0 dependence in both the virtual and real part, but this is not to disturb us at all[2]. To conclude with

[2]Actually, such a clear scheme where s_0 'sits' only in the real corrections is not even

we present below the full NLO contributions:

$$\begin{aligned}\Phi^{(1)}_{\gamma^*} = \Phi^{(1,virtual)}_{\gamma^*}\Big|^{finite} &- \frac{2\Phi^{(0)}_{\gamma^*}}{(4\pi)^2}\left\{\beta_0 \ln\frac{\boldsymbol{r}^2}{\mu^2} + C_F \ln(\boldsymbol{r}^2)\right\} \\ &+ \int_0^1 d\alpha \int \frac{d\boldsymbol{k}}{(4\pi)^2}\,\mathcal{I}_2(\alpha,\boldsymbol{k})\left\{C_A\left[\ln^2\alpha(1-\alpha)s_0 - \ln^2 M^2\right]\right. \\ &+ C_A\left[-2\ln(\boldsymbol{r}^2)\,\ln(\frac{s_0}{\boldsymbol{r}^2})\right] \\ &\qquad\left. + 2C_F\left[8 - 3\ln\alpha(1-\alpha)\Lambda^2 + \ln^2 M^2 + \ln^2\frac{\alpha}{1-\alpha}\right]\right\} \\ &+ C_A\,\Phi^{(1,real)}_{\gamma^*}\Big|^{finite}_{C_A} + C_F\,\Phi^{(1,real)}_{\gamma^*}\Big|^{finite}_{C_F}\,. \end{aligned} \tag{3.34}$$

Presenting in this way the finite contributions from the diagrams to the NLO impact factor has certain advantages. Most importantly, the first four lines in Eq. 3.34 are scale independent (apart from the β_0 dependent term obviously, which controls the running of the coupling constant α_s). To make it even clearer, by scale independence we mean that the terms in the first four lines (from now on, these will be referred to as virtual contributions despite the fact that some terms have their origin at the diagrams of Fig. 3.12) are in total a function of the ratios $\frac{s_0}{Q^2}$, $\frac{\Lambda^2}{Q^2}$ and $\frac{\boldsymbol{r}^2}{Q^2}$. The same holds for the last line separately, which we will call real contributions hereafter. They were integrated over phase space in Ref. [16]. The missing ingredient so far was the very first term in Eq. 3.34, namely $\Phi^{(1,virtual)}_{\gamma^*}\big|^{finite}$. The computation of this term will be presented in the next Section. The scale independence property will enable us to test its calculation. Another way one can interpret the scaling property is by stating that the only dependence that the impact factor carries upon the renormalisation scale μ lies onto the $\beta_0 \ln\frac{\boldsymbol{r}^2}{\mu^2}$ term, as it was demonstrated in Ref. [15]. Before we proceed to the next Section, where we will present the results for $\Phi^{(1,virtual)}_{\gamma^*}\big|^{finite}$, some remarks on what we should choose as the value of s_0 are in order. One can argue that we can chose an arbitrary fixed value, e.g. $s_0 = 10$ GeV^2 or $s_0 = 50$ GeV^2, but another choice is probably more fortunate. We remind that for the BFKL kernel, the usual choice is the symmetric

$$s_0 = \boldsymbol{r}\boldsymbol{r}'\,. \tag{3.35}$$

However, as we pointed out earlier, the scale s_0 has to have the same value for the NLO impact factor and the BFKL kernel and a choice as in Eq. 3.35 seems forbidden. It would mean that the upper impact factor would 'know'

accurate. One can see in Ref. [15] that, for the cancellation of the infrared divergencies of the vertex $\Gamma^{(1)}_{\gamma^*\to q\bar{q}}$, one needs a piece from the gluon trajectory (Eq. 33 and 34 in Ref. [15]), which brings an s_0 dependence into the virtual part.

about the lower one which does not make sense. We will show immediately though that things are not as they seem. Combining once more the equations 3.29, 3.30, 3.31 but also using 3.35 we get:

$$\begin{aligned}
\sigma^{(1)}_{\gamma^*\gamma^*} &= \frac{1}{s}\mathrm{Im}\, T^{(1)}_{\gamma^*\gamma^*}(s,t=0) \\
&= \int \frac{d^{D-2}\boldsymbol{r}}{(2\pi)^{D-2}} \int \frac{d^{D-2}\boldsymbol{r}'}{(2\pi)^{D-2}} \Phi^{(1)}_A(\boldsymbol{r}, s_0 = \boldsymbol{r}\boldsymbol{r}') \frac{1}{\boldsymbol{r}^2}\frac{1}{\boldsymbol{r}'^2} \Phi^{(0)}_B(\boldsymbol{r}')\delta^{(2)}(\boldsymbol{r}-\boldsymbol{r}') \\
&+ \int \frac{d^{D-2}\boldsymbol{r}}{(2\pi)^{D-2}} \int \frac{d^{D-2}\boldsymbol{r}'}{(2\pi)^{D-2}} \Phi^{(0)}_A(\boldsymbol{r}) \frac{1}{\boldsymbol{r}^2}\frac{1}{\boldsymbol{r}'^2} \Phi^{(1)}_B(\boldsymbol{r}', s_0 = \boldsymbol{r}\boldsymbol{r}')\delta^{(2)}(\boldsymbol{r}-\boldsymbol{r}') \\
&+ \int \frac{d^{D-2}\boldsymbol{r}}{(2\pi)^{D-2}} \int \frac{d^{D-2}\boldsymbol{r}'}{(2\pi)^{D-2}} \Phi^{(0)}_A(\boldsymbol{r}) \ln(\frac{s}{s_0 = \boldsymbol{r}\boldsymbol{r}'}) 2\omega^{(1)}(\boldsymbol{r}^2) \frac{1}{\boldsymbol{r}^2}\frac{1}{\boldsymbol{r}'^2} \Phi^{(0)}_B(\boldsymbol{r}')\delta^{(2)}(\boldsymbol{r}-\boldsymbol{r}') \\
&+ \int \frac{d^{D-2}\boldsymbol{r}}{(2\pi)^{D-2}} \frac{d^{D-2}\boldsymbol{r}'}{(2\pi)^{D-2}} \Phi^{(0)}_A(\boldsymbol{r}) \frac{1}{\boldsymbol{r}^4} \mathcal{K}_{real}(\boldsymbol{r},\boldsymbol{r}') \frac{1}{\boldsymbol{r}'^4} \Phi^{(0)}_B(\boldsymbol{r}') \ln(\frac{s}{s_0}) \,, \qquad (3.36)
\end{aligned}$$

from which, after performing the integration over $\boldsymbol{r}'$ with the help of the δ functions, we finally obtain:

$$\begin{aligned}
\sigma^{(1)}_{\gamma^*\gamma^*} &= \frac{1}{s}\mathrm{Im}\, T^{(1)}_{\gamma^*\gamma^*}(s,t=0) \\
&= \int \frac{d^{D-2}\boldsymbol{r}}{(2\pi)^{D-2}} \Phi^{(1)}_A(\boldsymbol{r}, s_0 = \boldsymbol{r}^2) \frac{1}{\boldsymbol{r}^4} \Phi^{(0)}_B(\boldsymbol{r}) + \int \frac{d^{D-2}\boldsymbol{r}}{(2\pi)^{D-2}} \Phi^{(0)}_A(\boldsymbol{r}) \frac{1}{\boldsymbol{r}^4} \Phi^{(1)}_B(\boldsymbol{r}, s_0 = \boldsymbol{r}^2) \\
&+ \int \frac{d^{D-2}\boldsymbol{r}}{(2\pi)^{D-2}} \Phi^{(0)}_A(\boldsymbol{r}) \ln(\frac{s}{\boldsymbol{r}^2}) 2\omega^{(1)}(\boldsymbol{r}^2) \frac{1}{\boldsymbol{r}^4} \Phi^{(0)}_B(\boldsymbol{r}) \\
&+ \int \frac{d^{D-2}\boldsymbol{r}}{(2\pi)^{D-2}} \frac{d^{D-2}\boldsymbol{r}'}{(2\pi)^{D-2}} \Phi^{(0)}_A(\boldsymbol{r}) \frac{1}{\boldsymbol{r}^4} \mathcal{K}_{real}(\boldsymbol{r},\boldsymbol{r}') \frac{1}{\boldsymbol{r}'^4} \Phi^{(0)}_B(\boldsymbol{r}') \ln(\frac{s}{s_0}) \,. \qquad (3.37)
\end{aligned}$$

Therefore, apart from a fixed value for s_0, we can also use the choice $s_0 = \boldsymbol{r}^2$ for the impact factor while we use for the BFKL kernel $s_0 = \boldsymbol{r}\boldsymbol{r}'$. Actually, Eq. 3.37 is what we, as before noted, would expect due the Regge ansatz. Moreover, with this choice of s_0, the third line in Eq. 3.34 vanishes and we recover Eq. 169 in Ref. [15]. Nevertheless, what is the best scale choice cannot be decided upon, without further investigation after contracting the NLO photon impact factor with the NLO gluon Green's function.

3.3 $\Phi^{(1,\mathrm{v}virtual)}_{\gamma^*}$, computational details

To compute $\Phi^{(1,virtual)}_{\gamma^*}$ we need the Born vertex $\Gamma^{(0)}_{\gamma^*\to q\bar{q}}$ from Eq. (3.16) and the NLO one $\Gamma^{(1)}_{\gamma^*\to q\bar{q}}$ which was calculated in [13]. Then it will be[3]:

$$\Phi^{(1,virtual)}_{\gamma^*} = \int \frac{d^{D-2}\boldsymbol{k}}{(2\pi)^{D-1}} \frac{d\alpha}{2\alpha(1-\alpha)} \left[\Gamma^{(1)}_{\gamma^*\to q\bar{q}} \otimes \Gamma^{(0)*}_{\gamma^*\to q\bar{q}} + c.c\right] , \qquad (3.38)$$

[3]In this Section we will skip the superscript 'virtual', since it is clear that we are referring to the virtual corrections.

where the contraction $\otimes$ implies also summation over helicities as a trace. The amplitude for the $\Gamma^{(1)}_{\gamma^*\to q\bar{q}}$, namely $T^{(1)}$, was presented in Ref. [13] as a sum of terms that are generated from each diagram in Fig. 3.11, plus the diagrams that are obtained after interchanging the couplings of t-channel gluons between quarks and antiquarks:

$$T^{(1)} = \sum_{i=1}^{13} \left(A_i \, + \, \bar{A}_i\right) + A_{14}\,. \tag{3.39}$$

A_{14} is symmetric with respect to interchanging quark-antiquark lines. in Ref. [13], every term in Eq. 3.39 has been cast into the following form:

$$A_{\#diagram} \, = \, \frac{1}{\epsilon^2} A^{(-2)}_{\#diagram} \, + \, \frac{1}{\epsilon} A^{(-1)}_{\#diagram} \, + \, A^{(0)}_{\#diagram}\,, \tag{3.40}$$

where the subscript $\#diagram$ runs from one to fourteen. After expanding in ϵ for each $A_{\#diagram}$ and the cancellation of the UV and IF divergences, we are left with the corresponding for each diagram finite piece. The sum of all these finite pieces is exactly the $T^{(1)}_{finite}$, that we need to contract with the Born in order to get $\Phi^{(1,virtual)}_{\gamma^*}$. We will not present the whole result here as it is very lengthy. Instead, we will present only the finite contribution of diagram 4 in Fig. 3.11 in order to discuss some important points of the calculation.

$$\begin{aligned}
A_4^{(finite)} = \frac{1}{(4\pi)^2}\Big(&\frac{-(H_T^\alpha \, \log(-t))}{2\,N_c\,s\,t_\alpha} + \frac{-2\,\alpha\,H_\varepsilon^\alpha\,s\,t_\alpha\,\log(-t) + H_T^\alpha\,t\log(-t)^2}{2\,N_c\,s\,(t-t_\alpha)\,t_\alpha} \\
&+ \frac{4\,H_T^\alpha\,t^2 - 8\,H_T^\alpha\,t\,t_\alpha + 5\,\alpha\,H_\varepsilon^\alpha\,s\,t\,t_\alpha + 4\,H_T^\alpha\,{t_\alpha}^2}{2\,N_c\,s\,(t-t_\alpha)^2\,t_\alpha} \\
&- \frac{5\,\alpha\,H_\varepsilon^\alpha\,s\,{t_\alpha}^2 + \alpha\,H_\varepsilon^\alpha\,s\,t\,t_\alpha\log(-t)^2}{2\,N_c\,s\,(t-t_\alpha)^2\,t_\alpha} \\
&+ \frac{(-(\alpha\,H_\varepsilon^\alpha\,s\,t_\alpha\,(3\,t+2\,t_\alpha)) + H_T^\alpha\,(-2\,t^2 + t\,t_\alpha + {t_\alpha}^2))\,\log(\frac{t}{t_\alpha})}{2\,N_c\,s\,(t-t_\alpha)^2\,t_\alpha} \\
&- \frac{H_T^\alpha\,t^2\log(-t_\alpha)^2 + H_T^\alpha\,t\,t_\alpha\log(-t_\alpha)^2 - \alpha\,H_\varepsilon^\alpha\,s\,t\,t_\alpha\log(-t_\alpha)^2}{2\,N_c\,s\,(t-t_\alpha)^2\,t_\alpha}\Big)\,.
\end{aligned} \tag{3.41}$$

Firstly, we need to say that for the NLO vertex, the helicity matrix elements are five and not two as for the Born case, namely H_T^α, $\bar{H}_T^\alpha$, H_ε^α, H_p^α and H_k^α. The definitions for H_T^α, $\bar{H}_T^\alpha$ are as in the Born case, whereas it is [13]:

$$H_\varepsilon^\alpha \, = \, \bar{u}(k+r,\lambda) \, \not{\varepsilon}\lambda^\alpha \, v(q-k,\lambda'), \tag{3.42}$$

$$H_k^\alpha \, = \, \bar{u}(k+r,\lambda) \, \not{k}\lambda^\alpha \, v(q-k,\lambda'), \tag{3.43}$$

$$H_p^\alpha \,=\, \bar{u}(k+r,\lambda)\; \not{p}\lambda^\alpha\, v(q-k,\lambda'). \tag{3.44}$$

Only four of them are independent because of the relation:

$$H_T^\alpha \,+\, \bar{H}_T^\alpha \,=\, sH_\varepsilon^\alpha \,-\, 2\varepsilon\cdot pH_k^\alpha \,-\, 2\varepsilon\cdot rH_p^\alpha. \tag{3.45}$$

We have chosen to use Eq. 3.45 for substituting the value of H_ϵ^α in all of our expressions. The summation over helicities as a trace, for the case of longitudinal polarisation that is of our concern, is done with the help of the following relations:

$$trH_T \otimes \frac{H_T^*}{st_a} \,=\, -\frac{2\alpha s}{Q^2 D(\boldsymbol{k})}\left[\boldsymbol{k}^2-\alpha(1-\alpha)Q^2\right]^2, \tag{3.46}$$

$$tr\bar{H}_T \otimes \frac{H_T^*}{st_a} \,=\, -\frac{2(1-\alpha)s}{Q^2 D(\boldsymbol{k})}\left[\boldsymbol{k}^2-\alpha(1-\alpha)Q^2\right]\,\left[(\boldsymbol{k}+\boldsymbol{r})^2-\alpha(1-\alpha)Q^2\right], \tag{3.47}$$

$$trH_p \otimes \frac{H_T^*}{st_a} \,=\, \frac{2\alpha(1-\alpha)s}{QD(\boldsymbol{k})}\left[\boldsymbol{k}^2-\alpha(1-\alpha)Q^2\right], \tag{3.48}$$

$$trH_k \otimes \frac{H_T^*}{st_a} \,=\, -\frac{2}{QD(\boldsymbol{k})}\left[\boldsymbol{k}^2-\alpha(1-\alpha)Q^2\right]\,\left[\boldsymbol{k}\cdot(\boldsymbol{k}+\boldsymbol{r})-\alpha(1-\alpha)Q^2\right], \tag{3.49}$$

$$trH_e \otimes \frac{H_T^*}{st_a} \,=\, -\frac{2}{Q^2 D(\boldsymbol{k})}\left[\boldsymbol{k}^2-\alpha(1-\alpha)Q^2\right]\,\left[\boldsymbol{k}\cdot(\boldsymbol{k}+\boldsymbol{r})-\alpha(1-\alpha)Q^2\right]. \tag{3.50}$$

A next observation that we can draw from Eq. 3.41 is that we have logarithms with dimenionsful arguments. Normally, one would expect ratios of two dimensionful scales in the arguments of any function that appears in the finite expressions for any diagram. Nevertheless, this needs not to worry us at this point, because of what we stated in the previous Section, namely the part of Eq. 3.34 that we named virtual corrections has the scaling property. This was extensively and thoroughly checked. In other words, one can imagine that every dimensionful argument of a logarithm is scaled by the renormalisation scale μ, however, the combination of all the logarithms from all the finite pieces of the virtual corrections cancels this μ dependence, with the exception of course being the term that regulates the running of the strong coupling constant. In our finite expressions for the virtual corrections, we have also the presence of dilogarithms but in this case the arguments are dimensionless.

Finally, the last remark we will make on Eq. 3.41 has to do with the appearance of the 'poles' $1/(t-t_\alpha)$. In the complete set of our expressions, we encounter the following spurious poles: $1/(t-t_\alpha)$, $1/(t-t_\beta)$, $1/(Q^2+t_\alpha)$, $1/(Q^2+t_\beta)$ and $1/(Q^2\,t+t_\alpha t_\beta)$. They were introduced (as Gram determinants) during the tensor decomposition of the loop integrals in the calculation of the amplitudes for the diagrams in Fig. 3.11. Before proceeding in the numerical evaluation, we made lengthy and extensive tests to verify

that these singularities are indeed spurious. By expanding in Taylor series the contributions from every diagram, we have seen that indeed they cancel for each diagram individually as one would expect. This was needed for one more reason. The spurious poles are prone to introducing numerical instabilities near the singular points of the phase space. One can then overcome this, by using the Taylor expansion of the amplitude in the close vicinity of the singular point instead of the full expression itself. However, we did not need to use this option as the convergence was very good anyway. It might be of use though, if one wants to push the accuracy well down to less than one percent, which for the present needs is not required.

To perform the phase space integration, we have written a code in MATHEMATICA which reads in the vertices, NLO and Born, makes the contraction between the helicity matrix elements and finally calculates the integrand which serves as the input for VEGAS, the integration routine we used. The integrand is far too long (several tens of thousand of lines in FORTRAN) to be presented in a printed form. We had tested the integration procedure by feeding in our MATHEMATICA routine and subsequently integrating with VEGAS, not the only the whole $\Gamma^{(1)}_{\gamma^*\to q\bar{q}}$ vertex which is the sum from the 14 different diagrams in Fig. 3.11, but also sole pieces from individual diagrams. The convergence was extremely good in most of the cases and we were able to achieve an accuracy better than one percent.

As we have already mentioned, we have used various checks for the consistency and the correctness of the numerical integration, from trivial ones up to quite involved. We will list here the most important of them. The units of the scales are in GeV^2 and of course the impact factor is dimensionless. The numerical values below, are the output of the integration of the first four lines of Eq. 3.34 and not of the $\Phi^{(1,virtual)}_{\gamma^*}$ alone. It is the numerical output of what we will refer to as the virtual corrections and will denote by $\Phi^{(1),virt}$.

- **s-independence**
  We have stated that all the energy dependence of the total cross section is carried by the BFKL Green's function. The impact factor should carry no s dependence. However, as one can see in Eq. 3.41, s appears explicitely in the expressions of the amplitudes. We have, therefore, checked whether s drops out finally. That is exactly what we have numerically verified, as can be clearly seen from the table below.

s	$\Phi^{(1),virt}$
10^5	0.01413
10^6	0.01415
10^7	0.01415
10^8	0.01414

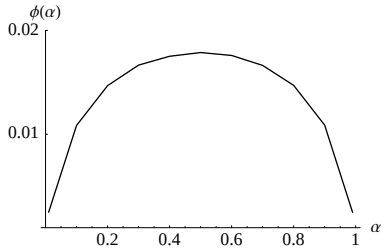

Figure 3.17: $\alpha \leftrightarrow 1-\alpha$ symmetry. $\phi(\alpha)$ is the α-unintegrated impact factor.

- $\alpha \leftrightarrow 1-\alpha$ **symmetry**
  This is a symmetry that has to hold after integrating over $\boldsymbol{k}$ but without performing the over α integration, in accordance with the LO case, Eq. 3.28. We remind here that α and $1-\alpha$ are the fractions of the longitudinal momentum of the photon that are carried by the quark and antiquark pair. The NLO corrections must and finally do follow the same pattern as we can see from the table below. We have run our code for $\boldsymbol{r}^2 = 75$, $Q^2 = 15$, $\Lambda = 15$ and $s_0 = 15$. In the right hand side column stand the values of the 'α-unintegrated impact factor' while in the left column are presented the corresponding values of α. We plot the table in Fig. 3.17 to show the symmetry in a pictorial way.

α	$\phi(\alpha)$
0.01	0.00249
0.1	0.01085
0.2	0.01468
0.3	0.01666
0.4	0.01751
0.5	0.01787
0.6	0.01759
0.7	0.01663
0.8	0.01471
0.9	0.01088
0.99	0.00248

- $\Phi^{(1)}_{\gamma^*}|_{\boldsymbol{r}\to 0} \sim \boldsymbol{r}^2$
  The NLO impact factor should also follow the behaviour of the Born

one at the $\boldsymbol{r} \to 0$ limit. It is implied, that it should vary like $\boldsymbol{r}^2$ or $\boldsymbol{r}^2 \ln \boldsymbol{r}^2$ at that limit. We can safely state for the virtual part of the corrections that it dies for very small $\boldsymbol{r}$, although we cannot say what exactly is its functional form (whether it involves logarithms). To answer that we would need to push the numerical accuracy to the extreme.

- **Scale invariance**
  We present here a demonstration of the scaling property that we described in details previously. We keep fixed the ratios $\frac{s_0}{Q^2}$, $\frac{\Lambda^2}{Q^2}$ and $\frac{\boldsymbol{r}^2}{Q^2}$, while we vary the actual values of each quantity. We note once more, that we integrate the first four lines of Eq. 3.34, which is actually why we need to specify values for Λ and s_0.

$\boldsymbol{r}^2$	Q^2	s_0	Λ	$\frac{\boldsymbol{r}^2}{Q^2}$	$\Phi_{\gamma^*}^{(1),virt}$
0.1	0.01	0.01	0.01	10	0.01860
1	0.1	0.1	0.1	10	0.01863
10	1	1	1	10	0.01865
20	2	2	2	10	0.01864
30	3	3	3	10	0.01864
50	5	5	5	10	0.01867

  The above table is also a clear justification of why we were permitted to use dimensionful arguments in the logarithms that appear in the expressions that contribute to the $\Gamma^{(1)}_{\gamma^* \to q\bar{q}}$.

- **s_0-independence of the NLO fixed order $\sigma_{tot}^{\gamma^*\gamma^*}$**
  As was previously stated, s_0 is a scale on which physical observables cannot have any dependence. The dependence that the BFKL kernel introduces into the calculation of a a total cross section cancels against the one that is entering via the NLO photon impact factor. Thus, we numerically check whether the pieces that carry explicitely or implicitly an s_0 in Eq. 3.34 are, at the end of the day, independent of it. That is indeed the case as we can see in Fig. 3.18. For this run of the code we used $\boldsymbol{r}^2/Q^2 = 5$. The curve shows that the result is s_0 independent (within deviations of the order of one standard deviation of the numerical integration).

3.4 Plots for the full NLO impact factor

It is now time to present plots for the full NLO virtual photon impact factor. Since the impact factor is an object that depends on the s_0 scale, we will present plots for two different values of s_0. For each value of s_0 we will show

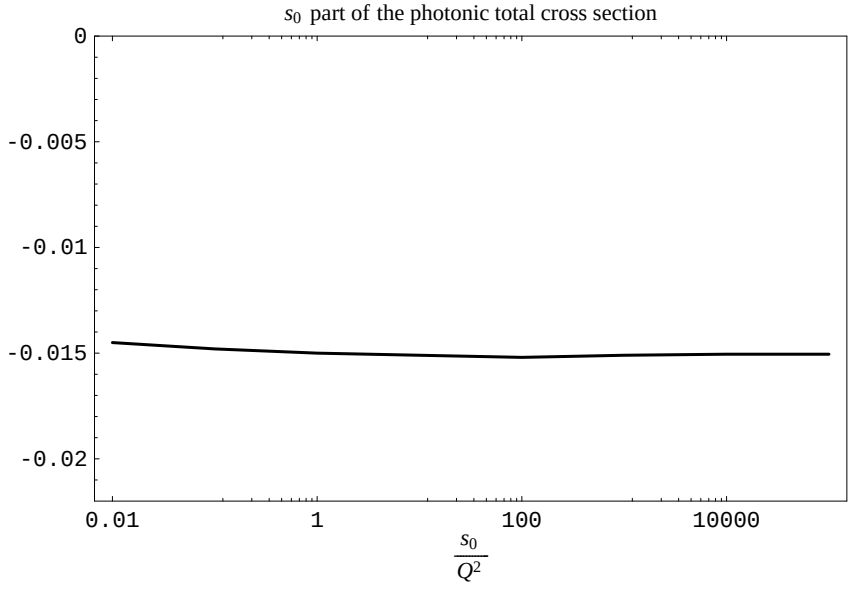

Figure 3.18: The part of the total $\gamma^*\gamma^*$ cross section that depends on s_0, plotted as a function of s_0/Q^2.

two figures, one with the virtual contributions (first four lines of (3.34)), the real contributions (last line of (3.34)) and the total NLO corrections plotted together, and one with the full NLO impact factor. We have chosen to use $Q^2 = 15$ as the scale that sets the running of the coupling α_s. The values for s_0 are:

- $s_0 = \boldsymbol{r}^2$, Fig. 3.19 and Fig. 3.20.
- $s_0 = 10$, Fig. 3.21 and Fig. 3.22.

As we can see, the real corrections are very large and negative. This is because, what we name at this point real corrections (last line of 3.34) do not correspond to the whole phase space. We remind that the central region is subtracted. On the other hand, the virtual part is also large and with positive sign. The combination of the two, which gives the total NLO corrections, is finally negative and large. Depending on the value of $\boldsymbol{r}^2/Q^2$ and s_0, the corrections are larger than half the value of the Born or even larger than the Born contribution itself, Fig 3.22. Actually, the shape of the full NLO impact factor depends critically on the choice of s_0. If we select a fixed value for s_0 then the smaller this value is, the larger the corrections are, such that they drive the full impact factor to negative values, Fig. 3.22. A large fixed s_0 on the other hand has exactly the opposite effect. Lastly,

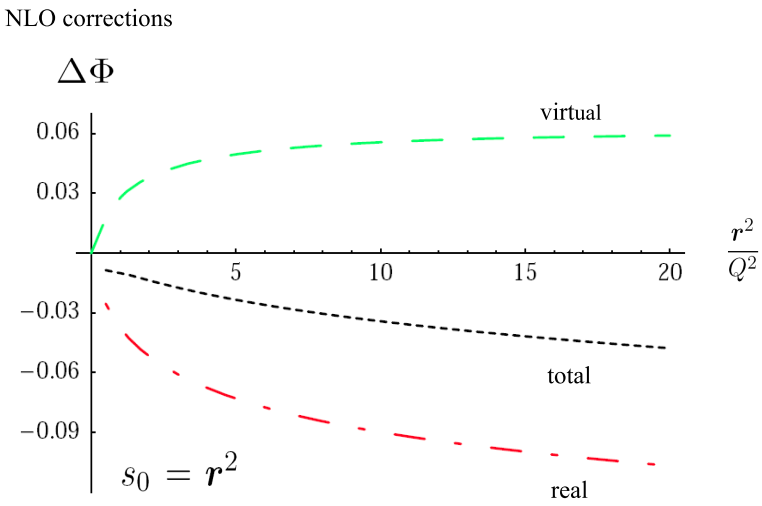

Figure 3.19: Virtual, real and total NLO corrections to the photon impact factor for $s_0 = \boldsymbol{r}^2$.

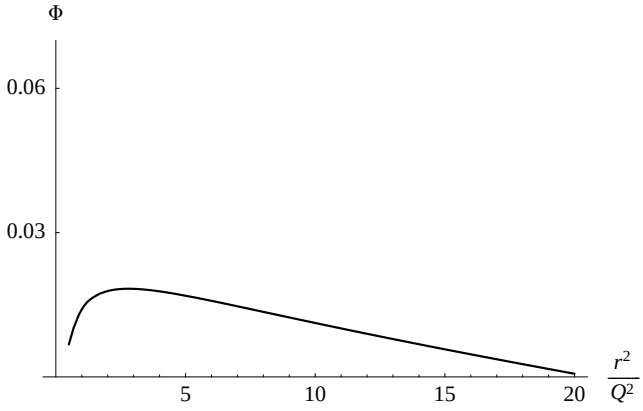

Figure 3.20: The full NLO impact factor for $s_0 = \boldsymbol{r}^2$.

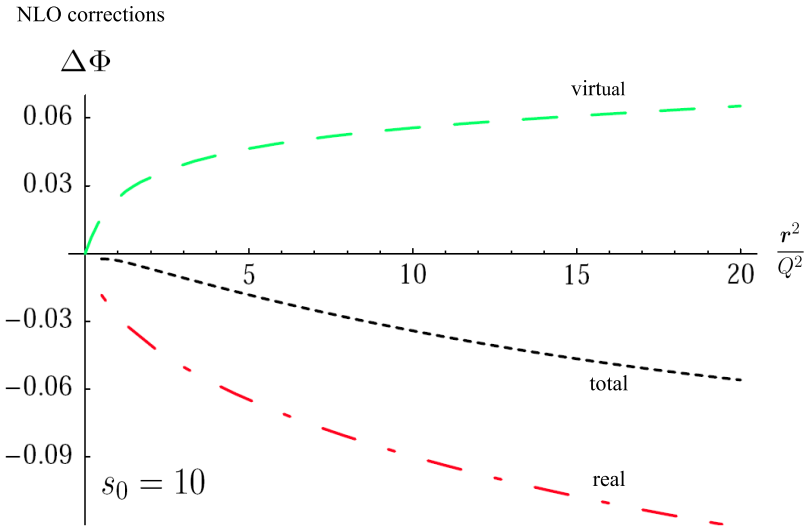

Figure 3.21: Virtual, real and total NLO corrections to the photon impact factor for $s_0 = 10$.

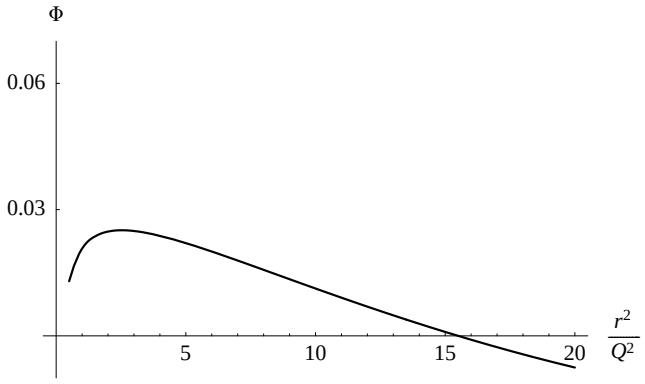

Figure 3.22: The full NLO impact factor for $s_0 = 10$.

from Fig. 3.19 we deduce that a choice of $s_0 = \boldsymbol{r}^2$ produces a more regular behaviour for the full NLO result. Nevertheless, we state once more that this discussion cannot be final before convoluting the NLO impact factor with the NLO gluon Green's function and make an extensive study.

3.5 Conclusions and Outlook

We have finally presented results for the full NLO virtual photon impact factor. The last missing ingredient for the numerical implementation was the integration over phase space for the virtual contributions. In our classification according to Eq. 3.34, the virtual contributions are large and positive, while the real contributions are also large and negative. The total corrections together are sizeable and negative. Nevertheless there are parameters that can change this overall picture. One of course is the value for s_0 which plays quite an important role for the shape of the corrections. Another, is the choice of the scale that regulates the running of a_s. A recent NLO analysis for the electroproduction of two light vector mesons [31] deals exactly with points like that. The above do not change the fact though, that we finally have the numerical integration of the analytic expressions for the NLO photon impact factor. The next step, during which the issues that we touched above will be totally cleared out, is when we will convolute the NLO gluon Green's function [32] with the NLO impact factor to produce total cross section and to which we are looking forward to.

Chapter 4

Non Linear Evolution in High Energy QCD

One of the most tantalising problems of Quantum Chromodynamics is the prediction of growth of the total cross sections at high energies, which emerges as a natural conclusion when one uses BFKL dynamics. In the following, we will review the BFKL equation, which in the first half of this thesis described the amplitude for the interaction between the reggeized gluons in the t channel, in a different setup, namely in the dipole picture. The BFKL equation, being a linear evolution equation, accounts only for gluon emissions, in describing the evolution in rapidity for the gluon density. The growth of the gluon density, as predicted from the BFKL equation, gives a strong power-like growth of the gluon density, which results in a similar behaviour of the cross section

$$f(x) \sim x^{-\lambda}, \tag{4.1}$$

where x is the Bjorken scaling variable and $\lambda = \frac{4 \ln 2 N_c}{\pi} \alpha_s$ is the Pomeron intercept in leading logarithmic approximation. This fact leads to the violation of the Froissart-Martin bound, which stems from the general assumptions of the analyticity and unitarity of the S-matrix, and states that the hadronic cross sections can have at high energies at most a logarithmic behaviour in s. For a DIS process it will be $\sigma_{tot} < R^2$ with $R \sim \ln s$. Power like behaviour of the cross sections is thus in direct contradiction with the s channel unitarity and a unitarization of the Pomeron amplitude is needed. In the early 80's, Gribov, Levin and Ryskin [17] and a bit later Mueller and Qiu [33] pointed out that a possible cure for the restoration of the unitarity was gluon fusion which at high energies should not be neglected. The main idea was that if gluon splitting leads to a very high gluon density, or in other words to a very dense medium, then this cannot go on without reaching a point at which the density saturates and gluon recombination effects are into

the game. That is exactly the notion behind *perturbative parton saturation*[1]. In Ref. [17], a new non-linear evolution equation was suggested to describe the phenomenon of saturation:

$$Q^2 \frac{\partial^2 xG(x,Q^2)}{\partial \ln 1/x \partial Q^2} = \frac{\alpha_s N_c}{\pi} xG(x,Q^2) - \frac{4\alpha_s^2 N_c}{3C_F R^2} \frac{1}{Q^2} [xG(x,Q^2)]^2 . \quad (4.2)$$

The nonlinear term accounting for gluon fusion comes with a negative sign and dominates for large gluon densities $xG(x,Q^2)$ leading to a suppression of the linear term.

Next steps towards a theory for modelling saturation at high energies were an approach by Balitsky [18] who constructed an infinite hierarchy of coupled equations for Wilson line operators and an equation by Kovchegov [19] derived independently in the *colour dipole* approach [34]. The Kovchegov equation is a nonlinear equation for the dipole scattering amplitude valid in the leading $\log 1/x$ approximation. In the mean field approximation, the first equation of the Balitsky hierarchy decouples, and is equivalent to the Kovchegov equation. Therefore, we shall from now on referring to them as the Balitsky-Kovchegov (BK) equation. Clearly, BK equation is also an approximation. A complementary approach initiated the JIMWLK equation, an evolution equation that describes the change of the correlation functions of the colour charge density in the hadron wavefunction [35, 36]. An effective theory which describes high parton densities within hadronic and nuclear wave functions at small x is the Color Glass Condensate [37]. The outline of this Chapter is the following: We firstly discuss the notion of parton saturation and then, within the dipole picture, we show the transition from linear to non-linear evolution. We present numerical solutions for the BK and BFKL equations using the same initial condition and we finally conclude by defining what saturation scale is.

4.1 The notion of parton saturation

The steep rise of the parton density in high energy limits, or in other words at $x \to 0$ as predicted by BFKL, must be tamed in order not to violate unitarity. It is precisely the strong growth of the gluon density that eventually leads to a situation in which individual partons necessarily overlap and, therefore, finite density effects need to be included in the evolution. It is then that we say that partonic gluon density saturates. The schematic picture of the saturation phenomenon is shown in Fig. 4.1. It depicts the

[1] It is generally believed, that the parton saturation mechanism leads to the unitarization of the cross section at high energies. Unfortunately, the problem is quite complex since the parton saturation is purely perturbative mechanism, while the Froissart bound has been derived from general principles and it refers to the QCD as to a complete theory of strong interactions including the non-perturbative effects.

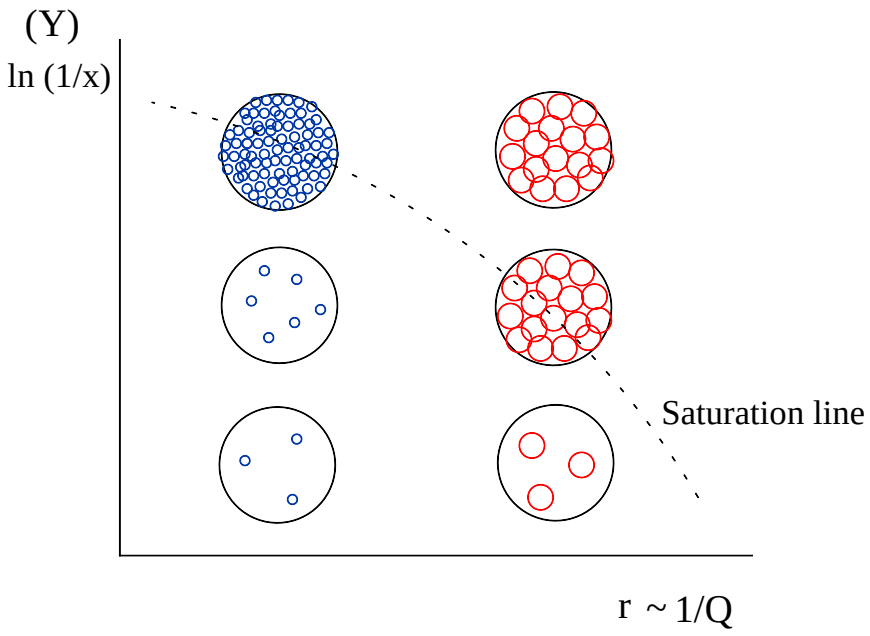

Figure 4.1: Schematic view of parton saturation. Above the Saturation line is the saturation region.

evolution in energy of the same hadronic system that is probed by two photons with different virtualities. The system in the left hand side is probed by a photon with larger virtuality that the one of the photon in the right hand side. The vertical axis is the rapidity, Y, axis whereas the horizontal one measures the size of the partons. The size of the partons is the inverse of the photon momentum, $r \sim 1/Q$, and thus, in the right column, the partons have a 'bigger size' than the ones in the left column. As we increase the energy, we 'produce' more and more partons (gluons). In both columns, the average size of the new produced gluons is bounded to be of the same order as the initial ones. We must remember that in BFKL dynamics there is strong ordering in rapidities but the transverse momenta are all of the same order. For both systems a point is reached where the limited size of the hadron will soon impose an upper bound to the number of gluons that can be accommodated. Then the system becomes saturated and recombination effects need to be taken into account. The difference between the two systems in Fig. 4.1 is that the one to the right becomes sooner saturated because of the initially bigger size of the partons. The Saturation line signifies that in the region above it we are in the saturation regime[2]. Therefore, if

[2]We will see later that this 'naive' at first sight image we get from Fig. 4.1 is very close to the image we draw after a precise numerical analysis, see Fig. 4.17.

one wants to account for gluon fusion, apart from production diagrams, one has to include additional diagrams which take into account gluon recombination. These diagrams look like the right hand side graph in Fig. 4.2 and they are called *fan diagrams*. In these, multiple BFKL ladders start from different partons in the hadron (one should imagine it somewhere below the graph) and due to high density of gluons they cannot stay independent so they recombine, resulting in a damped gluon density seen by the projectile (which one should imagine somewhere above the graph). Inclusion of this kind of diagrams leads to evolution equations which are nonlinear like for example Eq. 4.2.

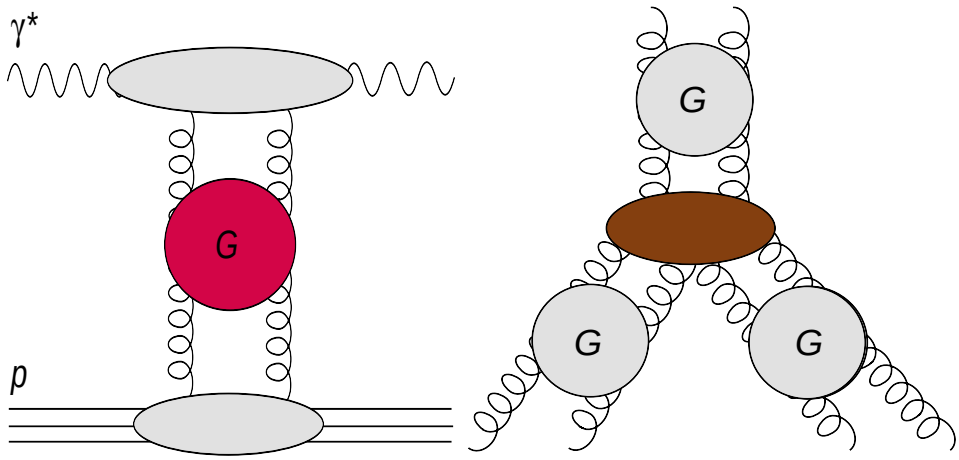

Figure 4.2: Left: linear evolution. Right: fan diagrams.

4.2 From BFKL to the BK equation in the colour dipole picture

4.2.1 Colour dipole picture of DIS

Colour dipole picture [34] is a different approach to DIS with an important feature: It provides a physically intuitive picture of the process by describing low x DIS in the proton rest frame. The virtual photon splits into a quark-antiquark pair at large distances from the proton target. It is then the $q\bar{q}$ pair that interacts with the proton after long time. The interaction time is much shorter than the life time of the pair and the pair appears to be frozen during the scattering. This happens because due to the uncertainty principal, the formation time will be $\tau_{for} \sim 1/\Delta E_{for}$ and respectively the interaction time will be: $\tau_{int} \sim R_p$ where R_p is the radius of the proton. ΔE_{for} proves to behave like x($\Delta E_{for} \sim x$) and since we are in the $x \to 0$

region, τ_{for} is much larger than τ_{int}, in other words we can assume that what we practically have is fixed-size $q\bar{q}$ pair scattering off a nucleon. The

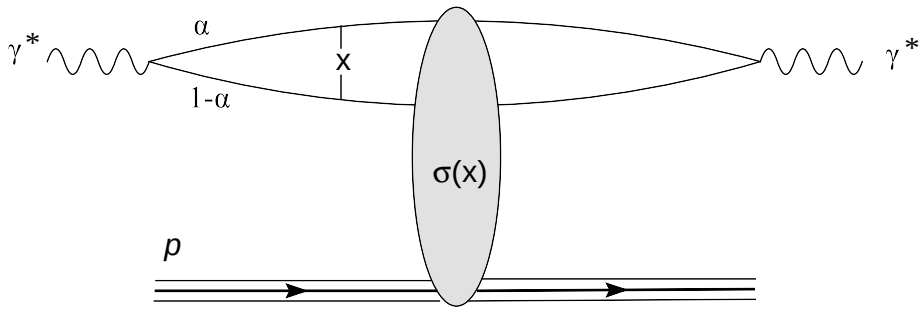

Figure 4.3: The $q\bar{q}$ pair appears to be frozen during the interaction with the nucleon.

total cross section for $\gamma^{\star}p$ scattering will then be:

$$\sigma_{\gamma^* p} = \int d\mathbf{x}\, d\alpha\, \psi^*(\mathbf{x},\alpha)\, \sigma_{q\bar{q}}(\mathbf{x})\, \psi(\mathbf{x},\alpha). \tag{4.3}$$

$\psi(\mathbf{x},\alpha)$ is the photon wave function that describes the fluctuation of the photon into a colour dipole, namely a $q\bar{q}$ pair, in which the quark and anti-quark carry light cone momenta fractions α and $(1-\alpha)$ of the virtual photon. $\mathbf{x}$ is the transverse dipole size and $\sigma_{q\bar{q}}$ is the cross section describing the interaction between the dipole and the proton (Fig 4.3). In the proton

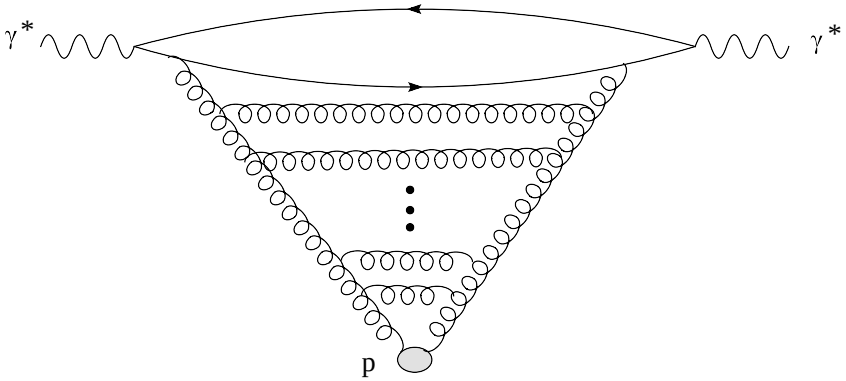

Figure 4.4: Gluon cascade development in the proton rest frame.

rest frame, one must imagine that the development of the gluon cascade starts from the initial dipole (Fig. 4.4).

4.2.2 BFKL in the dipole picture

Let us consider the wave function in the momentum space of a heavy quark-antiquark pair, *onium*, shown in Fig. 4.5,

$$\psi^{(0)}(\mathbf{k}_1, z_1) \,, \tag{4.4}$$

where $\mathbf{k}_1$ is the transverse momentum of the quark and $z_1 = \frac{k_{1+}}{p_+}$ is the fraction of light cone momentum carried by the quark ($1 - z$ for the anti-quark). Let us also denote with k_0 the momentum of the anti-quark. It

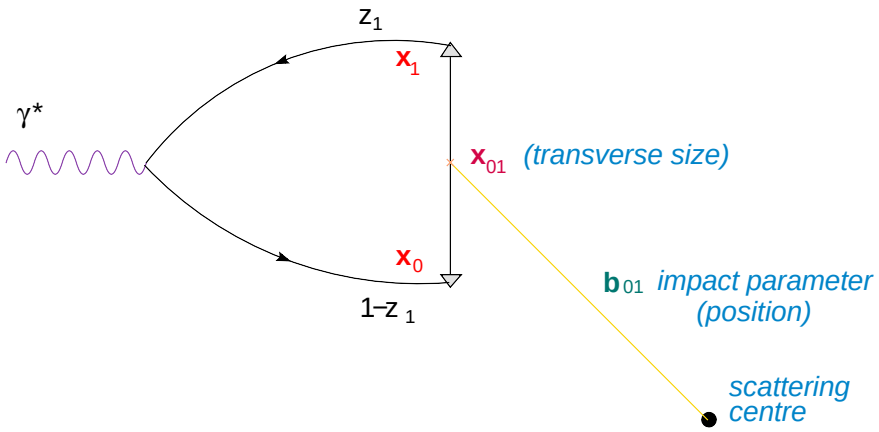

Figure 4.5: Heavy quark-antiquark dipole *onium*.

will be convenient to work in the transverse coordinate space since as we mentioned before the transverse size of the initial dipole remains frozen during the time of the soft gluon emissions, so if we average colour, and helicity indices we will have for the wave function:

$$\psi^{(0)}(\mathbf{x}_0, \mathbf{x}_1, z_1) \;=\; \int \frac{d^2\mathbf{k}_1}{(2\pi)^2} e^{i\mathbf{x}_{01}\cdot\mathbf{k}_1} \psi^{(0)}(\mathbf{k}_1, z_1) \,, \tag{4.5}$$

whereas for the impact factor it is:

$$\Phi^{(0)}(\mathbf{x}_0, \mathbf{x}_1, z_1) \;=\; \sum |\psi^{(0)}(\mathbf{x}_0, \mathbf{x}_1, z_1)|^2 \,, \tag{4.6}$$

where $\mathbf{x}_0$, $\mathbf{x}_1$ denote the positions (coordinates in configuration space) of the quark and antiquark respectively, which form the end points of the dipole and the sum is to be understood over all colour and polarisation indices. The transverse size will be $\mathbf{b}_{01} = \mathbf{b}_0 - \mathbf{b}_1$ and the impact parameter (position) of the dipole: $\mathbf{b}_{01} = \frac{\mathbf{b}_0 + \mathbf{b}_1}{2}$. In the following we will assume that there will be no impact parameter dependence of our evolution equations[3]. Suppose

[3]This implies that we are dealing with an homogeneous target, and dipoles with size much smaller than the radius of the target.

now that the quark (antiquark) of the onium, emits a soft gluon 2. "soft" means that $z_2 \ll z_1, (1-z_1)$. Then one finds that the wave function of this

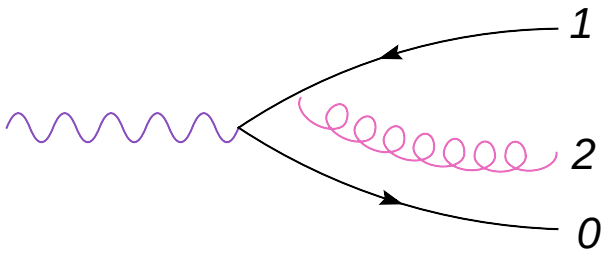

Figure 4.6: Onium with an additional single soft gluon.

new state $q\bar{q}g$, $\Psi^{(1)}$, is in relation to the onium wave function without any soft gluons $\Psi^{(0)}$:

$$|\Psi^{(1)}|^2 = 4C_F \frac{\alpha_s}{\pi} \frac{\mathbf{x}_{01}^2}{\mathbf{x}_{20}^2 \mathbf{x}_{12}^2} |\Psi^{(0)}|^2 \tag{4.7}$$

and the relation between the corresponding impact factors, $\Phi^{(1)}$ and $\Phi^{(0)}$ is:

$$\Phi^{(1)}(\mathbf{x}_0, \mathbf{x}_1, z_1) = \frac{\alpha_s C_F}{\pi^2} \int_{z_0}^{z_1} \frac{dz_2}{z_2} \int d^2\mathbf{x}_2 \frac{\mathbf{x}_{01}^2}{\mathbf{x}_{20}^2 \mathbf{x}_{12}^2} \Phi^{(0)}(\mathbf{x}_0, \mathbf{x}_1, z_1) \, . \tag{4.8}$$

We obtain this last relation after computing the four diagrams in Fig. 4.7 If we go one step further and we consider a state with two soft gluons 2 and

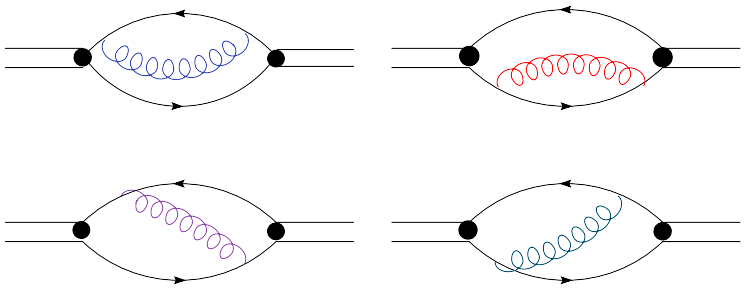

Figure 4.7: The diagrams that give $|\psi^{(1)}|^2$.

3, with strong ordering in rapidities being still valid, $z_3 \ll z_2 \ll z_1, (1-z_1)$, one understands that the situation becomes much more complicated since the possible configurations for the emissions are now not four but many more.[4] Nevertheless, we can simplify things if we go to the large-Nc limit. In this case, gluons can be represented by $q\bar{q}$ double lines, and the non-planar diagrams are suppressed with respect to the planar ones (planar are the ones with no intercepting quark lines) by powers of $\frac{1}{N_c}$. By calculating

[4]Gluon 3 can now be emitted from the quark or the anti-quark or the gluon 2 etc.

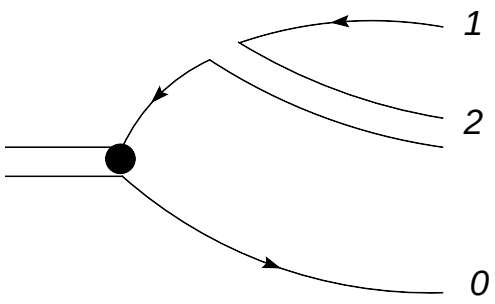

Figure 4.8: The planar diagram equivalent to the diagram in Fig. 4.6.

only the contributions from the planar diagrams one gets:

$$|\Psi^{(2)}|^2 = 2N_c\frac{\alpha_s}{\pi}\left(\frac{\mathbf{x}_{21}^2}{\mathbf{x}_{31}^2\mathbf{x}_{32}^2} + \frac{\mathbf{x}_{20}^2}{\mathbf{x}_{30}^2\mathbf{x}_{32}^2}\right)|\Psi^{(1)}|^2\,. \tag{4.9}$$

It is evident that the emission of one additional gluon is equivalent to the splitting of the original dipole $(0,1)$ into two dipoles $(0,2)$ and $(2,1)$ with the probability of branching given by the measure

$$d^2\mathbf{x}_2\frac{\mathbf{x}_{01}^2}{\mathbf{x}_{20}^2\mathbf{x}_{12}^2}\,. \tag{4.10}$$

The above quantity is the BFKL kernel in the dipole picture:

$$\mathcal{K} = \left(\frac{\alpha_s N_c}{\pi}\right)\frac{\mathbf{x}_{01}^2}{\mathbf{x}_{20}^2\mathbf{x}_{12}^2}\,. \tag{4.11}$$

If the process of emissions of subsequent soft dipoles is iterated, then by

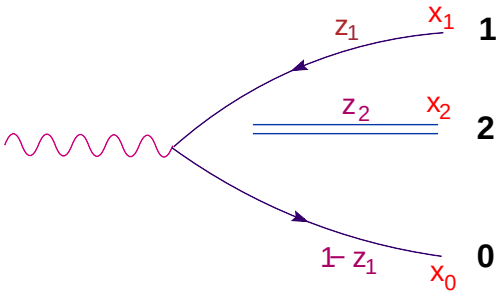

Figure 4.9: Onium wave function which consists of two dipoles.

investigating the relation between wave functions with n and $n+1$ dipoles, Mueller derived [34] the following differential equation for the scattering amplitude of the dipole off the target:

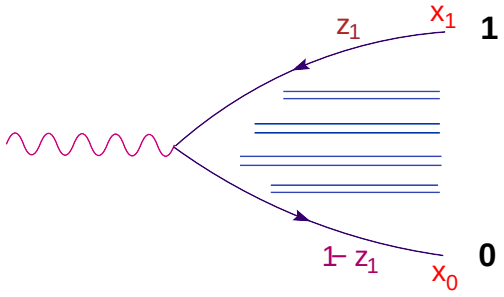

Figure 4.10: Onium wave function with arbitrary number of dipoles.

$$\frac{dN(\mathbf{x}_{01},\mathrm{Y})}{d\mathrm{Y}} = \bar{\alpha}_s \int \frac{d^2\mathbf{x}_2\,\mathbf{x}_{01}^2}{\mathbf{x}_{20}^2\,\mathbf{x}_{12}^2}\Big[N(\mathbf{x}_{20},\mathrm{Y}) + N(\mathbf{x}_{12},\mathrm{Y}) - N(\mathbf{x}_{01},\mathrm{Y})\Big], \quad (4.12)$$

where the evolution variable is the rapidity $\mathrm{Y} = \ln(1/z)$. It has to be stressed that only the contribution from the *single scattering* of one dipole on the target has been included in the derivation. Eq. 4.12 is the dipole version of the BFKL equation in the transverse coordinate space as derived in Ref. [34].

4.2.3 BK

One can generalise Eq. 4.12 by taking into account multiple scattering of many dipoles on the target, as in the right graph in Fig. 4.11 where the target now is a Nucleus. This leads to the BK equation:

$$\frac{dN(\mathbf{x_{01}},\mathrm{Y})}{d\mathrm{Y}} = \bar{\alpha}_s \int_\rho \frac{d^2\mathbf{x_2}}{2\,\pi}\,\frac{\mathbf{x_{01}^2}}{\mathbf{x_{02}^2 x_{12}^2}}\times \\ [2N(\mathbf{x_{02}},\mathrm{Y}) - N(\mathbf{x_{01}},\mathrm{Y}) - N(\mathbf{x_{02}},\mathrm{Y})N(\mathbf{x_{12}},\mathrm{Y})]\ . \quad (4.13)$$

It was shown [38] that Eq. 4.13 for the dipole density, appears as a special case of the nonlinear evolution equation which sums the fan diagrams for BFKL Green's functions in the Möbius representation. As with the GLR equation (Eq. 4.2), the nonlinear term $N(\mathbf{x}_{20},\mathrm{Y})\,N(\mathbf{x}_{12},\mathrm{Y})$ damps the amplitude for large N. We will make hereafter the additional assumption that the applicability of BK equation can be extended for the case when the target is a single proton. One has to stress that this multiple scattering is a completely incoherent process, i.e. dipoles scatter independently of each other and there are no target correlations. This is quite an important simplification which results in a relatively simple and closed evolution equation. The BK equation has the following probabilistic interpretation. When evolved in rapidity, the parent dipole with ends located at $\mathbf{x}_0$ and $\mathbf{x}_1$ emits a gluon, which corresponds in the large-N_c limit to two dipoles with ends $(\mathbf{x}_0,\mathbf{x}_2)$

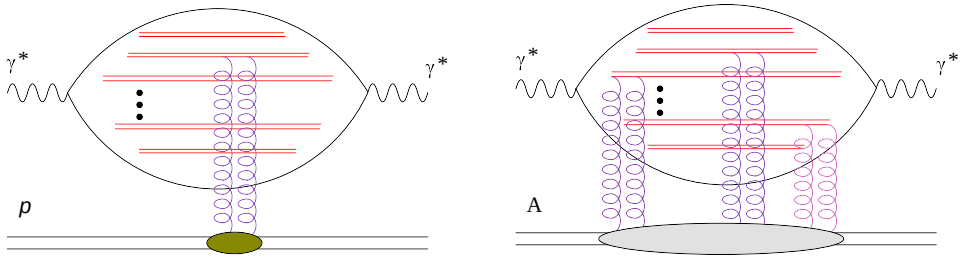

Figure 4.11: Left: single dipole scattering BFKL (linear) evolution (4.12). Right: multiple dipole scattering which results in nonlinear Balitsky-Kovchegov evolution equation (4.13).

and $(\mathbf{x}_2, \mathbf{x}_1)$, respectively. The probability of such emission is given by the BFKL kernel

$$\frac{\alpha_s N_c}{\pi} \frac{\mathbf{x}_{01}^2}{\mathbf{x}_{20}^2 \mathbf{x}_{12}^2} \,. \tag{4.14}$$

The variation with the rapidity is given by adding the probabilities for scaterring of the new dipoles, minus the scattering probability of the parent dipole, minus the non-linear term to avoid double counting. The BK equation ensures unitarity $|N(r, \mathrm{Y})| \leq 1$ since for $N(r, \mathrm{Y}) > 1$, the derivative with respect to Y in Eq. 4.13 becomes negative. We must emphasise here that we are referring to the unitarity for the scattering probability at a given impact parameter. However, BK itself, also violates S-matrix unitarity (Froissart bound) for scattering of a small projectile of size $\mathbf{x}_0$ on a target of size R_0 for rapidities $\mathrm{Y} > \frac{1}{\alpha_s N_c} \ln \frac{R_0}{\mathbf{x}_0}$ [39]. This is because the maximal value of the impact parameter that contributes to the scattering grows exponentially with rapidity Y.

4.3 Saturation scale and geometrical scaling

It is now well worthy to present solutions (numerical) of the BFKL (Eq. 4.12) and BK (Eq. 4.13) equations which will help us draw some very important comments. Since they both are integro-differential equations, one must start with an initial condition which will be fed in both of the equations and then the evolution with rapidity can be studied. The initial condition will be a profile function $N(r, \mathrm{Y}_0)$, giving the amplitude for the scattering of an initial dipole off a proton at a given rapidity Y_0, whereas $r \sim \frac{1}{Q}$ paremetrizes the initial dipole size. Solving the two equations (BFKL and BK), will provide us with the profile functions $N_{BFKL}(r, \mathrm{Y})$ and $N_{BK}(r, \mathrm{Y})$, which give the scattering amplitude for a dipole with a size r at a new rapidity Y. Since $N(r, \mathrm{Y})$ depends on Y and r, the solution will be a two dimensional surface. We present here the numerical solutions for BFKL and

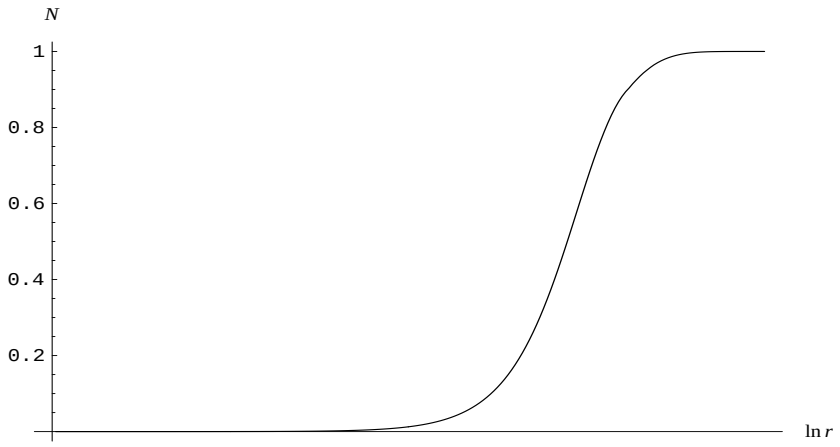

Figure 4.12: The initial condition used to numerically solve BK and BFKL equations. It is given by Eq. 5.17.

BK in Fig. 4.13 and Fig. 4.14 respectively, as a two dimensional function $N(\ln r, \mathrm{Y})$, while in Fig. 4.12 one can see the initial condition which was used as an input for both BFKL and BK equations. For each point $(\ln r, \mathrm{Y})$ the height N of the two dimensional surface gives the amplitude for the scattering when the initial dipole has size r and the rapidity in the process is Y. Upon a first inspection of Figs. 4.13 and 4.14, some very obvious remarks can be derived. Although we start with an initial condition that respects unitarity, recall that N stands for amplitude or in other words probability, for BFKL equation the solution violates unitarity (exceeds 1), whereas the solution for the BK respects unitarity (bounded by 1). Moreover, for BFKL the solution grows very fast with rapidity and it soon leads to exponential behaviour with respect to Y. Contrary, for BK the solution is always below 1 along the whole rapidity range. The solution for larger rapidities is certainly bigger for a given r but it is exactly the non-linear term that takes care of keeping the solution bounded by 1. One cannot speak of correct or wrong equation. The safe conclusion is that the applicability of the two equations is different. In high but not extremely high energies, BK and BFKL are having the same behaviour.

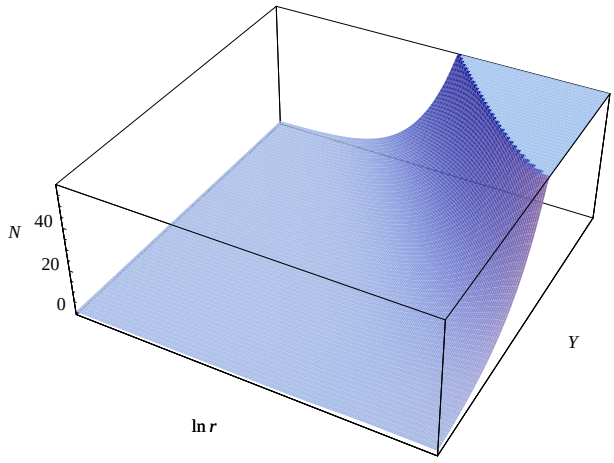

Figure 4.13: Solution of the BFKL equation. The initial condition used is the same as in Fig. 4.14. This is not obvious at first sight, because of the different ranges of the vertical axes, N, in the two figures.

The three dimensional plots are appropriate to gain an intuitive picture, however, in order to be more specific we need to have a closer look at the behaviour of the solutions with respect to r and Y separately. So, if we now suppose that we cut the surfaces along the $\ln r$-axis for a given Y (Fig. 4.16) and respectively along the Y-axis for a given r (Fig. 4.15) we can plot together the solutions for BK and BFKL. From Fig. 4.16, it is evident that the curve for the solution of the BK equation saturates to 1 for large rapidities, whereas the curve for BFKL exhibits an exponential behaviour with respect to Y.[5] We will mainly focus on Fig. 4.16 because we will use it for introducing quantitatively the notion of saturation. We can see that the curve for BK has distinct behaviours for small, medium and large r. In the small r region, it follows closely the linear solution, which suggests clearly that the non-linear effects in that region are small. For large r, the curve approaches smoothly the value 1 and we say that we are in the saturation region. This is the region where the non-linear effects are dominant and ensure the restoration of the unitarity. In the middle between small and large r we are in a transition region from linear to non-linear behaviour. We suppose that there is a scale (in momentum space) after or around which

[5]Remember that since $f(x) \sim x^{-\lambda}$ where $f(x)$ is the cross section calculated with the BFKL equation, and $\mathrm{Y} = \ln \frac{1}{x}$ then $f(\mathrm{Y}) \sim e^{\lambda \mathrm{Y}}$.

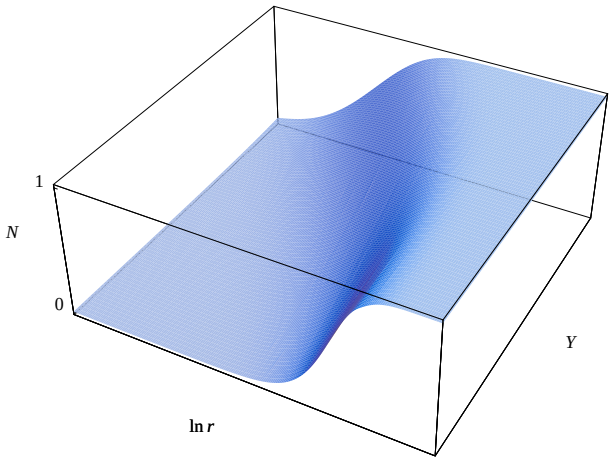

Figure 4.14: Solution of the BK.

the saturation begins to make itself manifest. We call this scale *saturation scale*, Q_s, and we define it as the scale where our non-linear solution (BK), is $\frac{1}{2}$, namely

$$Q = Q_s \Rightarrow N(r = \frac{2}{Q_2}) \equiv \frac{1}{2}. \tag{4.15}$$

We use the two-dimensional version of the uncertainty principle:

$$momentum = \frac{2}{distance}\,. \tag{4.16}$$

If we now go back to the three-dimensional plot in Fig. 4.16 and we cut the surface with a horizontal plane at height $\frac{1}{2}$, then what remains above the plane is what describes the saturation regime and what remains below describes the region where the non-linear effects are not dominant. Whats more, the projection of the line along which the cutting plane intercepts the surface-solution to the $(\ln r, \mathrm{Y})$ plane divides the later into two areas and each point of the projection gives the saturation scale as $Q_s = Q_s(\mathrm{Y})$. In Fig. 4.17 we present the contour plot for the solution from Fig. 4.16. The black curve-limit between the light and dark grey surfaces, is exactly the projection of the cutting line onto the $(\ln r, \mathrm{Y})$ plane (saturation line) and the dark grey area is the projection of the solution above the saturation line.

We will close this Section with some comments on a property that the solution for the BK equation exhibits in the saturation region[6], namely the

[6]Actually this property has been shown to extend its validity even to the region below

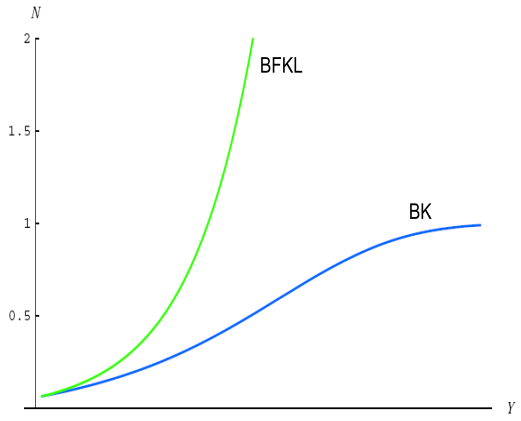

Figure 4.15: Solutions of the BFKL and BK equations at a given r_0, $N = N(r_0, \mathrm{Y})$

geometric scaling [40, 41]. Geometric scaling means that the amplitude $N(r, \mathrm{Y})$ becomes only a function of a dimensionless variable $\tau = r\,Q_s(\mathrm{Y})$ which is a combination between the saturation scale and the length r:

$$N(r, \mathrm{Y}) = N(r\,Q_s(\mathrm{Y})). \tag{4.17}$$

A very strong demonstration of this phenomenon was achieved by the authors in Ref. [40]. where they plotted combined HERA data on the total $\gamma^\star p$ cross section as a function of τ and they have shown that the data fall on the same curve, Fig. 4.18.

the saturation line.

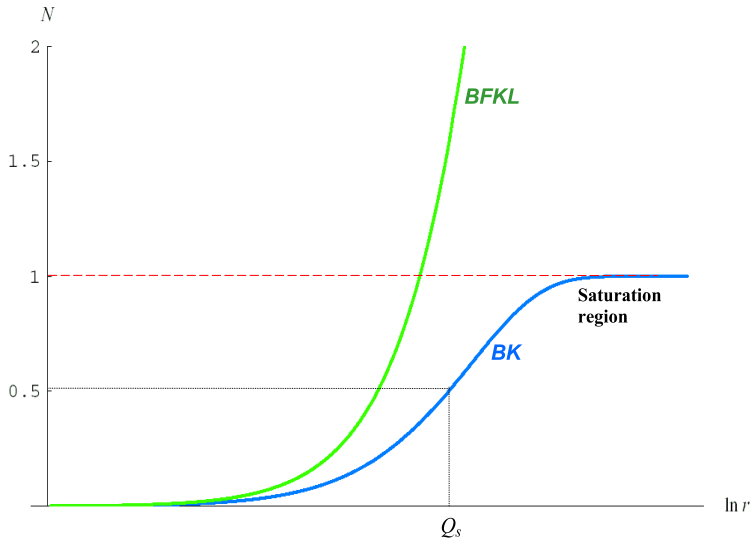

Figure 4.16: Solution of the BK equation at a given Y as a function of $\ln r$.

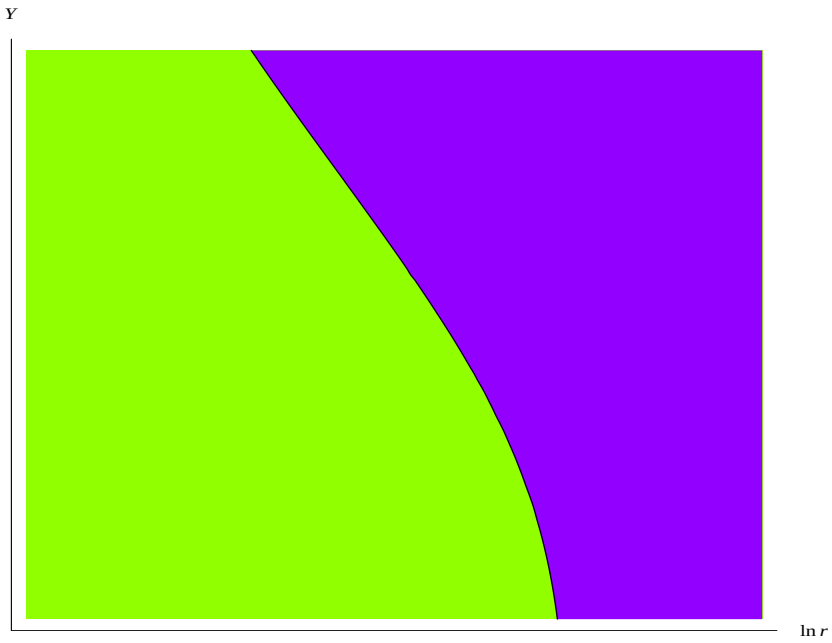

Figure 4.17: Contour plot at $N = 1/2$.

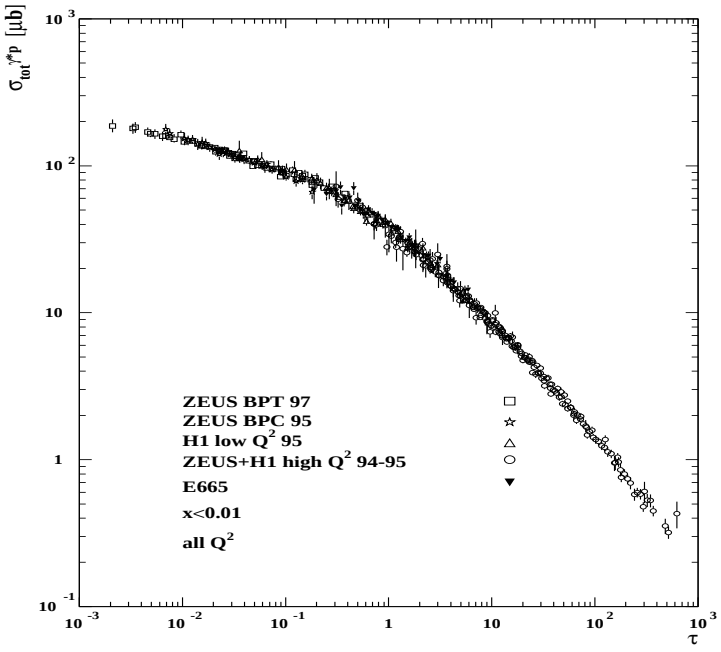

Figure 4.18: Geometric scaling.

Chapter 5

Higher Order Effects in Non Linear Evolution from a Veto in Rapidities

5.1 Introduction

The high energy behaviour of a parton system can be associated to the Balitsky–Fadin–Kuraev-Lipatov (BFKL) dynamics [1] as we have previously argued. At leading order (LO) the BFKL equation resums contributions of the form $(\alpha_s\,\mathrm{Y})^n$, with $\mathrm{Y} \sim \ln s$ being a rapidity variable. Linear evolution gives rise to a Pomeron–like behaviour of the scattering amplitudes with an intercept $\omega^{\mathrm{BFKL}} \simeq 0.5$. This power growth of the amplitude with energy violates s-channel unitarity at rapidities of the order of $\mathrm{Y} \sim 1/\alpha_s \ln 1/\alpha_s$ [42].

A theoretical possibility for the high energy growth of the amplitudes to be modified in a way consistent with unitarity is the idea of parton density saturation [17], which accounts for the possibility of parton annihilation, an essentially nonlinear effect. Present theoretical understanding views a system of saturated partons as a new state of matter called Colour Glass Condensate (CGC) (see e.g. Ref. [43] and references therein).

The fundamental quantity characterising the transition to the saturation regime, we have argued in the previous Chapter, is the so–called "saturation scale", $Q_s(\mathrm{Y})$. The determination of the rate of growth with rapidity of this saturation scale could be of a large importance for, e.g., structure function extrapolations from HERA to LHC kinematics. In the context of the well–known saturation model of Golec-Biernat and Wusthoff (GBW) [12], the saturation scale grows exponentially as $Q_s(\mathrm{Y}) \sim \exp(\lambda\,\mathrm{Y}/2)$ with $\lambda \simeq 0.29$.

Within the LO approximation BK equation is a theoretical tool with solid grounds in perturbative QCD suitable to study saturation phenomena

at high energies. The BK equation reads as we saw:

$$\frac{dN(\mathbf{x_0},\mathrm{Y})}{d\mathrm{Y}} = \bar{\alpha}_s \int_\rho \frac{d^2\mathbf{x_2}}{2\,\pi}\,\frac{\mathbf{x_{01}^2}}{\mathbf{x_{02}^2 x_{12}^2}}\times \\ [2N(\mathbf{x_{02}},\mathrm{Y}) - N(\mathbf{x_{01}},\mathrm{Y}) - N(\mathbf{x_{02}},\mathrm{Y})N(\mathbf{x_{12}},\mathrm{Y})]\,. \quad (5.1)$$

Here, the impact parameter dependence of the amplitude will be neglected, considering, in this way, a target of infinite size. ρ is an ultraviolet cutoff needed to regularise the integral which does not appear in physical quantities.

The BK equation has been studied both analytically [44, 45, 46, 47] and numerically [48, 49, 50, 51, 52, 53, 54, 55, 56]. Phenomenologically the BK equation provides a good description of DIS data from HERA [49, 57, 41, 58]. We remind, that the linear part of the BK equation is obtained in the leading soft gluon emission approximation keeping the strong coupling fixed and that the large N_c limit is used in order to write the nonlinear term as a product of two functions N. This limit is at the basis of the colour dipole picture and, to a large extent, it corresponds to a mean field theory without dipole correlations. The equation also neglects target correlations

It is very interesting to go beyond the original BK equation and relax some of the underlying assumptions outlined above. At present there is a large activity in this direction. Regarding the contribution of the N_c corrections they can be estimated to be up to 15% [53]. In this work we would like to focus on the higher order α_s corrections which are relevant, in particular, for phenomenological applications.

In principle, unitarity corrections based on LO estimates are expected to be important at rapidities of the order $\mathrm{Y} \sim 1/\alpha_s \ln 1/\alpha_s$, parametrically earlier than the next–to–leading (NLO) corrections which set in at $\mathrm{Y} \sim 1/\alpha_s^2$. It is also known that the NLO corrections to the linear BFKL equation significantly decrease the Pomeron intercept thus postponing the arrival of unitarity corrections to higher rapidities.

A complete nonlinear equation at NLO has not been derived yet. In the conventional approach based on s-channel unitarity, the forward BFKL kernel is known at NLO [8, 9]. A nonlinear evolution needs the knowledge of the non-forward kernel [59] together with the NLO impact factor [60, 61, 16]. However, a NLO study of the triple Pomeron vertex entering the BK equation has not been initiated yet. So far, the only exact result which has been reported is due to Balitsky and Belitsky [62] who have been able to compute a single NLO contribution with maximal nonlinearity, the N^3 term.

There have been some attempts to get insight about saturation at NLO using approximate methods. Triantafyllopoulos [63] has considered the renormalization group improved NLO BFKL equation with the presence

of a saturation boundary. His results show a decrease in the saturation scale growth as a function of rapidity towards the value $\lambda \simeq 0.3$ observed experimentally. A similar type of study based on the NLO BFKL has been recently reported in Ref. [64].

In this work we propose a new approach for the study of saturation effects including NLO corrections. We will introduce a constraint in the rapidity of the emitted gluons in the BK equation, a so–called "rapidity veto" [22, 23] which, for the linear part of the equation, is known to reproduce the bulk of the NLO corrections. In the next Section we revise how to introduce a veto in rapidity in the linear BFKL equation and apply this constraint to obtain an estimate of the saturation scale as a function of the veto. In Section 5.3 we apply the method of rapidity veto to the BK equation and study its influence on the energy growth of the saturation scale. In the last Section of this Chapter we present our summary.

5.2 The rapidity veto in BFKL and the saturation line

In the following the introduction of a rapidity veto as in Ref. [22, 23] will be shown. To impose the constraint that subsequent gluon emissions are separated by some minimum interval in rapidity, η, can be done writing the LO BFKL equation as an integral equation in rapidity, i.e.

$$f(\mathrm{Y},\gamma) \;=\; \int d\mathrm{Y}'\,\theta(\mathrm{Y}-\mathrm{Y}'-\eta)\,\bar{\alpha}_s\,\chi(\gamma)\,f(\mathrm{Y}',\gamma), \tag{5.2}$$

where γ corresponds to a Mellin transform in transverse momentum space and $\chi(\gamma) = 2\Psi(1) - \Psi(\gamma) - \Psi(1-\gamma)$ is the eigenvalue of the LO kernel. To go to the representation in the ω plane we use the transformation

$$f_\omega(\gamma) \;=\; \int d\mathrm{Y}\,e^{-\omega \mathrm{Y}}\,f(\mathrm{Y},\gamma). \tag{5.3}$$

The gluon Green's function as a function of s and transverse momenta, if we want to recover the notation of Chapter 2, can be obtained by the following transformations:

$$f(s,\boldsymbol{k}1,\boldsymbol{k}2) \;=\; \int \frac{d\omega}{2\pi i}\,\frac{d\gamma}{2\pi i}\,\left(\frac{s}{s_0}\right)^{\omega}\,\left(\frac{\boldsymbol{k}_1}{\boldsymbol{k}_2}\right)^{\gamma}\,\frac{1}{\omega \,-\, \chi(\gamma,\bar{\alpha}_s)}, \tag{5.4}$$

where $\chi(\gamma,\bar{\alpha}_s)$ is the generic BFKL kernel. By combining Eq. 5.2 and Eq. 5.3 we have

$$f_\omega(\gamma) \;=\; \bar{\alpha}_s\,\chi(\gamma)\int d\mathrm{Y}'\,f(\mathrm{Y}',\gamma)\int_{\mathrm{Y}'+\eta} d\mathrm{Y}\,e^{-\omega \mathrm{Y}}, \tag{5.5}$$

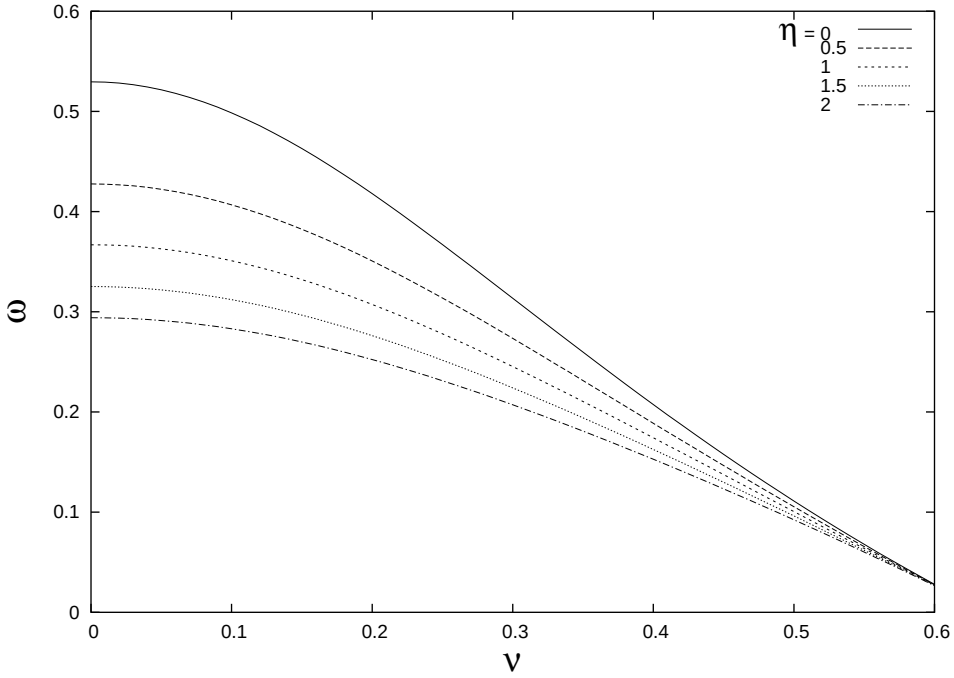

Figure 5.1: Dependence of the LO eigenvalue of the kernel on the veto upon ν.

therefore the effect of imposing the veto on the LO BFKL equation leads to an eigenvalue which is determined by the solution to

$$\omega \;=\; \bar{\alpha}_s \chi(\gamma)\, e^{-\eta\omega}. \tag{5.6}$$

It is worth noting that the solution to this equation respects the structure of a maximum at $\gamma = \frac{1}{2} + \mathrm{i}\,\nu$ for $\nu \simeq 0$ so that this region dominates at high energies. This is highlighted in Fig. 5.1 where the maxima are shown revealing how the original value of the Pomeron intercept decreases from about 0.5 to about 0.3 for a value of the veto of two units of rapidity. This is in agreement with other predictions from studies of the NLO gluon Green's function [10].

Now we calculate the influence of this veto in rapidity on the saturation scale. In the case of forward scattering the amplitude for a dipole of size $1/Q$ on a dipole of size $1/Q_0$ can be written as

$$\mathcal{N}\left(Q, Q_0, \mathrm{Y}\right) \;=\; \int d\gamma \int d\omega\, \mathcal{N}_0\left(\gamma\right) \exp\left(-\gamma L + \omega \mathrm{Y}\right) \frac{1}{\omega - \bar{\alpha}_s \chi\left(\gamma\right)}, \tag{5.7}$$

with $L \equiv \ln Q^2/Q_0^2$. The veto in rapidity is easily introduced via a modified

kernel as in Eq. 5.6:

$$\mathcal{N}\left(Q,Q_0,\mathrm{Y},\eta\right) \;=\; \int d\gamma \int d\omega\, \mathcal{N}_0\left(\gamma\right) \exp\left(-\gamma L+\omega \mathrm{Y}\right) \frac{1}{\omega-\bar{\alpha}_s \chi\left(\gamma\right) e^{-\eta\,\omega}}. \tag{5.8}$$

The saturation line, $L_s \equiv \ln Q_s^2(\mathrm{Y})/Q_0^2$ with $Q_s^2(\mathrm{Y}=0) \equiv Q_0^2$, can be defined as that with a stationary exponent:

$$-\gamma L_s + \omega(\gamma,\eta)\mathrm{Y} = 0, \tag{5.9}$$

where the introduction of the veto enforces

$$\omega(\gamma,\eta) \;\;=\;\; \bar{\alpha}_s \chi(\gamma) \exp\left(-\eta\,\omega(\gamma,\eta)\right). \tag{5.10}$$

At high energies the dominant region is that in the intersection with the saddle point $\bar{\gamma}$

$$-L_s + \left.\frac{\omega(\gamma,\eta)}{d\gamma}\right|_{\gamma=\bar{\gamma}} \mathrm{Y} \;\;=\;\; 0. \tag{5.11}$$

The solution to this system of equations provides an implicit equation for $\bar{\gamma}$:

$$\frac{\chi'(\bar{\gamma})}{\chi(\bar{\gamma})}\bar{\gamma} - 1 \;\;=\;\; \bar{\alpha}_s\,\eta\,\chi(\bar{\gamma}) \exp\left(1-\frac{\chi'(\bar{\gamma})}{\chi(\bar{\gamma})}\bar{\gamma}\right). \tag{5.12}$$

Consequently, when the rapidity veto is imposed it develops a dependence on the $\bar{\alpha}_s\eta$ product, $\bar{\gamma} = \bar{\gamma}\left(\bar{\alpha}_s\eta\right)$, and the saturation line reads now

$$L_s \;\;=\;\; \bar{\alpha}_s \frac{\chi(\bar{\gamma})}{\bar{\gamma}}\,\mathrm{Y}\, \exp\left(1-\frac{\chi'(\bar{\gamma})}{\chi(\bar{\gamma})}\bar{\gamma}\right) \equiv \lambda(\bar{\alpha}_s,\eta)\,\mathrm{Y}. \tag{5.13}$$

For a value of $\alpha_s = 0.2$ in Fig. 5.2 we have plotted the dependence of $\bar{\gamma}$ on the rapidity veto η. The effect of the constraint in rapidity is to increase the value of this critical $\bar{\gamma}$ from the well known $\bar{\gamma} \simeq 0.63$ (a value which is obtained for $\eta \to 0$ and/or in the limit of $\bar{\alpha}_s \to 0$) to about 0.69 for $\eta \sim 2.5$. This is in agreement with the recent results for this quantity of Ref. [64] where a resummed NLL BFKL equation was under study.

The evolution in energy is determined by the $dL_s/d\mathrm{Y} = \lambda(\bar{\alpha}_s,\eta)$ derivative. This λ term is calculated in Fig. 5.3 where it can be seen how the effect of the rapidity constraint is to delay the onset of the saturation line by means of decreasing λ at larger values of the veto. For zero veto it corresponds to the usual value of this linear coefficient of $\lambda \sim 0.93$, which can be calculated from Eq. 5.12 setting $\eta = 0$, $\alpha_s = 0.2$ and then introducing the result for $\bar{\gamma}$ in Eq. 5.13 reading $\lambda = \bar{\alpha}_s\chi(\bar{\gamma})/\bar{\gamma}$. At a rapidity constraint of $\eta = 2.5$ we obtain $\lambda \simeq 0.45$, in agreement with Ref. [64] and larger than that calculated in Ref. [63].

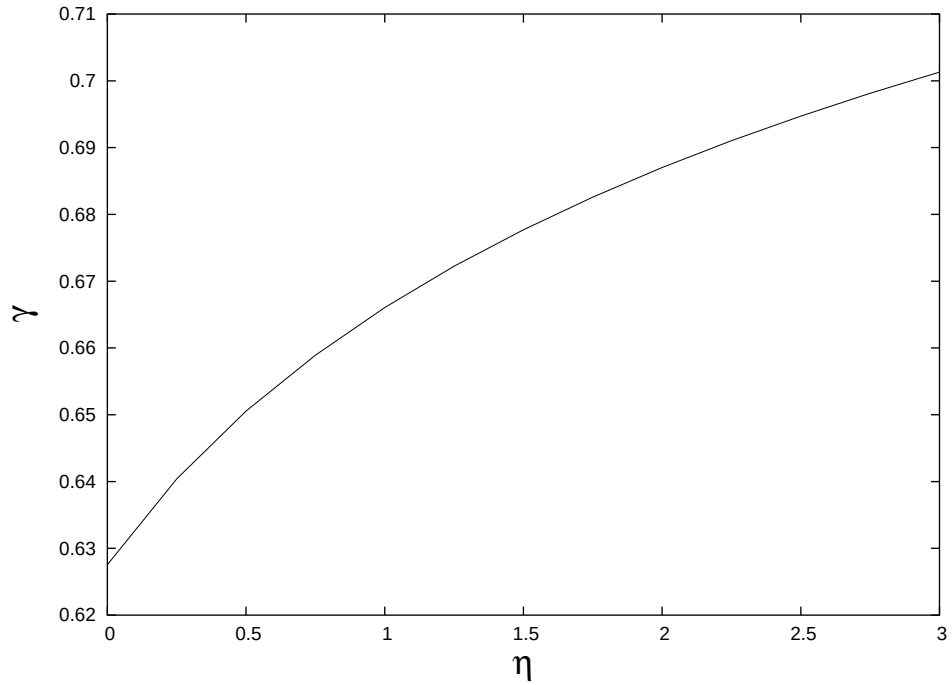

Figure 5.2: The solution to Eq. 5.12 as a function of the veto in rapidity, η.

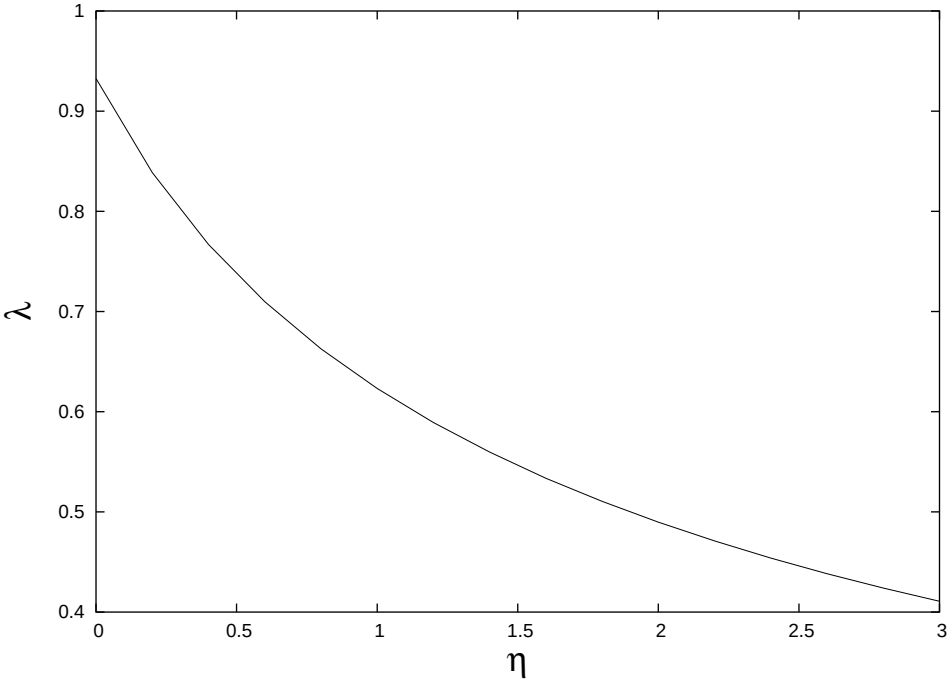

Figure 5.3: The saturation power (Eq. 5.13) as a function of the veto in rapidity, η.

These results have been produced in the case of linear evolution imposing a constraint which reproduces higher order corrections and estimating the position of the saturation line. In the following Section we introduce the veto in rapidities directly in the non–linear BK equation and study the consequences of this constraint on the evolution for phenomenological rapidities. We will see that the power growth of the saturation scale is slower, even for zero veto, mainly due to pre-asymptotic effects. We will then show how the effect of the veto in rapidity is very similar to that found in this Section: the effective power decreases as the veto is larger.

5.3 The rapidity veto in the BK equation

5.3.1 The fixed coupling case

To proceed with the numerical analysis it is convenient to write the BK equation for fixed coupling in the integral form

$$N(\mathbf{x_{01}},\mathrm{Y}) \;=\; N(\mathbf{x_{01}},\mathrm{Y}_0) \,+\, \bar{\alpha}_s \int_{\mathrm{Y}_0}^{\mathrm{Y}} d\,\mathrm{Y}' \int_\rho \frac{d^2\mathbf{x_2}}{2\,\pi}\,\frac{\mathbf{x_{01}^2}}{\mathbf{x_{02}^2}\,\mathbf{x_{12}^2}} \;\times \\ \left[\,2\,N(\mathbf{x_{02}},\mathrm{Y}') \,-\, N(\mathbf{x_{01}},\mathrm{Y}') \,-\, N(\mathbf{x_{02}},\mathrm{Y}')\,N(\mathbf{x_{12}},\mathrm{Y}')\right], \qquad (5.14)$$

with the initial condition being defined at the rapidity Y_0. As it was said above the rapidity veto prevents two emissions from being emitted close to each other in rapidity space. In this work we impose this veto in both the linear and non–linear parts of the BK equation. In this way we maintain the locality of the recombination process, corresponding to the quadratic term. Hence, the new equation simply reads

$$N(\mathbf{x_{01}},\mathrm{Y}) \;=\; N(\mathbf{x_{01}},\mathrm{Y}_0) \,+\, \bar{\alpha}_s \int_{\mathrm{Y}_0+\eta}^{\mathrm{Y}-\eta} d\,\mathrm{Y}' \int_\rho \frac{d^2\mathbf{x_2}}{2\,\pi}\,\frac{\mathbf{x_{01}^2}}{\mathbf{x_{02}^2}\,\mathbf{x_{12}^2}} \;\times \\ \left[\,2\,N(\mathbf{x_{02}},\mathrm{Y}') \,-\, N(\mathbf{x_{01}},\mathrm{Y}') \,-\, N(\mathbf{x_{02}},\mathrm{Y}')\,N(\mathbf{x_{12}},\mathrm{Y}')\right]. \qquad (5.15)$$

In the numerical implementation we work with the differential form of this equation with veto, i.e.,

$$\frac{dN(\mathbf{x_{01}},\mathrm{Y})}{d\mathrm{Y}} \;=\; \bar{\alpha}_s \int_\rho \frac{d^2\mathbf{x_2}}{2\,\pi}\,\frac{\mathbf{x_{01}^2}}{\mathbf{x_{02}^2}\,\mathbf{x_{12}^2}} \;\times \\ \left[\,2\,N(\mathbf{x_{02}},\mathrm{Y}-\eta) \,-\, N(\mathbf{x_{01}},\mathrm{Y}-\eta) \,-\, N(\mathbf{x_{02}},\mathrm{Y}-\eta)\,N(\mathbf{x_{12}},\mathrm{Y}-\eta)\right], \qquad (5.16)$$

which highlights the non–locality in rapidity after the constraint has been imposed. Expanding Eq. 5.16 in η (we assume $\eta \ll \mathrm{Y}$) one can easily verify that the corrections introduced via veto are proportional to α_s^2 and thus of the NLO.

In the context of the BK equation the imposition of the veto has the consequence of a small fluctuation above $N = 1$ when the function approaches the unitarity bound. These small fluctuations do not grow with rapidity. Technically this small violation of unitarity has its origin in the fact that the evolution is not stopped at $N(\mathrm{Y}) = 1$ since the derivative is computed at a retarded rapidity $\mathrm{Y} - \eta$, see Eq. 5.16. This small instability is not surprising since our approach is only an estimate of the NLO corrections. To fully preserve unitarity possibly we would have to introduce a correlation between coordinates and rapidity. Connecting with this point it is worth noticing that a generalisation of the BK equation proposed in Ref. [65] and amounting to having extra $1 - N(\mathbf{x_{01}}, Y)$ factor in front of the evolution kernel would respect unitarity even in the presence of a rapidity veto. In order to study the behaviour of the saturation scale, our analysis will be centred around the transition region $N \simeq 0.5$, which is a region not affected by the above issue.

Eq. 5.16 will be solved numerically for $x \leq x_0 = 0.01$, which corresponds to rapidities above $\mathrm{Y}_0 \simeq 4.65$. With this goal in mind we need to specify the initial conditions to the non–linear equation which, in principle, should be fitted to experimental data. Motivated by the phenomenological accuracy of the results in Ref. [49], the same initial conditions as those in that reference are used in the present work. These conditions were fitted to low $x\,F_2$ data for the BK equation with no veto and read

$$N(r, \mathrm{Y}_0) \;=\; 1 \,-\, \exp\left(-\alpha_s\, C_F\, r^2\, x\, G^{\mathrm{CTEQ}}/(\pi R^2)\right). \qquad (5.17)$$

Here α_s is taken to be LO running at the scale $4/r^2$, and $x\,G^{\mathrm{CTEQ}}$ is the LO CTEQ6 gluon distribution also computed at the scale $4/r^2$. The initial condition in Eq. 5.17 is smoothly extrapolated to $N = 1$ at very large distances using the method proposed in Ref. [41] and implemented in Ref. [49]. The parameter R stands for the effective proton size, $R^2 = 3.1\,\mathrm{GeV}^{-2}$, an output of the fit performed in Ref. [49]. For the numerical implementation of the veto it is necessary to generate the initial conditions in a band of width η between Y_0 and $\mathrm{Y}_0 - \eta$. The reason for this becomes clear if we think the evolution in rapidity Y as a process in which $N(r, \mathrm{Y})$ is the input for the next step which will give us $N(r, \mathrm{Y} + \delta\mathrm{Y})$. In the non zero veto case in order to compute $N(r, \mathrm{Y} + \delta\mathrm{Y})$ one would need to consider $N(r, \mathrm{Y} - \eta + \delta\mathrm{Y})$. Hence, since we start at Y_0 we need a band of initial conditions that will span the space between $\mathrm{Y}_0 - \eta$ and Y_0. As there is no evolution in energy along that band we assume the initial conditions to be independent of Y and equal to $N(r, \mathrm{Y}_0)$ on the band.

In Fig. 5.4 the first result for the solution to the BK equation is shown. There it can be seen how the amplitude N starts at zero for small transverse distances r (colour transparency) to reach the saturation regime $N \sim 1$ at r about 4 GeV^{-1}. This trend is general for all values of the rapidity veto

but, as a new feature, we observe how the arrival of the saturation of the amplitude is delayed as the veto increases. This first plot was done for a rapidity of 10 and a fixed coupling of $\alpha_s = 0.2$. In Fig. 5.5 we highlight how

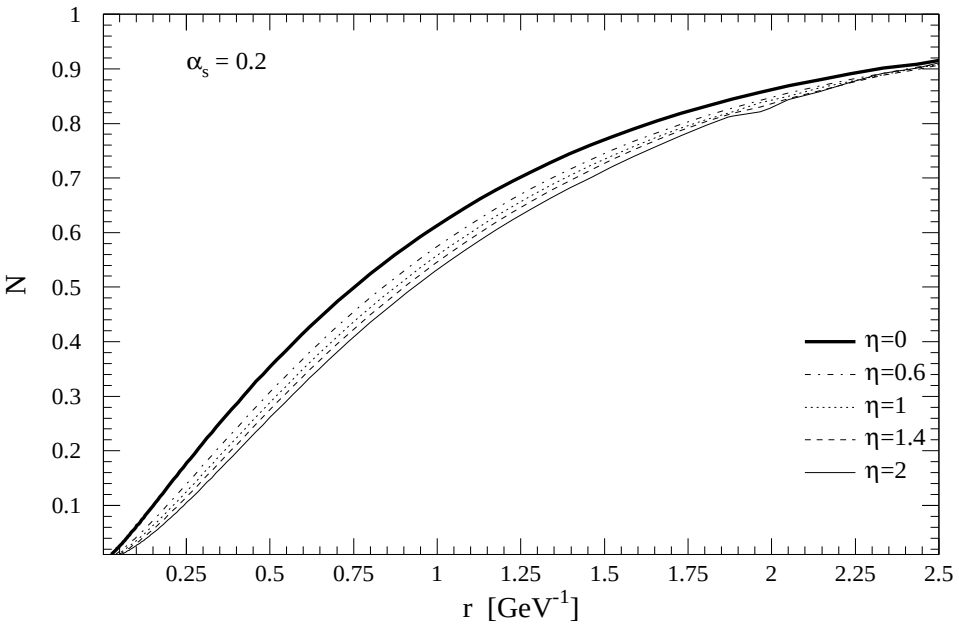

Figure 5.4: Solution to BK equation for different values of the veto as a function of r, for Y = 10 and $\alpha_s = 0.2$.

in a region of larger rapidity, Y = 14 saturation arises earlier in r for the set of initial conditions we have chosen. In this case of larger centre–of–mass energy the effect of the veto is more dramatic, considerably delaying the onset of saturation.

The major effect of the rapidity constraint comes when studying how the BK amplitude evolves with energy. As the intercept in the linear part is significantly reduced when higher order corrections are taken into account the saturation of the amplitude comes also later in rapidities. To illustrate this point we plot Fig. 5.6, where we have chosen a typical value of $r = 0.75$ GeV^{-1}. Once again our estimated NLO corrections do delay the onset of saturation. To make this statement more quantitative we now proceed to study the saturation scale and its dependence with energy. Different definitions of the saturation scale can be associated with the step like function N [41]. They might lead to different normalisations although the

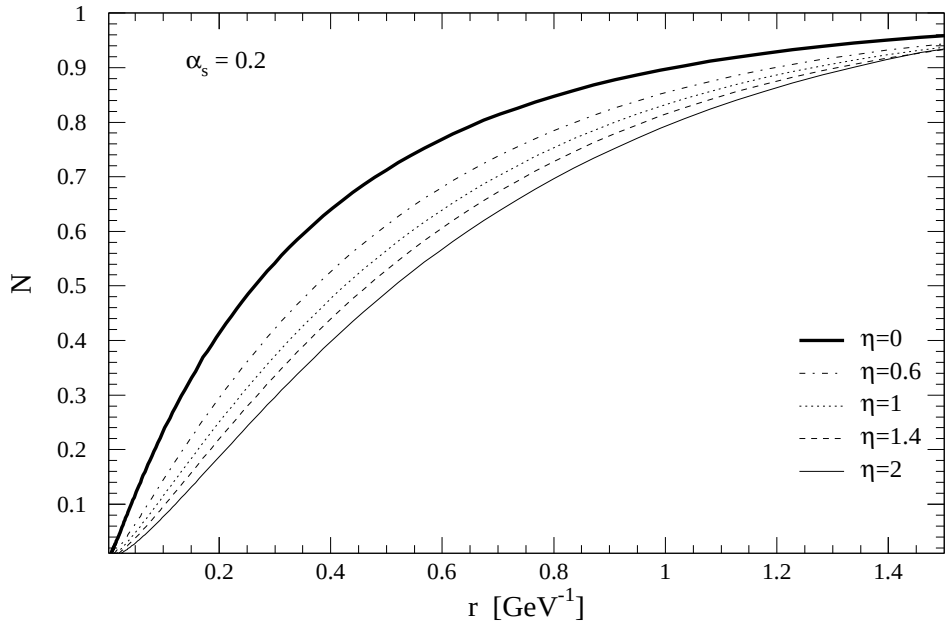

Figure 5.5: Solution to BK equation for different values of the veto as a function of r, for Y = 14 and $\alpha_s = 0.2$

energy dependence is qualitatively unique. For the sake of simplicity here, as in Chapter 4, we adopt the choice proposed in [52] where it was taken at a point where N reaches half:

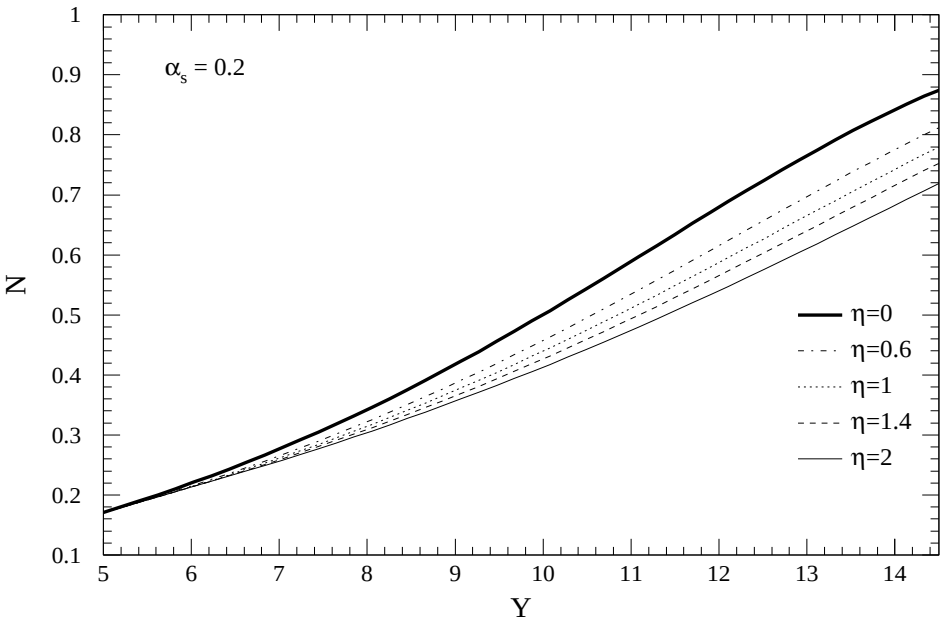

Figure 5.6: Solution to BK equation for different values of the veto as a function of the rapidity Y, for $r = 0.75$ GeV^{-1} and $\alpha_s = 0.2$.

$$N(r_s, \mathrm{Y}) \;=\; \frac{1}{2}, \tag{5.18}$$

with $r_s \equiv 2/Q_s$. For phenomenological applications the behaviour of $\ln Q_s^2$ with rapidity Y can be fitted linearly as in Eq. 5.13, i.e.,

$$Q_s^2 \;=\; Q_0^2\, e^{\lambda\, \mathrm{Y}}. \tag{5.19}$$

The numerical analysis of the rapidity dependence of this saturation scale is carried out in Fig. 5.7. This plot reflects very clearly how saturation tends to appear later in rapidity, in particular, for the veto which reproduces the NLO intercept, $\eta \sim 2$. We have also performed a linear fit to estimate the linear power of Eq. 5.13, λ, this fit was done for phenomenological rapidities between Y = 10 and Y = 15 so the expected value of the growth cannot

be as large as in Fig. 5.3 due to pre-asymptotic effects[1]. In fact, λ is much smaller at the beginning of the evolution for rapidities up to Y $\simeq$ 10. In

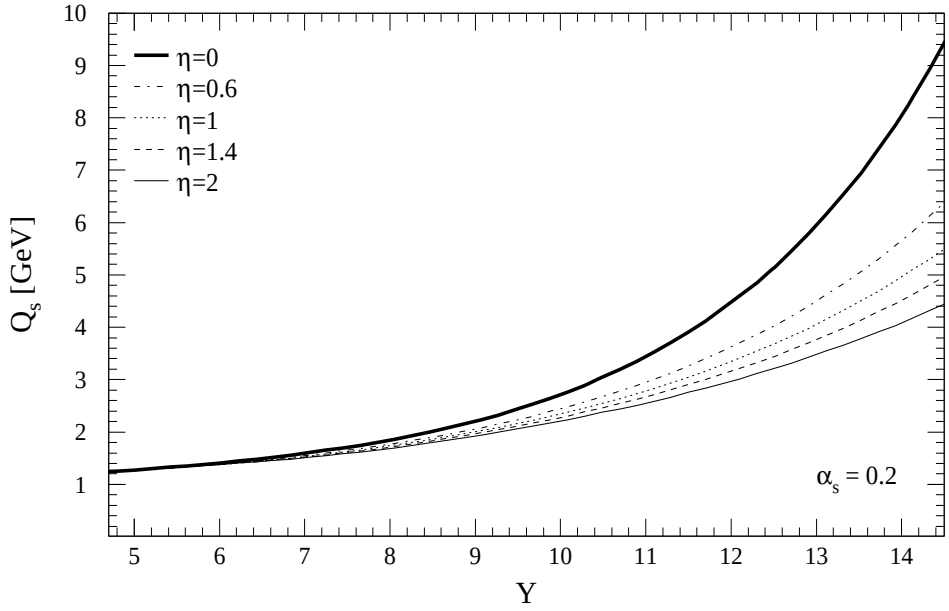

Figure 5.7: Rapidity dependence of the saturation scale for fixed α_s and different vetoes.

Fig. 5.8 we observe the transition power being of the order of 0.65 already at zero η. This value is smaller than the equivalent obtained in Sec. 5.2. Remarkably, the dependence on the rapidity veto is of the same functional form as in Fig. 5.3 with λ reaching ~ 0.31 at a veto of $\eta = 2.5$.

The main conclusion of this Section is to confirm the delay in energy space of the arrival of saturation when estimated higher order corrections are introduced in the BK equation with fixed coupling constant. The numerical results when we introduce the veto on the BK equation are consistent with those obtained from a more analytical approach in Section 5.2 based on the BFKL equation with a constraint in rapidity. In the following section the effect of this veto will be studied for phenomenological rapidities and running the QCD coupling.

[1]The preasymptotic effects in saturation scale have been studied in Refs. [66, 46, 47]. The numerical size of these terms is large at lower rapidities with the asymptotic values only reached at very large rapidities of the order of Y $\sim$ 100 (see [56] for a similar discussion).

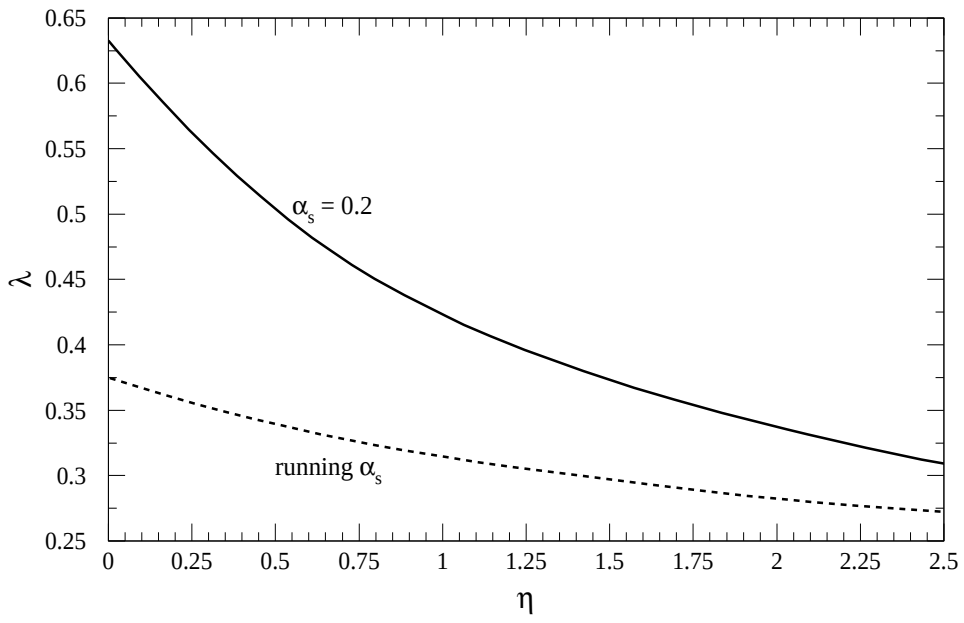

Figure 5.8: η dependence of λ with running and fixed $\alpha_s = 0.2$.

5.3.2 The running coupling case

The BK equation was originally derived for constant α_s, the introduction of the running is part of the NLO corrections. At present the use of the running α_s in the BK equation can only be done by modelling. In previous analysis introducing running seems to be phenomenologically favoured by the data [49]. This is because the effect of running α_s is to bring λ down to about 0.3 in the phenomenologically relevant region of $x \geq 10^{-7}$. The main concern of this Section is to study the stability of this value of $\lambda \sim 0.3$ when the veto is imposed on top of the running.

Similar to the initial conditions, α_s is taken at the leading order running with respect to the external scale $4/r^2$. At large distances α_s is frozen at the value $\simeq 0.5$. We have checked that our results are not sensitive to variations of this value.

Let us start with Fig. 5.9 where we again show the region of small r for the amplitude as calculated from the BK equation introducing the rapidity constraint, this time running the coupling. As previously found the effect of the higher order corrections is to delay saturation. The rapidity chosen for this plot is 14. It is worth pointing out that the effect of the veto is reduced if we compare Fig. 5.9 to Fig. 5.5, we will go back to this point soon below.

What about the energy dependence of the saturation scale? The answer to this question is plotted in Fig. 5.10 where the saturation scale is shown as a function of rapidity. The usual delay of the onset of saturation can be again observed although the effect of the estimated higher order corrections is smaller than for the case of fixed coupling in Fig. 5.7. To make this more explicit we calculate the dependence of the λ power in Eq. 5.13 as a function of the rapidity veto η in the case of running coupling [2] (Fig. 5.8). The main conclusion is that the effect of the veto is not so big in the running coupling case, taking λ from ~ 0.37 for $\eta = 0$ to about 0.27 for $\eta = 2.5$. This variation is much smaller than for the fixed coupling case.

The calculations in this Section teach us that once the coupling is allowed to run the influence of other higher order corrections is diminished. The prediction for the growth of the saturation scale with energy remains of the order of $\lambda \sim 0.3$ for phenomenological energies independently of the rapidity veto.

As a final remark, we have checked that the solutions to the BK equation for both fixed and running α_s cases exhibit the geometrical scaling property [40]. Namely, the amplitude $N(r, \mathrm{Y})$ is a function of the product $\tau = r\, Q_s(\mathrm{Y})$, that is $N(\tau)$. Scaling holds in the saturation domain $\tau > 2$

[2] It is known from analytic studies that, contrary to the fixed coupling case, for running coupling $\ln Q_s \sim \sqrt{Y}$. However, again due to large pre-asymptotic corrections [56], $\ln Q_s$ can be fitted linearly in rapidity for a limited range in Y relevant for phenomenology.

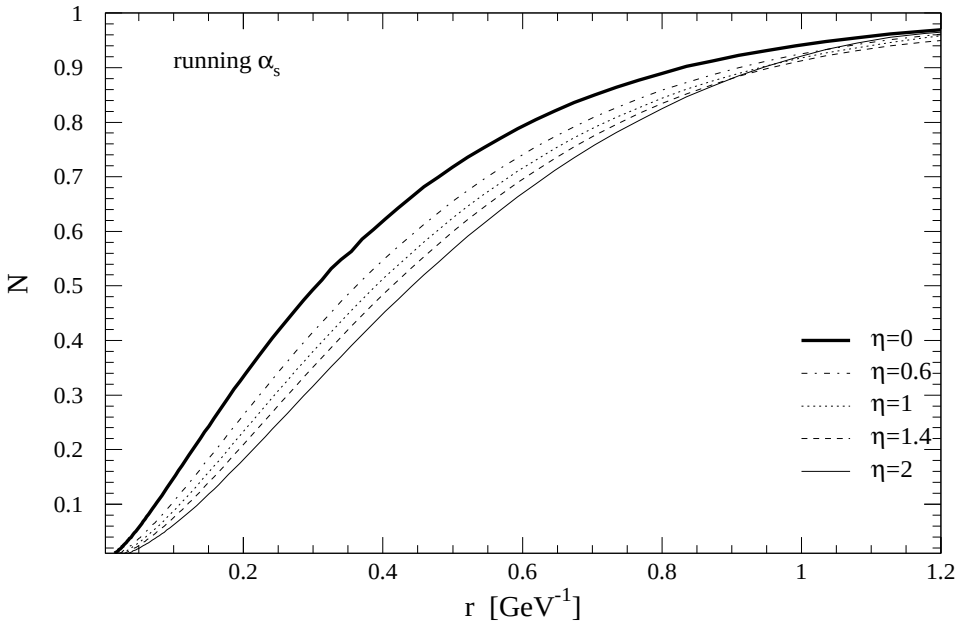

Figure 5.9: Solution of the BK equation for different vetoes as a function of r, for Y = 14 and running α_s.

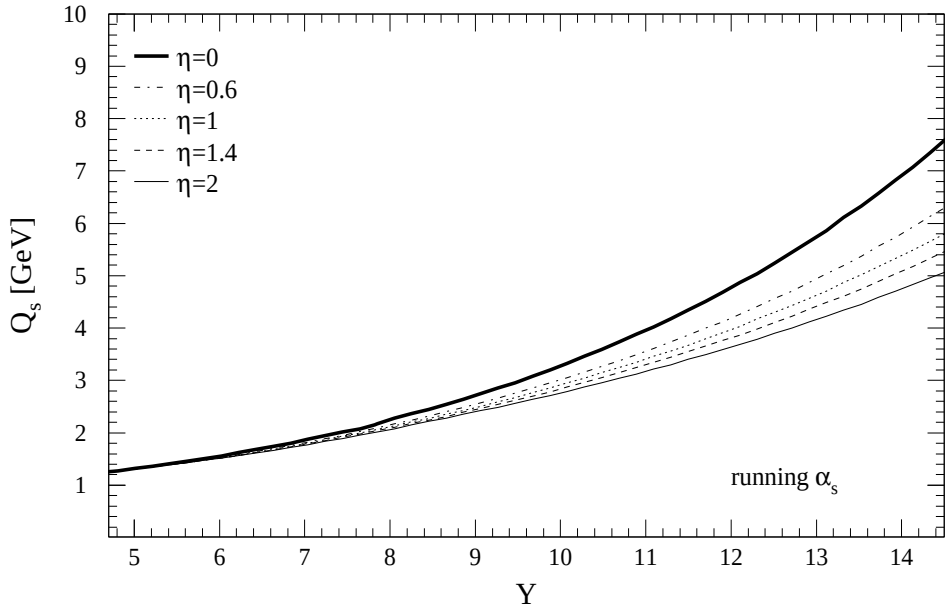

Figure 5.10: Y dependence of the saturation scale for running α_s.

and extends to a much broader region $\tau << 2$. For the BK equation with $\eta = 0$ scaling was shown in Refs. [50, 41, 51]. We have found that the scaling is still present after introducing a non-zero veto, suggesting the full NLO amplitude to be also a scaling function.

5.4 Higher order corrections and A dependence for heavy nuclei

In our previous analysis, we estimated higher order corrections to the Balitsky–Kovchegov equation by introducing a rapidity veto which forbids subsequent emissions to be very close in rapidity and is known to mimic higher order corrections to the linear BFKL equation. Assuming that the functional dependence of the saturation scale, Q_s, on the rapidity, Y, is of the form

$$Q_s(\mathrm{Y}) \sim e^{\lambda \mathrm{Y}}, \tag{5.20}$$

our numerical analysis was based on solving the BK equation for the case of the proton and for rapidities between 4.6 and 15. We want to extend here the numerical analysis for the case of Nuclei and for the same range of rapidities, seeking to estimate what will be impact on the A dependence of the Q_s after introducing higher order corrections.

We make the ansatz that the dependence of the saturation scale Q_s on A is of the form:

$$Q_{s,A}(\mathrm{Y}) \,=\, f(\mathrm{Y})\, A^{p(\mathrm{Y})}, \tag{5.21}$$

where $f(\mathrm{Y})$ is a function of rapidity that incorporates the main rapidity dependence of the saturation scale. We are interested to see what is the dependence of p on η if any.

We solved the BK equation for the case of realistic nuclei, namely for $A_{Na} = 22$, $A_{Ca} = 40$,$A_{Zn} = 65$, $A_{Xe} = 131$, and $A_{Au} = 197$. We also had the solution of the BK equation for the case of proton ($A = 1$) from our previous analysis. For each nucleus, we considered both cases of fixed and running a_s for different values of Veto, η, namely for $\eta = 0$, 0.6, 1, 1.4, 2 and 2.6. The initial conditions used for the case of nuclei were given by

$$N_A(r, \mathrm{Y}_0) = 1 \,-\, (1 \,-\, N(r, \mathrm{Y}_0))^{A^{1/3}}. \tag{5.22}$$

where $N(r, \mathrm{Y}_0)$ is defined in Eq. 5.17.

From Eq. 5.21 we obtain

$$\ln Q_{s,A}(\mathrm{Y}) \,=\, C(\mathrm{Y}) \,+ p(\mathrm{Y})\, \ln A. \tag{5.23}$$

Our ansatz that in $f(\mathrm{Y})$ is embedded the major rapidity dependence, will be justified if plotting $\ln Q_s$ versus $\ln A$ for a certain rapidity, yields a straight

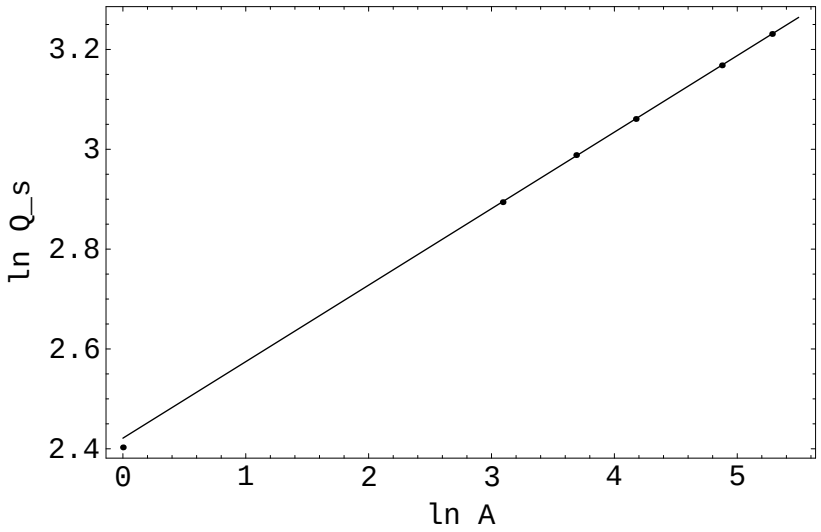

Figure 5.11: $\ln Q_s$ vs $\ln A$. The points are obtained after solving the BK equation for the different Nuclei and subsequently calculating the saturation scales. For this plot Y = 15 and $\eta = 0$. The curve is a linear fit to the points.

line. In Fig. 5.11, for Y = 15, $\eta = 0$ and fixed a_s we plot the points $(\ln Q_s, \ln A)$ along with a linear fit (straight line). The points that correspond to the heavy Nuclei lie all on the straight line, which is a factual justification for Eq. 5.21 The point at $\ln A = 0$ is obviously for the proton. The same picture holds over the whole range of our rapidities and it also holds when we switch the running of a_s on. Based on these facts, we tried to figure out how p = p(Y) changes when we consider the solutions with veto different than zero. For the case of fixed running coupling constant a_s there is not a clear picture as we need better numerical accuracy. There is a tendency for p to aquire smaller values with increasing Y, a trend that also survives after imposing a rapidity veto. However, for the case of running a_s things are more clear. At Y = 14.5 the value, of p is decreased by almost 30% comparing it with the one at Y = 5. Veto appears to make this decrease smaller. We consider these first results as very interesting. We present them here as a first insight. A fully quantitative analysis is needed though, before we are able to see clearly what conclusions we can safely draw. For that, we are bounded to increase the numerical accuracy of our code.

5.5 Conclusions

In this work higher order corrections to the Balitsky–Kovchegov equation have been estimated. This estimate has been based on the introduction of

a so–called "rapidity veto", which forbids two emissions to be very close in rapidity. It is known from Ref. [22, 23] that the introduction of a veto, η, of ~ 2.5 units of rapidity mimics the Pomeron intercept predicted by other resummations of the NLO BFKL equation. We have estimated these higher order corrections first using analytical arguments imposing the rapidity veto on the LO BFKL equation obtaining a power growth of the saturation scale of $\lambda \simeq 0.45$, for $\alpha_s = 0.2$, consistent with that calculated in Ref. [64] and larger than that obtained in Ref. [63], our main result being Eq. 5.12 , Eq. 5.13 and shown in Fig. 5.3.

We have then pursued a numerical analysis of the introduction of the rapidity constraint in the full Balitsky–Kovchegov equation for phenomenological rapidities, without using asymptotic arguments. For a fixed coupling constant of 0.2 we observe that the power λ decreases from ~ 0.65 for zero veto to ~ 0.31 for $\eta = 2.5$, with a dependence on the veto very similar to the previous analytical study, the main result plotted in Fig. 5.8. When running coupling effects are also taken into account the effect of imposing the veto is not so important taking λ at no veto from ~ 0.37 to ~ 0.27 for $\eta = 2.5$ (Fig. 5.8).

As follows from the present analysis the running coupling effects account for the bulk of the NLO corrections to the BK equation (see Fig. 5.8). Given that, as shown in Ref. [56], the dipole amplitude is not sensitive to the way the running is introduced, this suggests that phenomenological analysis including running coupling effects, as in Ref. [49], do provide reliable predictions. The results of this Chapter have been published in Ref. [67].

Chapter 6

QCD Corrections to $\gamma\gamma \to ZZ$

6.1 $\gamma\gamma \to ZZ$: Introduction

So far in this thesis we were concerned with higher QCD corrections and their impact in the Strong sector of the Standard Model. In this Chapter, we will investigate whether, pQCD corrections are relevant at all for the Electroweak sector.

The correct extension of the Standard Model (SM) and the determination of the electroweak symmetry breaking mechanism are one of the basic questions which have to be answered in the nearest future. Experimentally, we expect the first data and insights concerning these questions after the run of the Large Hadron Collider (LHC). Complementary, high precision measurements will come from the Next Linear Collider (NLC) e.g. TESLA, operating in the energy regime up to 1 TeV and providing a very clean environment. In addition one may have the capability of running the NLC in a $\gamma\gamma$ collision mode via Compton backscattering of laser photons off the linear collider electrons. Apart from the advantage of the higher luminosity, the energy of the initial photons can be determined more accurately than the energy of photons radiated in the e^+e^- collider mode. One of the important processes one will consider at the NLC is the production of vector bosons such as $\gamma\gamma \to ZZ$ [68].

Concerning the search of physics beyond the Standard Model, the fact that the first perturbative contribution starts at one loop makes the process $\gamma\gamma \to ZZ$ sensitive to a number of investigations. One is the search for the existence of anomalous triple and quartic vector boson couplings [69] or vector boson Higgs couplings [70]. The natural order of magnitude of these couplings [71] is small, so one needs to know the SM cross sections with a precision better than 1%. In order to get a detailed understanding of the spin structure of anomalous couplings, it is important to investigate the different helicity states of the outgoing Z bosons. Because of the absence of the tree

level contribution, this process is sensitive also to particles and new physics phenomena contributing through radiative corrections [72]. This leads to a method independent of and complementary to the direct production of new particles. Again, high precision of the Standard Model cross section is needed. In addition, the detection of CP violating phases [73] or effects due to the exchange of Kaluza-Klein gravitons in large extra dimension scenarios [74] have been discussed.

Another motivation to study the process $\gamma\gamma \to ZZ$ is its sensitivity to the Higgs sector. At high energies the biggest contribution to the cross section comes from the production of transverse polarised Z bosons in the kinematical limit of small scattering angles (helicity conserving channel). The dominant contribution to the scattering amplitudes is due to W loops and grows proportional to the scattering energy s. Compared to these leading contributions, the diagrams containing the Higgs contribution are suppressed by s^2. In contrast to this, in the production of longitudinal Z bosons the Higgs plays a crucial role. In this channel, both the Higgs contribution and the W loop are constant in s (up to powers of logarithms). For large Higgs masses the s-channel Higgs exchange in the scattering amplitude of $\gamma\gamma \to Z_L Z_L$ violates partial-wave unitarity [76, 75] and makes this helicity non-conserving case sensitive to the Higgs sector. Therefore we need to know the SM cross section with a high precision in order to disentangle different symmetry breaking scenarios.

In summary, the process $\gamma\gamma \to ZZ$ is an important tool to probe physics beyond the SM. In order to see deviations, high precision is needed, both on the experimental and on the theoretical side. A calculation at the lowest available order may not be accurate enough. Since the cross section gains its biggest contribution from small scattering angles, it is natural to ask whether QCD corrections could play a role in this kinematical regime. At high energies the most dominant corrections arise when the vector bosons fluctuate into quark-antiquark pairs, described by the boson impact factors, and these dipoles interact through gluon exchanges. At higher orders in α_s large logarithms in s emerge, leading to QCD corrections rising with the scattering energy. At very high energies these corrections will be large and cannot be neglected.

In this Chapter we address the question whether in the energy region of the NLC QCD corrections need to be taken into account. For this purpose we compute the differential cross section both for the electroweak and the QCD parts. For the helicity conserving channel the QCD corrections have been studied recently [77]. Here, we extend our analysis to the helicity non-conserving channel. The electroweak part was computed first in Ref. [68], but for our purposes we had to repeat the full one loop calculation. For the helicity conserving case it turns out that QCD corrections in the region of about 1 TeV are at the percent level and grow moderately with energy. For

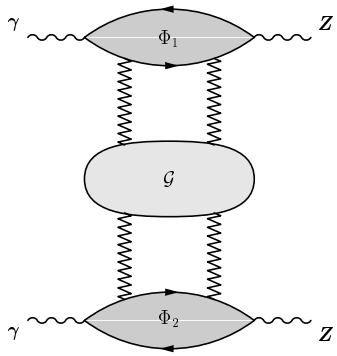

Figure 6.1: The BFKL exchange in the $\gamma\gamma \to ZZ$ elastic cross section. In this Chapter we change notation for the gluon Green's function, to be in accordance with Ref. [78].

the helicity breaking channel the QCD corrections to the differential cross section, at about 1 TeV, are of the same order, but they grow much faster with increasing energy.

6.2 QCD Corrections

The differential cross section including the QCD corrections reads:

$$\frac{d\sigma}{dp_T^2} = \frac{1}{16\pi s^2}|A_{EW} + A_{QCD}|^2\,, \tag{6.1}$$

with p_T being the exchanged transverse momenta, whereas the corrections to the pure electroweak amplitude are dictated by the interference term. The calculation was performed in the Feynman gauge.

The electroweak part of the amplitude was first computed in a full one loop calculation by Jikia [68] for Higgs masses over 300 GeV. In order to compute the above mentioned interference term, the results of [68] have been reproduced, however we used in this letter an up to date value of the top quark mass and a Higgs mass of $m_H = 115$ GeV. We adopted the definition of momenta and polarisation vectors from [79]. The Feynman diagrams were generated with *FeynArts* [80] and the resulting amplitudes were algebraically simplified using *FormCalc* [79]. To evaluate the one-loop integrals the package *LoopTools* [79, 81] was used. At small scattering angles the main contribution to the amplitude comes from the bosonic loop of the helicity conserving channel. These amplitudes are mainly imaginary and

proportional to s in this kinematical limit, in agreement with the calculation of [77] where a high energy approximation was used. For the helicity-flip channels no contributions proportional to s survive, thus these amplitudes are suppressed by one power of s compared to the helicity conserving cases. If one of the Z bosons has transverse and the other longitudinal polarisation, the amplitude is vanishing at the forward point ($p_T = 0$) due to angular momentum conservation.

The QCD part of the amplitude was calculated recently in Ref. [77], where the reader will find analytic expressions for A_{QCD}. In the small angle region these emerge when vector bosons fluctuate into a quark-antiquark pair and these dipoles interact through gluons. At the lowest order, when two gluons are exchanged in the t-channel, one obtains a contribution proportional to the scattering energy for both, the helicity conserving and helicity flip amplitudes. The radiation of more gluons enhances the cross section, since this higher order corrections provide large logarithms in energy, which are rising with the scattering energy. These contributions cannot be neglected at large energies. One possibility to take this into consideration is a resummation described by the LO BFKL equation [1] which gives an upper bound estimate of these effects.

The Feynman diagrams for A_{QCD} are illustrated in Fig. 6.1. Due to the high-energy factorisation one may calculate first the boson non-forward impact factors Φ associated to the external particles and integrate these with the BFKL Green's function $\mathcal{G}$. The BFKL Green's function is the result of the resummation of leading logarithms in energy, coming from diagrams of ladder topology, built with non-elementary reggeized gluons [1]. The boson impact factor is the convolution of the two boson wave functions which describes the probability that a boson fluctuates into a quark-antiquark pair [82]. The calculation was done for the kinematical region of small scattering angles in the high-energy approximation. Thus, one may neglect terms suppressed by powers of t/s, which simplifies the calculation significantly.

One important property of the helicity flip impact factors need particular attention concerning our further calculations: these impact factors are in general non-zero, they vanish only for forward scattering, where $p_T = 0$. This comes from a different symmetry behaviour of the transverse and longitudinal wave functions. Writing these in a coordinate space formulation [82], the longitudinal wave function is symmetric under the transformation of the dipole size vector $\mathbf{r} \to -\mathbf{r}$, while the transverse one is antisymmetric. Since the dipole interaction is also symmetric under this transformation, the convolution of this with a transverse and longitudinal wave function is antisymmetric, leading to the vanishing result for $p_T = 0$. For non-zero p_T, this symmetry properties are broken, resulting in non-vanishing helicity flip impact factors. Real and imaginary parts of the helicity flip impact factors are oscillating with p_T but shifted in a way that the absolute value of the

amplitude gives a smooth function (Fig. 9 of [77]). The helicity flip impact factors are constant in energy, thus the corresponding amplitudes are proportional to the scattering energy s [77, 82]. Because the electroweak parts of the helicity flip amplitude are suppressed by one power of s compared to the QCD ones, the QCD corrections will increase rapidly with energy, leading to significant corrections in the TeV energy regime.

6.3 Numerical Analysis

The order of magnitude of the QCD corrections is determined in a numerical analysis. Here we consider full circular polarisation of the incoming photons. For the QCD part of the amplitude, due to the huge rapidity separation of the bosons, it is only important if the helicity is conserved or broken in each impact factor. As a result, the amplitude $++ \to TT$ is equal to the amplitude $+- \to TT$ as well as to the amplitude with unpolarised photons. The mass of the Higgs boson was set to $m_H = 115$ GeV unless a different value is stated and the parameters $\alpha_W = \alpha/s_W^2$, $\alpha = 1/128$, $m_Z = 91.2$ GeV, $m_t = 174.3$ GeV and $\alpha_s(M_Z)$ have been used throughout the numerical computations. Since in the QCD expressions [77] the quark masses are always accompanied by the Z mass, they can be neglected in the numerical calculations apart from the top quark mass. The inclusion of the top quark mass reduces the QCD amplitude by 25%.

At high energies in the small angle limit one expects enhancements due to the appearance of large logarithms, these have been resummed in the BFKL scheme. The BFKL resummation was evaluated in the saddle point approximation [77]. The resummed leading logarithmic (LL) QCD corrections, as we previously argued, hold an uncertainty resulting from the scale which is not fixed at this order of the calculations. The scale was set to $s_0 = M_Z^2$ in the numerical evaluations. We stress that the resummed LL QCD corrections at the lower energies we consider, are overshooting what is expected from the true contribution, nevertheless they provide a first estimate of these corrections.

In Fig. 6.2(a-d) QCD corrections to the differential cross sections relative to the pure electorweak contributions are plotted. These relative corrections are defined as:

$$\Delta = \left(\frac{d\sigma_{QCD+EW}}{dp_T^2} - \frac{d\sigma_{EW}}{dp_T^2} \right) \Big/ \frac{d\sigma_{EW}}{dp_T^2} \tag{6.2}$$

and are presented as functions of p_T^2/M_Z^2 for centre of mass energies of 1 TeV and 3 TeV. At these energies $p_T^2/M_Z^2 = 4$ corresponds to values of $\cos\theta$

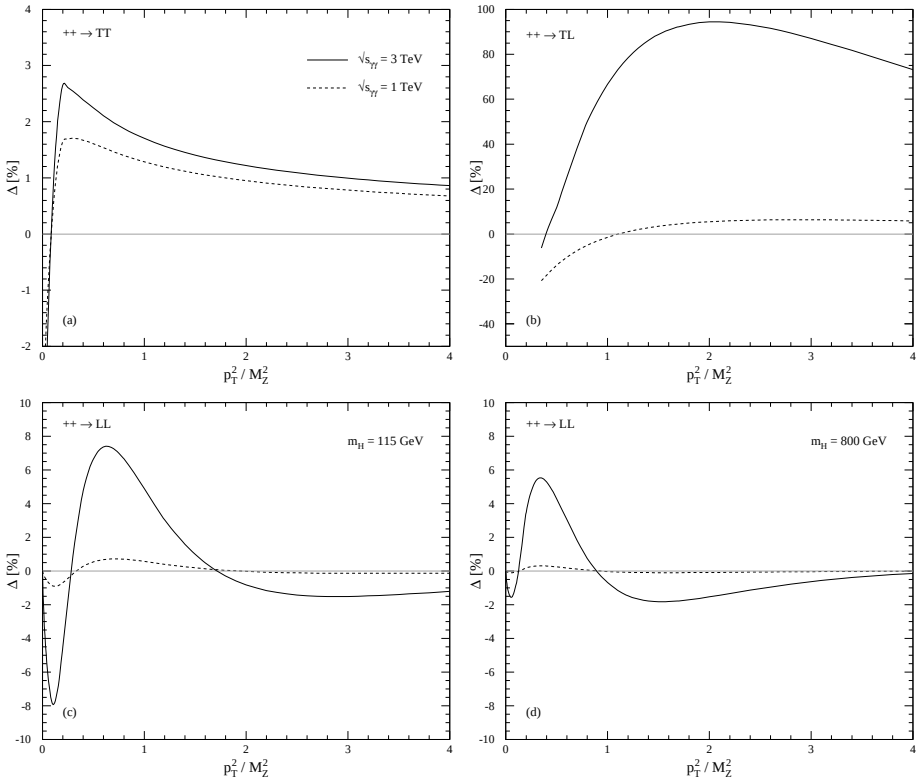

Figure 6.2: QCD corrections to the differential cross section relative to the pure EW contribution for different Z polarisations and centre of mass energies $\sqrt{s}$. The relative correction is defined as $\Delta = (\frac{d\sigma_{QCD+EW}}{dp_T^2} - \frac{d\sigma_{EW}}{dp_T^2})/\frac{d\sigma_{EW}}{dp_T^2}$.

(where θ is the scattering angle) of 0.90 and 0.99 respectively. Thus, for rising energy the scattering angle will be continously smaller for the same p_T values. For a TESLA detector it was proposed that the tracker system will reach values $\cos\theta < 0.993$, in this range one has a good measurement possibility [83]. Moreover, the decay products of the Z bosons will carry also transverse momenta, thus these particles can have bigger angles from the beam pipe.

Fig. 6.2(a) shows QCD corrections for transverse polarised Z bosons. The electroweak amplitude is mainly imaginary, in agreement with the result of [77] calculated in the high-energy approximation. Therefore, from the QCD amplitude it will be also the imaginary part which mainly accounts for the interference term. The relative corrections are of the order of percent level in the helicity conserving channel. For higher p_T they are approximately one percent and they are rising up to a few percent while

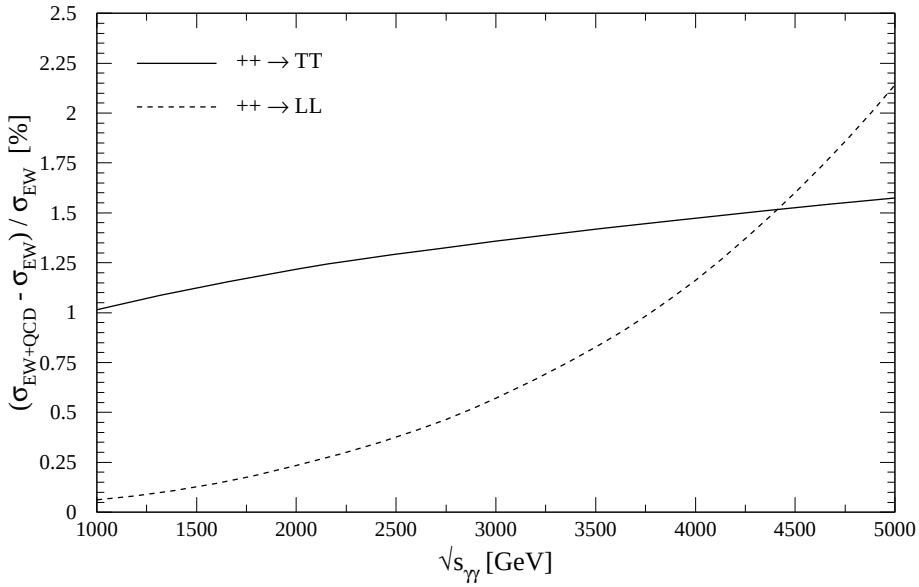

Figure 6.3: QCD corrections to the integrated cross section relative to the pure EW contribution for transverse and longitudinal polarised Z bosons. The integration region was chosen as $0 < p_T^2 < 4M_Z^2$.

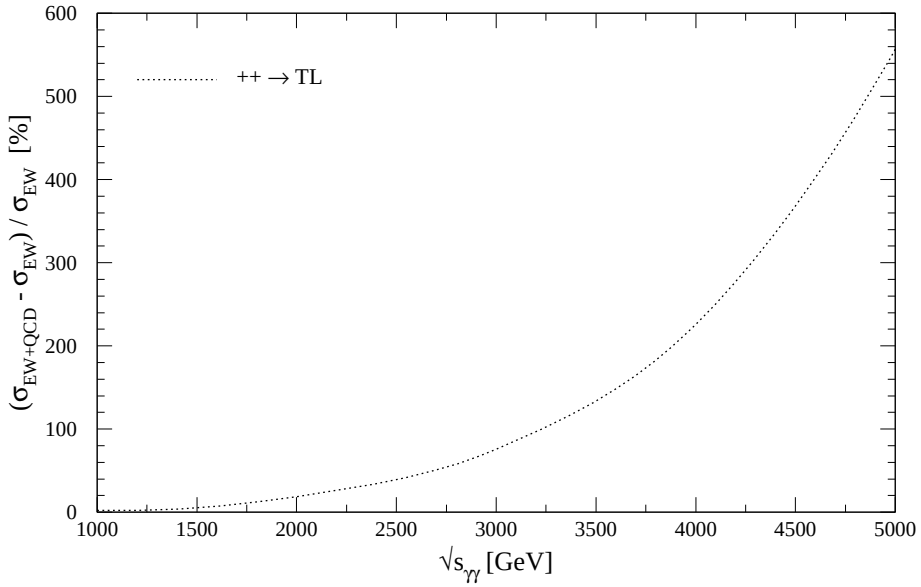

Figure 6.4: QCD corrections to the integrated cross section relative to the pure EW contribution where the Z bosons have different polarisation. The integration region was chosen as $1/2M_Z^2 < p_T^2 < 4M_Z^2$.

approaching the forward region, since the QCD amplitude gets more enhanced compared to the electroweak one. This is due to the fact that in the transition to forward physics the perturbative QCD analysis is increasingly affected by the long distance interactions, since the gluons are massless. The slight rise of the corrections from 1 to 3 TeV is due to the LL BFKL resummation and is dictated by the Pomeron intercept. Almost at the forward region the imaginary part of the QCD amplitude changes sign and becomes negative which is also visible in the relative corrections.

Next we discuss the helicity breaking cross sections. As discussed in the previous Section, the most important property of the helicity flip amplitudes is, that the electroweak parts are not anymore proportional to s as the helicity conserving parts were, so they are suppressed by one power of s compared to the QCD part of the amplitude. As a consequence the QCD corrections in comparison to the electroweak part will increase rapidly with the scattering energy, they vanish only for $p_T = 0$. This appear in Fig. 6.2(c) where the relative QCD corrections are plotted for longitudinally polarised Z bosons. The corrections are first rising when p_T is becoming smaller but they vanish for $p_T = 0$. For 1 TeV the corrections are less than 1%, but for 3 TeV they are rising up to 8%. This strong rise is dominating by the different s dependence between the electroweak and QCD amplitude. The additional rise coming from the BFKL resummation is negligible compared to this effect. While the electroweak part of the amplitude was mainly imaginary in the helicity conserving cases, here real and imaginary parts are of the same order. The oscillations visible in the plot are coming entirely from the QCD part of the amplitude, described in the previous Section. For higher Higgs masses the real part of the electroweak amplitude gets an enhancement from the Higgs pole contribution, thus the form of the corrections is changing. This is illustrated in Fig. 6.2(d) where the calculation was done for a Higgs mass of $m_H = 800$ GeV.

In Fig. 6.2(b) relative corrections are plotted where one of the Z bosons is transverse and the other longitudinally polarised. The most striking property of these corrections is their magnitude, they can be as high as 100% already at $s = 3$ TeV. This is due to the fact that here the EW part of the amplitude is smaller but the QCD part is bigger in comparison with the case where both Z bosons are longitudinally polarised. The enhancement of the QCD part is coming from the helicity conserving impact factor Φ, which is separated by a huge rapidity gap from the suppressed helicity flip impact factor. On the other hand, the QCD part is vanishing for $p_T = 0$ since the helicity flip impact factor does. Because of the dominance of the helicity conserving impact factor, the oscillations coming from the helicity flip impact factor are not visible any more. We observe here again corrections which are rising if p_T gets smaller. Both, electroweak and QCD parts of the amplitude have to vanish for the case of forward scattering due to

angular momentum conservation. Since the QCD part has its turning point for bigger p_T, approaching the forward point the corrections are decreasing. We did not plotted corrections up to $p_T = 0$ since Eq.(6.2) lacks of definition at the forward point. Again, here the corrections are rising strongly with s, since the electroweak amplitude is suppressed by one power of s compared to the QCD one. The relative corrections are approximately one order of magnitude bigger if s grows from 1 to 3 TeV. The rise resulting from the BFKL resummation is again negligible in this context.

Next we display corrections to the integrated cross section. The high energy approximation on which the QCD calculation is based, is for a kinematical range where $s \gg -t$. Thus, for the corrections to the integrated cross section we integrated only up to $p_T^2 = 4M_Z^2$, since for high p_T the QCD calculation is loosing its validity. The solid line in Fig. 6.3 displays these corrections for the helicity conserving case. In this integration range the corrections are around one percent and they have a slight rise due to the BFKL resummation, since (up to powers of logarithms) electroweak and QCD amplitudes have the same behaviour in s. The dashed line is for corrections with two longitudinal Z bosons in the final state. In this helicity breaking part the electroweak amplitude is suppressed by one power of s in comparison to the QCD amplitude, so the corrections are rising rapidly with the scattering energy. The smallness of the corrections in the integrated cross section is due to the fact that the corrections to the differential cross section, Fig. 6.2(c), are changing sign with p_T varying, presenting an oscillating behaviour.

In Fig. 6.4 again corrections to the helicity flip cross section are plotted, but here one of the Z bosons is transverse polarised. Due to the different s behaviour of the amplitudes again a strong rise of the corrections with s is present. These are very big, for higher energies the QCD part of the amplitude completely dominates this part of the cross section. The magnitude of these corrections is mainly due to the helicity conserving impact factor Φ of the QCD amplitude. The integration was done down to $p_T^2 = 1/2M_Z^2$, because the relative corrections lose they meaning for $p_T = 0$, since both amplitudes are vanishing at the forward point.

6.4 Summary

In summary, we have computed QCD corrections for $\gamma\gamma \to ZZ$ at high centre of mass energies in the kinematical region of small scattering angles. We have considered the exchange of BFKL gluon ladders which couple to the incoming photons via $\gamma \to Z$ impact factors. The electroweak part was

computed in a full one loop calculation, and a complete analysis involving all helicity channels has been done.

In the helicity conserving channel the corrections are at the order of a few percent for $s = O(1\ \text{TeV})$ and they show a moderate rise with the scattering energy. In the helicity flip channels the QCD corrections are at the same level for $s = O(1\ \text{TeV})$. However, since in this channel the electroweak amplitudes are suppressed by one power of s compared to the QCD ones, the corrections rise much stronger with the scattering energy. Already for $s = O(3\ \text{TeV})$ the QCD corrections are significant.

Concerning the QCD corrections we stress, that the LL BFKL contribution contains a noticeable scale dependence. For a more precise analysis one has to use the next-to-leading BFKL Green's function and next-to-leading impact factors. One has also to look in the full SM two loop contribution, in order to achieve precision at the percent level.

On the experimental side the separation of longitudinal and transverse final state Z bosons clearly presents a demanding challenge. Only a statistical analysis of the angular distribution of the decay products of the Z bosons allows to discriminate between the different polarisations. However, as discussed in the beginning of this letter, a careful measurement of the process $\gamma\gamma \to ZZ$ with all its different helicity configurations is important and should be pursued. The results of our study indicate that in the analysis of the measurements QCD corrections cannot be neglected and were published in Ref. [78].

Chapter 7

Summary and future work

In this thesis we studied the role of higher order QCD corrections in the Regge limit and in the small x limit. The subject was discussed in the context of three different issues. The main one was the total cross section for $\gamma^*\gamma^*$ scattering that is driven by the BFKL dynamics. The key role in this thesis was reserved for the object we name *impact factor* in high energy physics, seen from different perspectives, in BFKL formalism as a perturbatively defined object, in the colour dipole picture as the evolving colour dipole.

The calculation of the photon impact factor and the study of its properties is a major project, ongoing for the last six years now. It is necessary mainly for testing the BFKL Pomeron, but also for investigating important questions like whether we can speak for higher order Fock components of the photon wave function that would emerge naturally from the pQCD calculation, or what is the collinear limit of our calculation and what comparisons we can perform between the $\boldsymbol{k}_\perp$ factorisation scheme and the collinear factorisation. For testing the BFKL Pomeron, the numerical implementation of the impact factor is necessary. The last step to this direction was the phase space integration of the NLO virtual corrections, a step that we completed and presented in this thesis. We have found that the total NLO corrections are sizeable and negative. We cannot underestimate the mere fact that now we are ready for the next step, namely to convolute the NLO gluon Green's function with the NLO impact factor, and be able to study photonic total cross sections. Important questions like what is the optimal scale for the running of the coupling as well as what is the total significance of the collinear resummation program of the NLO BFKL kernel, can be investigated within that project.

In the second half of this thesis, higher order corrections to the Balitsky–Kovchegov equation have been estimated. The dominant notion is the parton saturation and the saturation scale. A main question was whether sat-

uration delays in rapidity when higher order correction terms are taken into account. To estimate that, our analysis was based on the introduction of a so–called "rapidity veto", which forbids two emissions to be very close in rapidity and which mimics the Pomeron intercept predicted by other resummations of the NLO BFKL equation. From analytic investigation and a full numerical analysis of the introduction of the rapidity constraint in the full Balitsky–Kovchegov equation, we studied the implications for phenomenological rapidities, without using asymptotic arguments. Finally we were able to state that saturation does delay in rapidity, the last seen as the dynamical variable, but the effect is much weaker in the case of running coupling constant. It follows from the present analysis, that the running coupling effects account for the bulk of the NLO corrections to the BK. The fact that the dipole amplitude is insensitive to the way the running is introduced, suggests that phenomenological analysis including running coupling effects do provide reliable predictions.

The last part of the thesis was reserved for a transition from the Strong to the Electroweak sector of the Standard Model. We computed QCD corrections to the process $\gamma\gamma \to ZZ$ at high centre of mass energies in the kinematical region of small scattering angles. For this process, we considered the $\gamma \to Z$ impact factor at LO. The electroweak part was computed in a full one loop calculation. A complete analysis, involving all helicity channels, was done. From our findings, we have concluded that in the helicity conserving channel the corrections are of the order of a few percent for $s = O(1 \text{ TeV})$ and they show a moderate rise with the scattering energy. In the helicity flip channels the QCD corrections are at the same level for $s = O(1 \text{ TeV})$. The corrections become significant at CLIC energies. For a more precise analysis one has to use the NLO BFKL Green's function and NLO impact factors. However, our work here was only a first attempt to see whether leading logarithm BFKL can supply significant corrections in the small x limit for EW processes. The results of our study indicate, that in the analysis of the measurements of future colliders, QCD corrections cannot be neglected.

We conclude this thesis by realizing that there are still many challenging questions searching for answers. For some of these questions we have shown that the photon impact factor and the precise estimation of the saturation line on the kinematical plane are of great importance. However, by proceeding just a bit further, we reach puzzles like the understanding of the BFKL Pomeron, its connection with the soft Pomeron or even the way that saturation effects touch the very same problem of confinement. Puzzles that are the occupants of the top positions of the 'challenging projects' list' of High Energy Scattering Physics.

Bibliography

[1] L. N. Lipatov, Sov. J. Nucl. Phys. **23** (1976) 338, E. A. Kuraev, L. N. Lipatov, V. S. Fadin, Sov. Phys. JETP **45** (1977) 199, I. I. Balitsky, L. N. Lipatov, Sov. J. Nucl. Phys. **28** (1978) 822.

[2] J. Bartels, A. de Roeck and M. Loewe, Z. Phys. **C54** (1992) 635.

[3] J. Kwiecinski, A. D. Martin and P. J. Sutton, Phys. Rev. **D46** (1992) 921.

[4] A. H. Mueller, H. Navelet, Nucl. Phys. **B282** (1987) 727

[5] J. Bartels, A. De Roeck, H. Lotter, Phys. Lett. **B 389** (1996) 742.

[6] S.J. Brodsky, F. Hautmann, and D.E. Soper, Phys. Rev. **D56** (1997) 6957, Phys. Rev. Lett. **78** (1997) 803.

[7] http://l3.web.cern.ch/l3/

[8] V. S. Fadin, L. N. Lipatov, Phys. Lett. **B429** (1998) 127.

[9] M. Ciafaloni, G. Camici, Phys. Lett. B **430** (1998) 349.

[10] G.P. Salam, JHEP**8907** (1998) 19,
M. Ciafaloni and D. Colferai, Phys. Lett.**B452** (1999) 372,
M. Ciafaloni, D. Colferai and G.P. Salam, Phys. Rev. **D60** (1999) 114036,
R.S. Thorne, Phys. Rev. **D60** (1999) 054031,
J. R. Forshaw, D. A. Ross and A. Sabio Vera, Phys. Lett. **B498** (2001) 149,
G. Altarelli, R. D. Ball and S. Forte, Nucl. Phys. **B575** (2000) 313, Nucl. Phys. **B621** (2002) 359, Nucl. Phys. **B674** (2003) 459,
M. Ciafaloni, D. Colferai, G. P. Salam and A. M. Stasto, Phys. Lett. **B576** (2003) 143, Phys. Rev. **D68** (2003) 114003, Phys. Lett. **B587** (2004) 87,
J. R. Andersen and A. Sabio Vera, Phys. Lett. **B567** (2003) 116, Nucl. Phys. **B679** (2004) 345, `hep-th/0406009`.

[11] V. N. Gribov and L. N. Lipatov, Sov. J. Nucl. Phys. **15** (1972) 438; Yu.L. Dokshitzer, Sov. Phys. JETP **46** (1977) 641; G. Altarelli and G. Parisi, Nucl. Phys. **B126** (1977) 298.

[12] K. Golec-Biernat and M. Wusthoff, Phys. Rev. D **59** (1999) 014017.

[13] J. Bartels, S. Gieseke and C. F. Qiao, Phys. Rev. D **63** (2001) 056014 [Erratum-ibid. D **65** (2002) 079902].

[14] J. Bartels, S. Gieseke and A. Kyrieleis, Phys. Rev. D **65** (2002) 014006.

[15] J. Bartels, D. Colferai, S. Gieseke and A. Kyrieleis, Phys. Rev. D **66** (2002) 094017.

[16] J. Bartels and A. Kyrieleis, `hep-ph/0407051`.

[17] L. V. Gribov, E. M. Levin, and M. G. Ryskin, *Nucl. Phys.* **B 188** (1981) 555; Phys. Rep. **100** (1983) 1.

[18] Ia. Balitsky, Nucl.Phys. **B463** (1996) 99.

[19] Yu. Kovchegov, Phys. Rev. **D60** (2000) 034008.

[20] V. S. Fadin, "Status of the small-x resummation programme", DESY THEORY WORKSHOP 2002, Hamburg, Germany

[21] L. N. Lipatov, talk presented at the 4th Workshop on Small-x and Diffractive Physics, FNAL, September 1998

[22] C. R. Schmidt, Phys. Rev. **D60** (1999) 074003.

[23] J. R. Forshaw, D. A. Ross and A. Sabio Vera, Phys. Lett. **B455** (1999) 273.

[24] J. R. Forshaw and D. A. Ross, *Quantum Chromodynamics and the Pomeron*, Cambridge 1997 (Cambridge lecture notes in physics 9)

[25] V. Barone and E predazzi, *High-Energy Particle Difraction*, Springer 2002

[26] V. S. Fadin, Zh. Eksp. Teor. Fiz. Pis'ma **61** (1995) 342; V. S. Fadin, R. Fiore and A. Quartarolo, Phys. Rev. **D53** (1996) 2729; V. S. Fadin, M. I. Kotsky, Yad. Fiz. **59**(6) (1996) 1; V. S. Fadin, M. I. Kotsky and R. Fiore, Phys. Lett. **B359** (1995) 181.

[27] V. S. Fadin and L. N. Lipatov, Nucl. Phys. **B406** (1993) 259; V. S. Fadin, R. Fiore and A. Quartarolo, Phys. Rev. **D50** (1994) 5893

[28] V. S. Fadin, M. I. Kotsky and L. N. Lipatov, Phys. Lett. **B415** (1997) 97.

[29] S. Catani, M. Ciafaloni and F. Hautmann, Phys. Lett. **B242** (1990) 97; Nucl. Phys. **B366** (1991) 135; G. Camici and M. Ciafaloni, Phys. Lett. **B386** (1996) 341; V. S. Fadin, R. Fiore, A. Flachi and M. I. Kotsky, Phys. Lett. **B422** (1998) 287

[30] M. Ciafaloni, D. Colferai and G. P. Salam, Phys. Rev. **D60** (1999) 114036

[31] D. Y. Ivanov, A. Papa, Nucl. Phys. **B732** (2006) 183.

[32] J. R. Andersen, A. Sabio Vera, Nucl. Phys. **B679** 345 (2004), Nucl. Phys. **B699** (2004) 90 Phys. Lett. **B567** (2003) 116

[33] A. H. Mueller and J. Qiu, Nucl. Phys. **B268** (1986) 427.

[34] A. H. Mueller, Nucl. Phys. **B415** (1994) 373

[35] J. Jalilian-Marian, A. Kovner, A. Leonidov and H. Weigert, Nucl. Phys. **B504** (1997) 415; Phys. Rev. **D59** (1999) 014014. J. Jalilian-Marian, A. Kovner and H. Weigert, Phys. Rev. **D59** (1999) 014015.

[36] H. Weigert, Nucl. Phys. **A703** (2002) 823.

[37] L. McLerran and R. Venugopalan, Phys. Rev. **D49** (1994) 2233; Phys. Rev. **D49** (1994) 3352; Phys. Rev. **D50** (1994) 2225;
J. Jalilian-Marian, A. Kovner, L. McLerran and H. Weigert, Phys. Rev. **D55** (1997) 5414; R. Venugopalan, Acta Phys. Polon. **B30** (1999) 3731;
E. Iancu, A. Leonidov and L. McLerran, Nucl.Phys. **A692** (2001) 583;
E. Ferreiro, E. Iancu, A. Leonidov and L. McLerran, Nucl. Phys. **A701** (2002) (489);
E. Iancu and R. Venugopalan, `hep-ph/0303204`.

[38] J. Bartels, L.N. Lipatov, and J.P. Vacca, `hep-ph/0404110`, Nucl. Phys. **B706** (2005) 391.

[39] A. Kovner and U.A. Wiedemann, Phys. Rev. **D66** (2002) 051502; Phys. Rev. **D66** (2002) 034031; Phys. Lett. **B551** (2003) 311.

[40] A. M. Stasto, K. Golec-Biernat and J. Kwiecinski, Phys. Rev. Lett. **86** (2001) 596.

[41] M. Lublinsky, Eur. Phys. J. **C21** (2001) 513.

[42] A. H. Mueller, Phys. Lett. **B396** (1997) 251.

[43] L. D. McLerran, Lect. Notes Phys. **583** (2002) 291; `hep-ph/0104285`.

[44] Yu. Kovchegov, Phys. Rev. **D61** (2000) 074018; E. Levin and K. Tuchin, Nucl. Phys. **B573** (2000) 833; Nucl. Phys. **A691** (2001) 779.

[45] A. Kovner and U.A. Wiedemann, Phys. Rev.**D66** (2002) 051502.

[46] E. Iancu, K. Itakura and L. McLerran, Nucl. Phys. **A708** (2002) 327.

[47] S. Munier and R. Peschanski, Phys. Rev. **D69** (2004) 034008; Phys. Rev. Lett. **91** (2003) 232001; `hep-ph/0401215`.

[48] M. Braun, Eur. Phys. J. **C16** (2000) 337.

[49] E. Gotsman, E. Levin, M. Lublinsky, and U. Maor, Eur. Phys. J **C 27** (2003) 411; parameterizations are available at www.desy.de/∼lublinm/.

[50] N. Armesto and M. Braun, Eur. Phys. J. **C20** (2001) 517.

[51] K. Golec-Biernat, L. Motyka, A. Stasto, Phys. Rev. **D65** (2002) 074037.

[52] M. Lublinsky, E. Gotsman, E. Levin, and U. Maor, Nucl. Phys. **A696** (2001) 851.

[53] K. Rummukainen and H. Weigert, Nucl. Phys. **A739** (2004) 183.

[54] K. Golec-Biernat and A.M. Stasto, Nucl. Phys. **B 668** (2003) 345;
E. Gotsman, M. Kozlov, E. Levin, U. Maor, and E. Naftali, `hep-ph/0401021`.

[55] K. Kutak and A. Stasto, `hep-ph/0408117`.

[56] J. L. Albacete, N. Armesto, J. G. Milhano, C. A. Salgado and U. A. Wiedemann, `hep-ph/0408216`.

[57] E. Gotsman, E. Levin, M. Lublinsky, U. Maor, and E. Naftali, Acta Phys. Polon. **B34** (2003) 3255;
J. Bartels, E. Gotsman, E. Levin, M. Lublinsky, and U. Maor, Phys. Rev. **D68** (2003) 054008; Phys. Lett. **B 556** (2003) 114;
E. Levin and M. Lublinsky, Nucl. Phys. **A696** (2001) 833; Phys. Lett. **B521** (2001) 233.

[58] E. Iancu, K. Itakura and S. Munier Phys.Lett. **B590** (2004) 199.

[59] V. S. Fadin,

Nucl. Phys. Proc. Suppl. **99A** (2001) 204.

[60] V. S. Fadin, D. Y. Ivanov and M. I. Kotsky, Nucl. Phys. **B658** (2003) 156.

[61] V. S. Fadin, R. Fiore, M. I. Kotsky and A. Papa, Phys. Rev. **D61** (2000) 094005.

[62] I. Balitsky and A. Belitsky, Nucl. Phys. **B629** (2002) 290.

[63] D.N. Triantafyllopoulos, Nucl. Phys. **B648** (2003) 293.

[64] V. A. Khoze, A. D. Martin, M. G. Ryskin and W. J. Stirling, `hep-ph/0406135`.

[65] E. Levin and M. Lublinsky, Nucl. Phys. **A730** (2004) 191.

[66] A.H. Mueller and D.N. Triantafyllopoulos, Nucl. Phys. **B640** (2002) 331.

[67] G. Chachamis, M. Lublinsky and A. Sabio Vera, Nucl. Phys. **A748** (2005) 649.

[68] G. Jikia, Nucl. Phys. **B405** (1993) 24.

[69] G. Bélanger and F. Boudjema, Phys. Lett. **B288** (1992) 210; K. A. Peterson and S. Godfrey, `hep-ph/9302297`; O. J. P. Éobli, M. C. Gonzaléz-García and S. F. Novaes, Nucl. Phys. **B411** (1994) 381; O. J. P. Éobli, M. B. Magro, P. G. Mercandante and S. F. Novaes, Phys. Rev. **D52** (1995) 15; S. Godfrey, `hep-ph/9505252`; G. J. Gounaris, F. M. Renard, Z. Phys. **C69** (1996) 513; G. J. Gounaris, J. Layssac, F. M. Renard, Z. Phys. **C69** (1996) 505; M. Baillargeon, G. Bélanger and F. Boudjema, Nucl.Phys. **B500** (1997) 224; E. Boos et al., `hep-ph/0103090`.

[70] I.F. Ginzburg, preprint 28(182) INP Novosobirsk (1990); G.J. Gounaris, J. Layssac, F.M. Renard, Z. Phys. **C65** (1995) 505; G.J. Gounaris, F.M. Renard, Z. Phys. **C65** (1995) 513; A. T. Banin, I. F. Ginzburg and I. P. Ivanov, Phys. Rev. **D59** (1999) 115001.

[71] F. Boudjema, in Physics and Experiments with Linear e^+e^- Colliders, Waikoloa, Hawaii, 1993, Ed. F.A. Harris *et al.*, *Word Sci.*, vol.II, p. 712.

[72] G.J. Gounaris, J. Layssac, P.I. Porfyriadis and F.M. Renard, *Eur. Phys. J.* **C 13** (2000) 79.

[73] J.L. Hewett and F.J. Petriello, Phys. Rev. **D64** (2001) 095017.

[74] T. G. Rizzo, Phys. Rev. **D60** (1999) 115010; K. Cheung, Phys. Rev. **D61** (2000) 015005; H. Davoudiasl, Phys. Rev. **D60** (1999) 084022; Phys. Rev. **D61** (2000) 044018.

[75] E. E. Boos and G. V. Jikia, Phys. Lett. **B275** (1992) 164.

[76] A. Dobado and M.J. Herrero, Phys. Lett. **B228** (1989) 495; **233** (1989) 505; J.F. Donoghue and C. Ramirez, Phys. Lett. **B234** (1990) 361.

[77] K. Peters and G.P. Vacca Eur. Phys. J. **C30** (2003) 345.

[78] G. Chachamis and K. Peters, Phys. Lett. **B580** (2004) 169.

[79] T. Hahn and M. Pérez-Victoria, Comp. Phys. Commun. **118** (1999) 153.

[80] J. Küblbeck, M. Böhm, and A. Denner, Comp. Phys. Commun. **60** (1990) 165;
T. Hahn, `hep-ph/0012260`.

[81] G.J. van Oldenborgh and J.A.M. Vermaseren, Z. Phys. **C46** (1990) 425; G.J. van Oldenborgh, Comp. Phys. Commun. **66** (1991) 1.

[82] J. Bartels, K. Golec-Biernat and K. Peters, Acta Phys. Pol. **B34** (2003) 3051.

[83] T. Behnke, S. Bertolucci, R. D. Heuer and R. Settles, "TESLA Technical design report. Pt. 4: A detector for TESLA," DESY-01-011

First of all I would like to thank Prof. J. Bartels, for his support, interest, criticism and invaluable guidance during the years. I have profited from numerous discussions with him and from his clear view of how a theorist should be. Thank you for the Physics.

I am very grateful to Agustin Sabio Vera, Misha Lublinsky and Krisztian Peters for the fruitful and enjoyable collaborations. Thank you Agustin and thank you Misha for honouring me with your friendship and for all the help. Thank you for the Physics.

I am deeply grateful to M. Diehl for all his help and interest. It was a great experience to be in contact with G. Levin, V. Fadin and L. Lipatov. I am thankful for many valuable, enlightening and stimulating discussions. Special thanks to G. Levin for his help. I am obliged to L. Lipatov for his interest and for sharing his ideas with me. Thank you for the Physics.

I wish to thank A. Kyrieleis, C. F. Qiao and S. Giesieke for many helpful conversations. Many thanks to G. P. Vacca, K. Motyka, K. Golec Biernat, A. Stasto, H. Jung and S. Bondarenko. Many thanks to K. Kutac, T. Robens, F. Schwennsen and T. Prüstel for the many hours spent together, whether it was for discussing Physics or not.

I am indebted to the II. Institute of Theoretical Physics and the DESY Theory Group for the inspiring and motivating working environment. This work was supported by the Graduiertenkolleg 'Zukünftige Entwicklungen in der Teilchenphysik'.

All the work in this thesis would not have been possible without the care and support of many people and I thank them all. Special thanks to Olivia, Gayane, Lilly and Achim for their friendship. Thanks to my friends in Spain. Thanks to my Durham friends. Thank you to Ebru and to Jose Ignacio. Thank you to Laika. Special thanks to many people in Greece. Thanks to my relatives Petros, Ageliki, Toula, Ilias, Theodoris, Dimitris. Ilia, Theodori and Dimitri many thanks for the encouragement. Thanks to my friends Aris (many times my link to the others), Mixalis, Biky, Nikos and Babis.

Olga thank you for your love and support.

I cannot express my gratitude to my family for their help. To my mother, Maria, who has been and is always there and to whom any "thank you" in any form is not enough. To my little sister, Garifalia, for being such a special person and for always standing by me. To my father, Dimitri, who is not any more in life, but who was the one to give me my first Physics lessons at a very early age and also lessons for life that I will always carry with pride. He was one of the brightest minds I have ever known and in whatever I succeed he has his own piece of merit.